Thesis for the degree of Doctor of Philosophy

Intense laser-plasma interactions

Joel Magnusson

Department of Physics
Chalmers University of Technology
Gothenburg, Sweden, 2019

Intense laser-plasma interactions
Joel Magnusson
ISBN 978-91-7905-198-3

Doktorsavhandlingar vid Chalmers tekniska högskola
Ny serie nr 4665
ISSN 0346-718X

Department of Physics
Chalmers University of Technology
SE–412 96 Gothenburg
Sweden
Telephone +46 (0)31-772 1000

Cover:
Illustration of an electric dipole wave showing the electric (red) and magnetic (blue) field lines. Electrons (yellow) passing through this field can emit high-energy photons (grey) through Compton scattering, which may in turn decay into electron-positron (cyan) pairs.

Chalmers Reproservice
Gothenburg, Sweden, 2019

Intense laser-plasma interactions
JOEL MAGNUSSON
Department of Physics
Chalmers University of Technology

Abstract

In the interaction of ultra-intense laser fields with matter, the target is rapidly ionized and a plasma is formed. The ability of a plasma to sustain acceleration gradients, orders of magnitude larger than achievable with conventional accelerators, has led to a great interest in laser-driven plasma-based particle and radiation sources, with applications in materials science, biology and medicine.

In this thesis, two separate, yet highly related, topics are pursued. The first half of the thesis concerns plasma-based techniques for ion acceleration, through the interaction of intense laser fields with solid density targets. In the most accessible acceleration scheme, the ion acceleration is mediated by a population of suprathermal, *hot*, electrons produced by the rapid heating of the target surface. We study the effect of adding microstructures to the target surface, show how this affects the distribution of hot electrons and discuss its implications for ion acceleration. We further study a novel acceleration scheme, aimed at achieving controllable ion acceleration using a frequency chirped standing wave. We analyse the robustness of this scheme, named chirped-standing-wave acceleration, under non-ideal conditions and discuss its prospects and limitations.

The second half of the thesis concerns laser-matter interactions where the emission of high-energy photons necessitates a quantum mechanical description of radiation reaction and enables a prolific production of electron-positron pairs. In this regime, we study the interaction of an energetic electron beam with an optimally focused laser field, in the form of a dipole wave, and highlight its capabilities as a multi-GeV photon source. We further discuss the phenomena observed in this setup, in particular investigating the emergence of pair production cascades, and provide a review of previous results. Finally, we highlight a number of regimes within reach of upcoming laser facilities.

Keywords: laser, plasma, ion acceleration, radiation generation, radiation reaction, pair production cascades, particle-in-cell

Publications

This thesis is based on the following publications:

A J. Magnusson, A. Gonoskov, M. Marklund,
Energy partitioning and electron momentum distributions in intense laser-solid interactions,
The European Physical Journal D **71**, 231 (2017).

B J. Magnusson, F. Mackenroth, M. Marklund, A. Gonoskov,
Prospects for laser-driven ion acceleration through controlled displacement of electrons by standing waves,
Physics of Plasmas **25**, 053109 (2018).

C J. Magnusson, A. Gonoskov, M. Marklund, T. Zh. Esirkepov, J. K. Koga, K. Kondo, M. Kando, S. V. Bulanov, G. Korn, S. S. Bulanov,
Laser-particle collider for multi-GeV photon production,
Physical Review Letters **122**, 254801 (2019).

D J. Magnusson, A. Gonoskov, M. Marklund, T. Zh. Esirkepov, J. K. Koga, K. Kondo, M. Kando, S. V. Bulanov, G. Korn, C. G. R. Geddes, C. B. Schroeder, E. Esarey, S. S. Bulanov,
Multiple-colliding laser pulses as a basis for studying high-field high-energy physics,
Accepted for publication in Physical Review A.
arXiv:1906.05235 [physics.plasm-ph]

Statement of contribution

Paper A: I developed the numerical diagnostics tools used for tracking the partitioning of energy between different energy channels. I performed all simulations, analysed the data and produced all figures. I prepared the draft of the entire paper, except for parts of the introduction. I finalized the text for publication together with the co-authors.

Paper B: I developed the idea for the paper together with the co-authors and I performed all simulations. I performed all data analysis and I produced all figures. I derived the estimates for when CSWA performs efficiently, leading up to equation 13, and derived the remaining equations together with co-authors. I prepared the draft of the entire paper, excluding section 2 and part of the introduction. I finalized the text for publication together with the co-authors.

Paper C: I developed the concept for the paper together with co-authors. I performed all QED-PIC simulations and the analysis of the related data. I produced all figures except figure 2 and derived the motivating estimates together with the co-authors. I prepared a majority of the draft, primarily excluding parts of the introduction and the section containing the motivating estimates. I finalized the text for publication together with the co-authors.

Paper D: I developed the concept for the paper together with co-authors. I performed all simulations and data analysis. I produced figures 2, 3 and 5 together with the co-authors and produced all remaining figures. I wrote a majority of the draft in close collaboration with the co-authors. I finalized the text for publication together with the co-authors.

Related publications not included in the thesis

E L. Giuffrida, K. Svensson, J. Psikal, D. Margarone, P. Lutoslawski, V. Scuderi, G. Milluzzo, J. Kaufman, T. Wiste, M. Dalui, H. Ekerfelt, I. Gallardo Gonzalez, O. Lundh, A. Persson, A. Picciotto, M. Crivellari, A. Bagolini, P. Bellutti, J. Magnusson, A. Gonoskov, L. Klimsa, J. Kopecek, T. Lastovicka, G.A.P. Cirrone, C.-G. Wahlström, G. Korn,
Nano and micro structured targets to modulate the spatial profile of laser driven proton beams.,
Journal of Instrumentation **12**, C03040 (2017)

F L. Giuffrida, K. Svensson, J. Psikal, M. Dalui, H. Ekerfelt, I. Gallardo Gonzalez, O. Lundh, A. Persson, P. Lutoslawski, V. Scuderi, J. Kaufman, T. Wiste, T. Lastovicka, A. Picciotto, A. Bagolini, M. Crivellari, P. Bellutti, G. Milluzzo, G. A. P. Cirrone, J. Magnusson, A. Gonoskov, G. Korn, C.-G. Wahlström, D.Margarone,
Manipulation of laser-accelerated proton beam profiles by nanostructured and microstructured targets,
Physical Review Accelerators and Beams **20**, 081301 (2017).

Acknowledgements

I would first and foremost like to express my deepest gratitude towards my supervisors Mattias Marklund and Arkady Gonoskov for all of their support, and for continuing to both inspire and encourage me. I would also like to thank Andreas Isacsson for his guidance, as well as for sharing his wisdom whenever I disturb him in his office. I am grateful to my many colleagues and especially past and present members of my research group for creating a pleasant and comradely environment, and with whom I have enjoyed a great many crappy movies.

I would also like to thank Stuart Mangles for his hospitality during my stay at Imperial, Chris Ridgers and Chris Murphy for their hospitality during my visit to York, and Stepan Bulanov for being ever so easy to collaborate with. A special thanks to Tom Blackburn for being the best imaginable office mate and for putting up with me for almost 4 years, as well as to Benjamin Svedung Wettervik for providing daily distractions from the work at hand and for making sure the office sofa is never alone. Finally I would like to express my gratitude to my family and many friends for their support.

Joel Magnusson, 2019

Contents

Chapter 1

Introduction

Physics is arguably one of the oldest of sciences and generally concerns the nature of energy and matter. As a science it has expanded tremendously over the centuries, not least compared to the beginning of the 20th century when the theories of quantum mechanics and general relativity revolutionized the science. Today, physics covers a very broad range of subjects, making it practically impossible for physicists to be experts within every field. Nevertheless, physicists often draw inspiration from a common toolbox, applying it in seemingly wildly different areas. Regardless of the field of application, the essence of physics lies in describing the world as accurately as possible using mathematical models. The purpose of this is not only to be able to explain and reproduce what has been observed in experiments, but also to predict new phenomena. Given enough predictive power the models we create can then also be used as a guide forward and, for this reason, often serves as a strong motivator in the planning and construction of new research infrastructure.

However, not all experiments are easily explained and not all phenomena are easy to model. Most physics research today is therefore supported by numerics, one way or another. Not necessarily because the underlying equations are difficult to write down, but because in order to obtain a verifiable or predictive result, the equations must often be solved under realistic conditions. Some problems require a combination of different models, perhaps only valid in different, yet overlapping, regimes. Some problems contain multiple scales and are highly dependent on effects from all of them. Some have unknown initial conditions and some contain all of the above issues. The difficulty then lies in determining what is essential and what is not, and to keep only what is necessary to obtain a valuable result. For any given problem, this naturally leads to a hierarchy of different models where generality and scope is often traded for tractability. While useful results are regularly obtained from simpler models, even using analytics alone, some

questions can only be answered using more comprehensive ones, often requiring large-scale simulations.

In this thesis we generally concern ourselves with the interaction of strong electromagnetic fields with matter. This subject naturally falls into the category of plasma physics, which itself is mainly a combination of classical electrodynamics and statistical physics. Depending on the problem statement, it can also contain significant elements of quantum mechanics, in particular in relation to atomic and nuclear physics. While the contribution from these two topics will remain largely unexplored, given the field strengths considered in parts of this thesis we will discuss effects due to quantum electrodynamics.

As may already have become apparent, the topic of this thesis carries many of the issues detailed earlier. On its own, plasma physics contains a rich set of complex phenomena and is characterized by the collective motion of its constituents. Coupled with the influence of strong electromagnetic fields, hereafter assumed to be generated using a powerful laser, the interaction becomes highly nonlinear. Accurate description of the physics therefore require large-scale simulations, not seldom utilizing thousands of processors for several hours, and constitutes the main tool in writing this thesis. This is supported by simplified analytical and numerical models, predominantly based on single-particle dynamics in a given field, in order to gain further insights where applicable. Even so, the computer models used to simulate the physics are only accurate to a certain extent and important aspects are left out for the benefit of computability. In particular, the process of ionization is commonly omitted and the initial stages of the interaction is often replaced by an experienced guess on the density and ionization level of the plasma. This is not due to laziness, but reflects our lack of knowledge in key features of the experiments, on which a more accurate description depends. It is a consequence of the initial plasma formation occurring over a much larger time scale, and at a much lower intensity, than suggested by the parameters of the main pulse.

Getting back to the subject of this thesis, it more specifically concerns the science of laser-based particle and light sources and is centred around two related topics (i) acceleration of protons through laser-solid interaction and (ii) generation of high-energy photons through laser-beam interaction. Central to both of these topics is the transfer of energy to the particles of interest, which can be either transferred from the field itself or simply mediated by it, while simultaneously considering other source properties, such as particle numbers and collimation. In relation to this, the thesis covers the basics of laser-plasma and laser-particle interactions, and discusses the principal mechanisms of transferring energy before addressing the papers on which the thesis is based. The goal is to explain the underlying physics as accurately as possible and while the subject is approached from a theoretical point of view, the discussion aspires to be as honest as possible on the limits

of our current understanding and not forgetting the experimental challenges that exists.

1.1 The road to high-intensity lasers

The study of electric and magnetic fields and their interaction with matter by far predates the classical theory of electromagnetism. As the knowledge of electromagnetism expanded, and techniques for generating the fields improved, studies were performed at increasingly higher field strengths. In the early half of the 20th century these studies could be performed using for example Van de Graaff generators, cavities or masers, but are today dominated by the use of lasers, which allow for an unprecedented compression of electromagnetic energy. As such, the recent history of the research on strong electromagnetic fields is highly intertwined with the evolution of high-intensity lasers, illustrated in Figure 1.1.

The laser was imagined long before its first successful construction by Maiman in 1960 [1], with many theoretical works preceding its invention. Once realized, the capabilities of lasers rapidly improved and techniques for producing pulsed laser beams were soon invented. This made it possible to increase the achievable field intensities by simply shortening the pulse duration, even if the pulse energy is left unchanged. Pulse durations on the nanosecond scale was first achieved using Q-switching [2] and then through mode-locking [3] not long after, with the latter opening up the possibility for pulse durations on the pico- and even femtosecond scale.

By the end of the decade, and after a rapid development had pushed the peak intensities up to $10^{14}\,\mathrm{W/cm^2}$, this tremendous progress stagnated. At these intensities the radiation causes breakdown of the amplifying media and increasing the aperture to combat the breakdown would instead lead to the growth of parasitic transverse modes, hampering the efficiency of this strategy. As a result, there were only (comparatively) minor improvements in peak intensity over the course of the next two decades and as this required increasingly more expensive laser systems these results became largely limited to a few large-scale facilities.

Inspired by similar techniques from the radar community, a solution was finally presented in the form of *chirped-pulse amplification* (CPA) by Strickland and Mourou in 1985 [4], which recently won them the 2018 Nobel Prize in Physics. A variation of this technique, *optical parametric chirped-pulse amplification* (OPCPA) [5], was proposed not long after and has become an important alternative. In CPA the laser pulse is passed through a dispersive delay line, stretching the pulse in time by imposing a strong frequency modulation (chirping), before the main amplification stage. Stretching the pulse proportionally decreases its intensity, after which the pulse is amplified as usual. The stretched, amplified pulse is then recompressed to its original

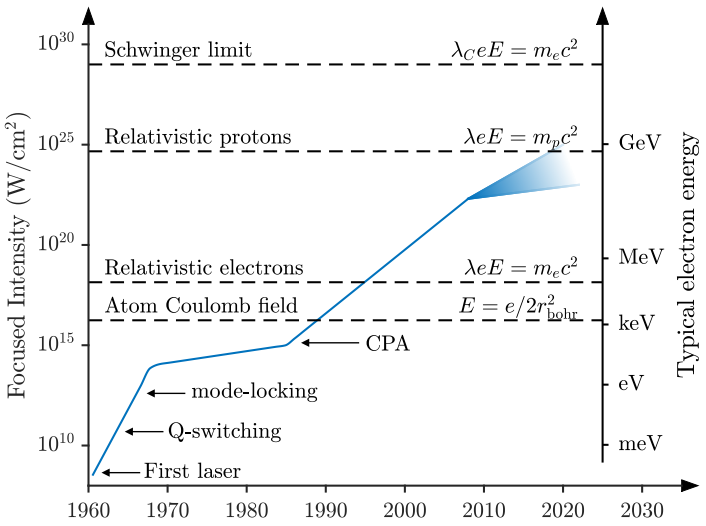

Figure 1.1: Evolution of the record peak intensities achieved with high-intensity lasers. The second axis indicates the typical electron energy obtained at the given intensity and with a laser wavelength of $\lambda = 1\,\mu\text{m}$. The marked area shows the range of peak intensities that could be produced at upcoming 10 PW laser facilities.

length using a second dispersive delay line, inverting the effect of the first, resulting in a multifold increase of the laser intensity. As the pulse can easily be stretched by more than a factor of thousand, the previous limitations due to breakdown of the amplifying media can now be surpassed by several orders of magnitude. The stretcher and compressor can for example be realized as a pair of diffraction gratings, positioned and oriented such that the different wavelengths of light are made to travel different distances. Another advantage of this technique is that the component now experiencing the strongest fields is the surface of the final grating in the compressor, which can have a much greater damage threshold than that of the amplifying media.

At about the same time as the introduction of CPA, it was discovered that titanium doped sapphire crystals Ti:Al_2O_3 (or Ti:Sa) could serve as a broad-band amplifying medium, allowing for pulses in the tens of femtoseconds [6, 7]. This provided an alternative to the Nd:glass lasers (and other neodymium-doped compounds) often used to reach high intensity and power. Today, high-intensity lasers based on Ti:Sa are often used to produce 1–100 J in pulses of 10–100 fs and with high repetition rates (>0.1 Hz) while Nd:glass lasers provide longer pulses (nano- and picosecond) of greater energy (kilojoules) and lower repetition rates (<0.1 Hz).

Enabled by these breakthroughs, there was a renewed revolution within high-intensity laser science that eventually lead up to the current peak in-

tensity record of $2 \times 10^{22}\,\mathrm{W/cm^2}$, at the University of Michigan in 2008 [8]. The laser, HERCULES, was capable of providing pulses of 300 TW peak power at a 0.1 Hz repetition rate and achieved the record intensity using adaptive optics with an $f/1$ parabolic mirror. At the same time the record peak power was just over 1 PW, first achieved with the NOVA Petawatt at the Lawrence Livermore National Laboratory [9] and subsequently also with high repetition rate systems [10]. The available peak powers have since then been pushed even further, with the current record set at 5.4 PW [11] and several upcoming facilities are expected to demonstrate 10 PW in the near future [10, 12–16]. At this power, laser intensities of 10^{23}–$10^{24}\,\mathrm{W/cm^2}$ could be reached using focusing optics similar to that used in producing the latest intensity record, with the equivalent of $10^{25}\,\mathrm{W/cm^2}$ being the physical limit if full 4π-focusing is employed. With several proposals for 100 PW systems currently under discussion [10, 17, 18], it is not impossible that even greater laser intensities will be reached in the coming decades.

The intensities given above are obviously very large, but perhaps difficult to relate to without further elucidation of their scale. As a point of reference, the Sun irradiates the Earth at the top of our atmosphere with an average intensity of $1361\,\mathrm{W/m^2}$ [19]. Put in more familiar terms, the record laser-intensity is therefore equivalent to focusing all sunlight striking the Earth to a spot size of about 10 µm, which is quite literally the width of human hair. The difference, of course, is that the laser field only lasts for but a tiny fraction of a second. But light also carries momentum, making it possible to relate the field intensity to a *radiation pressure* that the light can impose upon interacting with an object. For an intensity of $10^{22}\,\mathrm{W/cm^2}$ this pressure is about 10^{18} Pa, or roughly ten trillion times the normal atmospheric pressure. This natural capacity for both heating and pushing has made high-intensity lasers an attractive tool for studying high-temperature high-density systems, otherwise only encountered in astrophysical environments. The very same qualities have also inspired the development of techniques for laser-plasma based particle accelerators and radiation sources. As much stronger fields are allowed in laser-plasma interactions, such sources can be made considerably smaller than conventional alternatives.

1.2 Laser-plasma based acceleration

High-energy particle beams is today a trademark of particle and nuclear physics where it is used for studying the fundamental interactions of particles, but has also become an equally indispensable tool within medicine, biology and materials science. Accelerating particles to the highly relativistic energies possible today has required many technological advances. Today's conventional accelerators operate using strong electromagnetic fields generated inside a metallic radiofrequency (RF) cavity, and are either linear

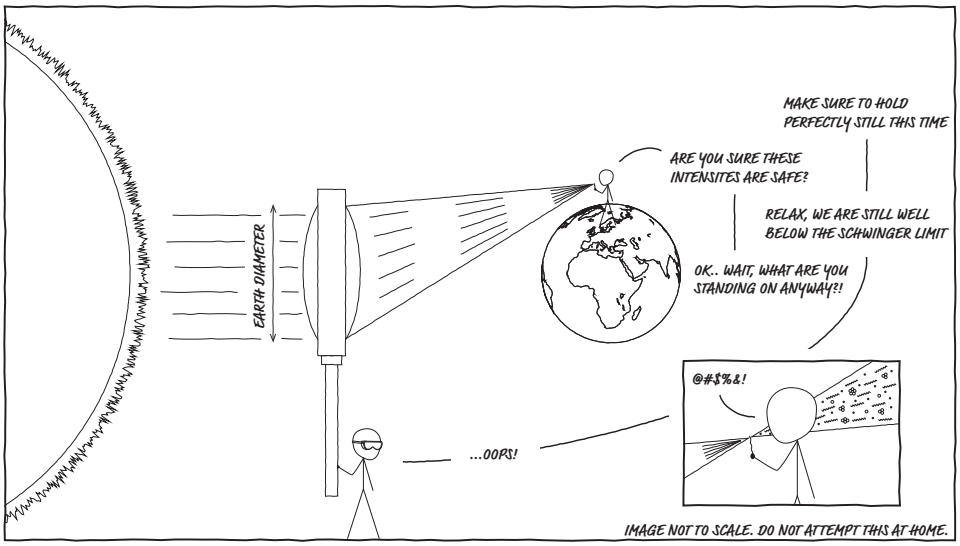

Figure 1.2: Comic illustration showing a common analogy to the capabilities of high-intensity lasers. Inspired by the graphical style of xkcd [20].

(accelerates particles along a straight line) or circular (accelerates particles along a circle) depending on their purpose. Common to both types is that larger physical size translates into greater particle energies, as the electric field strengths are limited to $\sim$10 MV/m in order to avoid ionizing the walls of the cavity.

The main enemy when accelerating particles are energy losses due to radiation emission. These losses depend on both the mass of the particle (m^{-4}) and the curvature of its motion (ρ^{-2}), with lighter particles radiating much more strongly for a given track radius and smaller radii translating into greater emissions. Linear accelerators are therefore often used to accelerate light particles such as electrons and positrons, and the maximum possible particle energy will be directly proportional to the length of the accelerator. The largest linear accelerator in the world is the Stanford Linear Accelerator (SLAC) at 3 km, used for electron-positron collisions, and is able to impart 1 GeV per 100 m.

In accelerating heavier particles such as protons, for which the energy losses are substantially lower, the benefit of using circular accelerators is that it allows for an iterative acceleration over several revolutions. The maximum energy that can be reached is then limited not only by the energy losses, but also by the strength of the bending magnets. In accelerating hadrons the latter is typically the key limiting factor, necessitating a large radius of curvature. The largest circular accelerator in the world, and also the largest accelerator in general, is the Large Hadron Collider (LHC) with a radius of 4 km, and is able to accelerate protons to an energy of 7 TeV. Most circular accelerators in use today, including the LHC, are technically

synchrotrons, for which the bending magnetic field strength is synchronized to the kinetic energy of the accelerated particles such that they travel in a closed loop, despite gaining energy. While radiation emission limits the maximum energy of especially light particles, it is not always unwelcome. In fact, due to its widely tunable properties and short wavelengths the emitted *synchrotron radiation* is frequently used in several spectroscopic and imaging applications for research in materials science, physics and chemistry.

Research on the interaction between strong laser fields and matter first began in the 1970s and was largely driven by its uses for atomic and molecular physics and laser-induced nuclear fusion. As the available intensities grew it became apparent that it also holds great potential for particle acceleration, which had been suggested and studied in earlier theoretical works, some even preceding the invention of the laser. At intensities above $10^{16}\,\mathrm{W/cm^2}$ the laser field is able to rival the Coulomb field of an atom, leading to rapid ionization of a target, eventually creating a plasma. While conventional accelerators must avoid such plasma formation from occurring, high-intensity lasers do not rely on the cavity walls for field generation, allowing us to circumnavigating these restrictions. Through the interaction of intense laser fields with a plasma it is possible to both create and sustain acceleration gradients of 100 GV/m and above, greatly surpassing the limits of conventional accelerators. This significantly reduces the required acceleration distances and opens up the possibility for more compact and thereby cheaper accelerators.

Today, state-of-the art lasers are capable of producing ultra-short electron bunches of more than 1 GeV over an acceleration distance of a few centimetres through a process called *laser wakefield acceleration* (LWFA) that involves propagating the laser pulse through a gas target. The current energy record is set at 7.8 GeV and was reached over an acceleration distance of only 20 cm [21]. Due to their much greater particle mass, acceleration of protons and heavier ions has turned out to be more challenging and often requires the energy to be transferred to the ions via electrons as intermediaries. Because ions react more slowly to the field, ion acceleration, as opposed to electron acceleration, often involve laser interaction with solid targets. This allows stronger fields to be sustained for a longer time. The experimentally most accessible ion acceleration scheme is currently *target normal sheath acceleration* (TNSA), which has been able to accelerate protons to about 100 MeV [22].

One of the near-term goals of laser-based electron acceleration is the generation of monoenergetic, 10 GeV electron bunches of 100 pC charge in a single acceleration stage. This is to be used as the primer in staged wakefield acceleration, expected to allow for a continued efficient acceleration to much greater energies. The hope is to eventually be able to couple this to a future laser-based acceleration scheme tailored for positrons, in order to create a compact electron-positron collider [23]. For laser-based ion acceleration, the

holy grail has for a long time been the prospect of a compact particle source for hadron therapy [24]. Achieving this would require high-quality proton bunches of tunable energy in the hundreds of MeV and at high repetition rates [25–29]. While multiple acceleration schemes have been proposed, the energies necessary for hadron therapy have experimentally remained out of reached. Nevertheless, progress have been made in a number of areas [30, 31], and the usefulness of laser-driven ion sources have been demonstrated in other applications, such as various imaging techniques [32–34] and isochoric heating of matter [35]. In moving towards new technologies, these sources do not only require higher energies, but improvements to energy conversion efficiency, beam divergence and spectral control will also be important, not to mention increased particle numbers and improved shot-to-shot stability.

1.3 Outline

This thesis is written with the aim of providing an introduction to the topics of plasma and high-intensity laser physics sufficient for the interested reader to understand the publications on which the thesis is based. The primary assumption is that the reader has a solid background in physics, but not necessarily within plasma physics or on the topic of radiation reaction. We therefore begin by covering some key concepts of plasma physics in Chapter 2 and while some of the presented equations will not be revisited, they are important in understanding the basis for the numerical approaches on which much of this thesis relies. In Chapter 3 the basics of intense laser-matter interaction is presented, with the aim of guiding the reader through the ideas that has enabled laser-driven ion acceleration. It begins by covering single particle dynamics in strong fields, before it transitions to a discussion on plasma-based acceleration mechanisms and the results of Paper A. Chapter 4 introduces the recently proposed laser-driven ion acceleration scheme studied in Paper B, chirped-standing-wave acceleration. The formulation of the acceleration scheme is motivated drawing upon the shortcomings of the schemes discussed in Chapter 3, and its operation is described in detail.

For the uninitiated reader, Chapter 5 covers the basic principles behind radiation emission in strong background fields and the backreaction on a radiating particle. Starting from synchrotron radiation and classical radiation reaction, the ultimate need for a quantum description is motivated. At the end of the chapter the dominant QED effects in strong fields, of photon emission and electron-positron pair production, are detailed. In Chapter 6 we discuss the balance between photon emission and pair production, and the resulting importance of the field geometry, for an efficient generation of high-energy photons, as investigated in Paper C. A particular field geometry considered in Paper C, and further studied in Paper D, is also introduced. This geometry, formally that of a dipole wave, corresponds to an optimal

focusing of laser radiation, maximizing the intensity for a given laser power. It is discussed in relation to its role as a potential photon source, but also for studying more exotic phenomena such as electron-positron pair cascades.

Chapter 7 introduces the particle-in-cell approach and describes how it is used for efficient, large-scale plasma simulations. The classical scheme is in Section 7.2 followed by a description of an advanced extension, named QED-PIC, necessary to more accurately capture the particle dynamics in particularly strong fields.

Finally, the reader should note that the system of units used in equations throughout this thesis is that of Gaussian CGS, unless explicitly written otherwise. This fact also includes the papers covered in this thesis. Where applicable, the metric tensor can be assumed to have the signature $(+,-,-,-)$.

Chapter 2

Introduction to plasma physics

A *plasma* is an *ionized gas* and it is often referred to as the fourth state of matter, after *solid*, *liquid* and *gas*, as illustrated in Figure 2.1. Despite this rather unremarkable characterization, plasma is by far the most abundant phase of ordinary matter in the universe. This is not less true in our own solar system where most of the matter is contained in the sun, which can be thought of as a gravitationally confined plasma.

Artificially produced plasmas can be found in a large number of applications ranging from plasma displays, rocket ion thrusters, gas-discharge lamps, fusion energy and plasma torches used in plasma cutting and plasma arc welding. These plasmas exhibit a large number of complex phenomena and their properties depend on parameters such as the plasma density and temperature.

2.1 General properties

The fundamental building blocks of a plasma are freely moving and electrically charged particles, usually electrons and (at least partially ionized) ions. These particles are *free* in the sense that they are not atomically bound to each other and the fact that the particles in the plasma are charged gives it properties that are vastly different from that of a gas. The motion of the charged particles gives rise to electromagnetic (EM) fields, and these fields will in turn affect the motion of the particles. As a result, this interplay between the charged particles and the fields leads to a variety of complex collective behaviours, which can be viewed as defining features of a plasma.

Despite being made up of charged particles the plasma is often *quasi-neutral*, meaning that it is neutral only on a macroscopic scale. This property arises due to the fact that any separation of charge will give rise to a field that, when acting on the surrounding charges, drives the particles in such

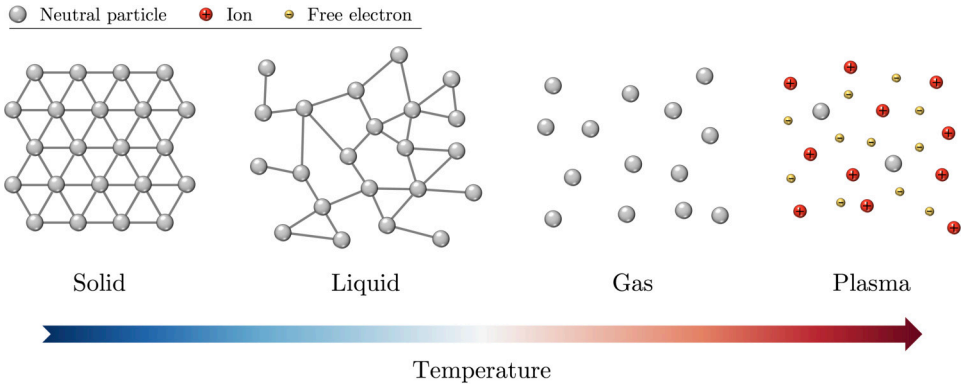

Figure 2.1: Illustration of the four most common states of matter, ordered from left to right by increasing temperature.

a way as to cancel the field, and thereby making the plasma quasi-neutral. The characteristic time scale for this to occur is one of the most important parameters of the plasma. For a non-collisional plasma and neglecting the motion of the ions, because of their much larger inertia compared to the electrons, this characteristic time scale can easily be obtained by calculating the oscillation frequency of an electron slab displaced from equilibrium. This frequency is called the (electron) *plasma frequency*

$$\omega_p = \sqrt{\frac{4\pi n_e e^2}{m_e}}, \tag{2.1}$$

where n_e is the unperturbed electron density, $-e$ the electron charge and m_e the electron mass, and it determines the rate at which the plasma responds to local charge density fluctuations.

The tendency of a plasma to cancel out electric fields, and thereby establish quasi-neutrality, can further be described by the fundamental plasma property of *Debye shielding* or *screening*. Because of this tendency, the electric potential of a test charge located inside the plasma would effectively be screened by the surrounding plasma over some characteristic length scale. This length scale is called the *Debye length* [36] and is, again assuming immobile ions, given by

$$\lambda_D = \sqrt{\frac{k_B T_e}{4\pi n_e e^2}}, \tag{2.2}$$

where k_B is Boltzmann's constant and T_e is the electron temperature. The effective potential of the screened test charge thereby becomes proportional to $\exp(-r/\lambda_D)/r$, decaying exponentially faster than if it was unscreened, as shown in Figure 2.2(a). Together, equations (2.1) and (2.2) define the temporal and spatial scales of the interactions in a simple, non-collisional plasma and must be considered when modelling the plasma, in order to correctly capture its collective behaviour.

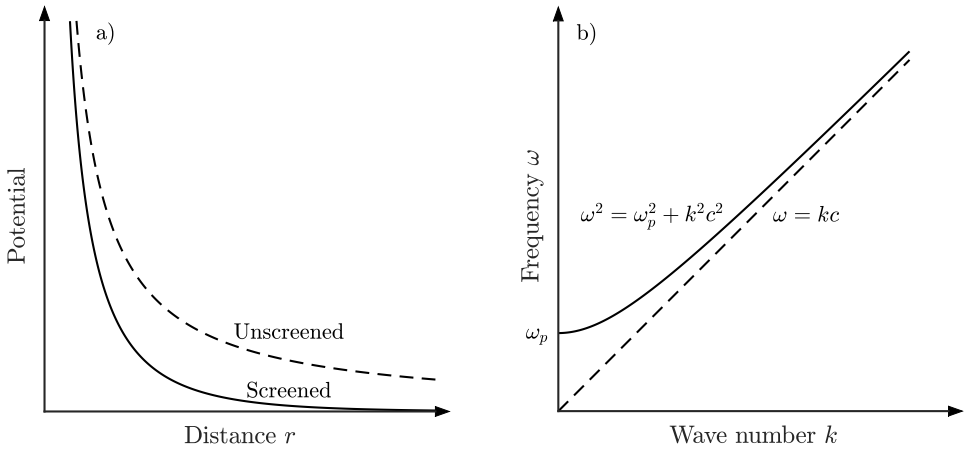

Figure 2.2: (a) The electric potential of a charged particle with (solid) and without Debye screening (dashed) and (b) the dispersion relation of the electromagnetic wave in a plasma (solid) and in vacuum (dashed).

Studies of plasmas generally look at how a plasma behaves under various conditions or responds to external influence. For the interaction of a plasma with laser radiation the response of the plasma can be separated into two major regimes, depending on the frequency of the plasma compared to that of the incoming radiation. To see this, it is sufficient to look at the dispersion relation for waves propagating in a cold and unmagnetized plasma, *i.e.*, containing no background magnetic field. For transverse electromagnetic waves, such as light, propagating in this plasma the dispersion relation is given by

$$\omega^2 = \omega_p^2 + k^2c^2, \tag{2.3}$$

where k is the wave number and ω is the frequency of the wave, and is shown in Figure 2.2(b). We see that these waves only propagate in the plasma if their frequency is greater than the plasma frequency ω_p. If it is instead smaller than the plasma frequency, the wave number becomes purely imaginary, indicating an exponential decay. Put in a different way, if the plasma frequency ω_p is smaller than the frequency of incoming radiation ω_0, then the characteristic time scale of the plasma is longer than the optical period of the incoming radiation. The plasma can therefore not respond quickly enough to stop the propagation of the electromagnetic wave and is thus transparent to it, or *underdense*. In the opposite case, when the plasma frequency is greater than that of the incoming radiation, the characteristic time scale of the plasma is short enough for it to respond to the incoming wave. This response is generally such that it cancels the field in the bulk of the plasma, typically leading to the reflection of the external radiation at the plasma boundary. The plasma thus appear opaque to this radiation and is said to be *overdense*. The natural separation of these two regimes occur

when the plasma frequency is equal to that of the incoming radiation and the corresponding *critical density* can, through equation (2.1), be defined as

$$n_{\mathrm{cr}} = \frac{m_e \omega_0^2}{4\pi e^2}. \tag{2.4}$$

Plasmas with densities close to this critical density generally exhibit strong resonance effects in their interaction with the incoming radiation and are typically referred to as *near-critical*. Finally, it should be noted that plasmas allow for several wave modes beyond the one considered here and although important in describing a number of plasma phenomena, these will not be examined further in this thesis.

2.2 Electromagnetic fields

The classical theory of electrodynamics has been one of the most successful areas of not only physics, but science in general, since its birth around the start of the nineteenth century. It rests on *Maxwell's equations*, describing the evolution and generation of electric and magnetic fields by charges and currents, and the *Lorentz force*, describing the force acting upon charged particles by the electric and magnetic fields. Written in vector notation, Maxwell's equations read [37]

$$\nabla \cdot \mathbf{E} = 4\pi\rho \tag{2.5a}$$
$$\nabla \cdot \mathbf{B} = 0 \tag{2.5b}$$
$$\nabla \times \mathbf{E} = -\frac{1}{c}\frac{\partial \mathbf{B}}{\partial t} \tag{2.5c}$$
$$\nabla \times \mathbf{B} = \frac{4\pi}{c}\mathbf{J} + \frac{1}{c}\frac{\partial \mathbf{E}}{\partial t} \tag{2.5d}$$

where $\mathbf{E}$ and $\mathbf{B}$ are the electric and magnetic fields, $\mathbf{J}$ and ρ are the current and charge densities and c is the speed of light. Separately, equations (2.5a), (2.5c) and (2.5d) are named Coulomb's law (or Gauss' law), Ampère's law and Faraday's law respectively. The remaining equation (2.5b) is typically referred to as the absence of (free) magnetic charge (but occasionally also called Gauss' law for magnetism). Similarly, the Lorentz force is given by

$$\mathbf{F} = q\left(\mathbf{E} + \frac{\mathbf{v}}{c} \times \mathbf{B}\right), \tag{2.6}$$

where $\mathbf{F}$ is the force, due to the electromagnetic fields, acting on a particle of charge q and moving with velocity $\mathbf{v}$.

The electromagnetic fields store energy and the transfer of this energy and transformation into other forms is often of great interest. The energy stored in the fields is described by the electromagnetic energy density

$$u = \frac{1}{8\pi}\left(\mathbf{E}^2 + \mathbf{B}^2\right), \tag{2.7}$$

and the directional flux of electromagnetic energy is similarly given by the *Poynting vector* [38]

$$\mathbf{S} = \frac{c}{4\pi}\mathbf{E} \times \mathbf{B}. \tag{2.8}$$

The electromagnetic energy density and the Poynting vector can further be related through a statement of energy conservation of the electromagnetic fields known as *Poynting's theorem*,

$$\frac{\partial u}{\partial t} + \nabla \cdot \mathbf{S} = -\mathbf{J} \cdot \mathbf{E}, \tag{2.9}$$

which relates the flux of electromagnetic energy to the work done on electric charges. The total energy content of a localized electromagnetic pulse, at a given instance, can therefore be obtained by simple integration of equation (2.7) over space. While this tells us a global property of the fields, it gives little information about the strength of the fields or the flux of energy. It is therefore often more important to know the *intensity* of the fields, or their *power*. The intensity of the electromagnetic fields is simply the (cycle-averaged) magnitude of the Poynting vector,

$$I = \langle |\mathbf{S}| \rangle, \tag{2.10}$$

describing the flux of energy per unit time and unit area. It can also be defined along a given direction $\hat{\mathbf{n}}$ as $I = \langle \mathbf{S} \cdot \hat{\mathbf{n}} \rangle$. The power of the fields, on the other hand, describe the flux of energy through some surface $\mathcal{S}$ per unit time, and is therefore related to the Poynting vector through integration over this surface,

$$P = \int_{\mathcal{S}} \mathbf{S} \cdot \mathrm{d}\mathbf{A}. \tag{2.11}$$

2.3 Plasma descriptions

There are several ways in which a plasma can be modelled and which description is the most appropriate generally depend on the specific scenario. Most commonly used are the *kinetic* and *fluid* descriptions. These two are usually complemented by the *single-particle* description, in which the dynamics of individual particles are studied in an external field, neglecting their own contribution to the field. While this description is not technically that of a plasma, it is often used for back-of-the-envelope calculations and can still provide valuable information, especially when dealing with particles in strong background fields.

2.3.1 Kinetic description

In kinetic theory the plasma is described by a set of (single-particle) distribution functions $f_s(\mathbf{r}, \mathbf{v}, t)$ representing the distribution of particles of species

s, at position $\mathbf{r}$ and with velocity $\mathbf{v}$. The set of all positions $\mathbf{r}$ and velocities $\mathbf{v}$ (or, alternatively, particle momenta $\mathbf{p}$) is called the *phase space* of the system and is in general six-dimensional. More formally, $f_s(\mathbf{r}, \mathbf{v}, t)$ gives the probability of finding a particle of species s in a neighbourhood of (within the phase space volume $\mathrm{d}^3\mathbf{r}\,\mathrm{d}^3\mathbf{v}$) the phase space point $(\mathbf{r}, \mathbf{v})$, at time t. The dynamics of such a system can be described by the *Boltzmann equation*

$$\frac{\mathrm{d}f_s}{\mathrm{d}t} = \frac{\partial f_s}{\partial t} + \mathbf{v} \cdot \frac{\partial f_s}{\partial \mathbf{r}} + \frac{\mathbf{F}}{m_s} \cdot \frac{\partial f_s}{\partial \mathbf{v}} = \left(\frac{\partial f_s}{\partial t}\right)_{\text{coll}}, \tag{2.12}$$

where $\mathbf{F}$ is the force acting upon the particle, m_s is its mass and $f_s = f_s(\mathbf{r}, \mathbf{v}, t)$ for brevity. The right-hand side describes the effect of collisions between particles and can be quite complex, requiring additional knowledge of the statistics obeyed by the particles, and can make the Boltzmann equation difficult to solve.

In weakly coupled plasmas where the effect of collisions is small compared to the collective plasma effects, the right hand side of equation (2.12) can be neglected. This brings us to one of the most important equations in plasma physics, the *Vlasov equation* [39, 40],

$$\frac{\partial f_s(\mathbf{r}, \mathbf{v}, t)}{\partial t} + \mathbf{v} \cdot \frac{\partial f_s(\mathbf{r}, \mathbf{v}, t)}{\partial \mathbf{r}} + \frac{q_s}{m_s}\left(\mathbf{E} + \frac{\mathbf{v}}{c} \times \mathbf{B}\right) \cdot \frac{\partial f_s(\mathbf{r}, \mathbf{v}, t)}{\partial \mathbf{v}} = 0, \tag{2.13}$$

where the Lorentz force from equation (2.6) has now been written out explicitly. The Vlasov equation can be solved self-consistently together with Maxwell's equations, (2.5a)–(2.5d), where the charge density ρ and current density $\mathbf{J}$ are given by

$$\rho(\mathbf{r}, t) = \sum_s q_s \int f_s(\mathbf{r}, \mathbf{v}, t)\,\mathrm{d}^3\mathbf{v} \tag{2.14}$$

and

$$\mathbf{J}(\mathbf{r}, t) = \sum_s q_s \int \mathbf{v} f_s(\mathbf{r}, \mathbf{v}, t)\,\mathrm{d}^3\mathbf{v}, \tag{2.15}$$

respectively.

2.3.2 Fluid description

In the fluid description the plasma is modelled as a set of interpenetrating fluids, one for each particle species in the plasma, by looking at macroscopic quantities. The fluid equations can be derived from kinetic theory by taking *velocity moments* of the governing kinetic equation (e.g. the Boltzmann or Vlasov equation) and where the n-th moment of f_s can be found by integrating $\mathbf{v}^n f_s$ over velocity space to obtain macroscopic quantities such as the particle number density n_s and mean velocity $\mathbf{v}_s$ of species s. These macroscopic quantities are functions of coordinate space and time, and the

fluid description is therefore a simplification of the kinetic description, as the resulting fluid equations are three-dimensional.

Unless truncated by the use of some additional information, taking the moments of the kinetic equation would produce an infinite series of equations. Instead, the moments are closed using a constitutive relation that further ties the moments together, often limiting the number of moment equations to two or three. As an example, integrating the Vlasov equation over all of velocity space gives us the zeroth order moment equation, the *continuity equation*,

$$\frac{\partial n_s}{\partial t} + \nabla \cdot (n_s \mathbf{v_s}) = 0, \tag{2.16}$$

which with the vanishing right-hand side describes that the fluid is conserved, meaning it can neither be created nor destroyed. Instead multiplying the Vlasov equation by $\mathbf{v}$ and again integrating over velocity space gives us the first order moment equation, the *momentum equation*,

$$\frac{\partial \mathbf{v}_s}{\partial t} + (\mathbf{v}_s \cdot \nabla)\mathbf{v}_s = \frac{q_s}{m_s}\left(\mathbf{E} + \frac{\mathbf{v}}{c} \times \mathbf{B}\right) - \frac{\nabla \cdot \mathbf{P}_s}{m_s n_s}, \tag{2.17}$$

where $\mathbf{P}_s$ is the pressure tensor, representing the equation of motion of the fluid of species s. Assuming f_s is isotropic, the last term can be simplified to $\nabla \cdot \mathbf{P}_s = \nabla p_s$ where p_s is the scalar pressure. The fluid equations are then often truncated by for example assuming an adiabatic flow, thus turning the second order moment equation into an *equation of state* for the pressure

$$p_s n_s^{-\gamma_s} = \text{const}, \tag{2.18}$$

where γ_s is the adiabatic index.

So far, we have described each particle species of the plasma in terms of a separate fluid. By making additional assumptions on the particle distribution functions and scale lengths of the plasma, for example being dominated by collisions, it can instead be modelled as a single fluid. This one-fluid model is also referred to as the *magnetohydrodynamic* (MHD) model [41] and describes the plasma as a single conducting medium, represented by combined macroscopic quantities like the mass density ρ_m, charge density ρ, center-of-mass velocity $\mathbf{V}$, and the electric current density $\mathbf{J}$. The MHD theory is widely used for modelling and describing interstellar plasmas and astrophysical phenomena, magnetically confined fusion plasmas as well as stellar and planetary interiors.

While the fluid description provides a set of equations of reduced dimensionality compared to the kinetic description, making studies of large-scale systems more tractable, the simplifications unavoidably also make it restricted in scope. Because the dynamical dependence on the velocity distribution is fully neglected (strictly speaking, it often assumes a Maxwellian distribution), fluid theory is unable to correctly capture the physics in systems with strong kinetic effects. One of the earliest and most well-known

examples of such an effect is *Landau damping* [42], in which plasma waves are damped through an interplay between the wave and particles of different velocities. In such cases, solving the kinetic equations of kinetic theory is usually the only reliable option.

Chapter 3

Laser-plasma interactions

In the following chapter we present basic particle dynamics in intense electromagnetic fields as well as common particle acceleration mechanisms of intense laser-plasma interaction. The main focus of the text is on the question of how laser energy can be transferred to charged particles. In relation to this, we summarize the results of Paper A [43], where we study the interaction of an intense laser and a plasma slab with periodic surface structures.

3.1 Single-particle motion in intense fields

Before discussing the interaction of intense laser fields with plasmas it is instructive to first study single-particle dynamics in such fields, as well as define what we actually mean by *intense*. In doing so we will derive some basic properties of importance for the subsequent discussion. More detailed analysis can be found in common textbooks covering the topic [37, 44–46].

3.1.1 Non-relativistic motion in a plane wave

We begin by looking at the simple case of a charged particle oscillating non-relativistically in a propagating plane wave field. Assuming that the wave is propagating in the x-direction we may write the electric and magnetic fields as

$$\mathbf{E}(x,t) = E_0\hat{\boldsymbol{\varepsilon}}\mathrm{e}^{i(kx-\omega t)}, \quad \mathbf{B}(x,t) = \hat{\mathbf{x}} \times \mathbf{E}(x,t), \tag{3.1}$$

where E_0 is the field amplitude, ω the frequency, $k = \omega/c$ the wave number and $\hat{\boldsymbol{\varepsilon}}$ the polarization vector. That the real physical values are obtained from the real part of the expression is left implicit. The equations of motion for a non-relativistic charged particle under the influence of these fields are simply obtained from the Lorentz force (2.6),

$$m\frac{\mathrm{d}\mathbf{v}}{\mathrm{d}t} = q\left(\mathbf{E}(\mathbf{r},t) + \frac{\mathbf{v}}{c} \times \mathbf{B}(\mathbf{r},t)\right), \quad \frac{\mathrm{d}\mathbf{r}}{\mathrm{d}t} = \mathbf{v}, \tag{3.2}$$

where m and q is the mass and charge of the particle, respectively, and where both its position $\mathbf{r}$ and velocity $\mathbf{v}$ are functions of time. For non-relativistic particle motion the speed of the particle is much smaller than the speed of light, $|\mathbf{v}| \ll c$, and the $\mathbf{v} \times \mathbf{B}$ term can therefore be neglected. The solution to equation (3.2) is in this limit given by

$$\mathbf{v} = \frac{iq}{m\omega}\mathbf{E}, \quad \mathbf{r} = -\frac{q}{m\omega^2}\mathbf{E}. \tag{3.3}$$

In order for the assumption of non-relativistic particle motion to hold true we must now require that $|\mathbf{v}| = |q|E_0/m\omega \ll c$, which puts restrictions on the field amplitude E_0. Introducing the dimensionless parameter $a_0 = |q|E_0/m\omega c$, our assumption holds true for $a_0 \ll 1$, and particle motion generally becomes relativistic and non-linear for $a_0 \gtrsim 1$, defining what we call the *relativistic regime*. Electrons (and positrons), which have the largest charge-to-mass ratio among the charged particles, will therefore reach this relativistic regime for the lowest field amplitudes. For intense laser pulses this dimensionless parameter is therefore generally defined in terms of the charge and mass of the electron and is called the *normalized laser amplitude*,

$$a_0 = \frac{eE_0}{m_e\omega_0 c}, \tag{3.4}$$

where ω_0 is the laser frequency.

In order to relate the normalized laser amplitude to something more tangible we can further calculate the intensity of the plane wave using equation (2.10). Assuming that the wave is linearly polarized, its cycle-averaged intensity becomes

$$I = \frac{c}{4\pi}\langle|\mathbf{E} \times \mathbf{B}|\rangle = \frac{cE_0^2}{8\pi} = \frac{c}{8\pi}\left(\frac{m_e\omega_0 c}{e}\right)^2 a_0^2. \tag{3.5}$$

Using this expression, the normalized laser amplitude can be expressed in more common physical units as

$$a_0 = 0.85\sqrt{\left(\frac{I}{10^{18}\,\mathrm{W/cm^2}}\right)\left(\frac{\lambda^2}{1\,\mu\mathrm{m}^2}\right)}, \tag{3.6}$$

where $\lambda = 2\pi c/\omega_0$ is the laser wavelength. As an attribute of a laser field, *intense* is therefore used to describe the ability of the field to induce relativistic motion of electrons. For present state-of-the-art laser systems, often operating at 10^{20}–$10^{21}\,\mathrm{W/cm^2}$ and with a typical wavelength of $0.81\,\mu\mathrm{m}$, it is possible to achieve $a_0 \sim 10$, which is well into the relativistic regime.

3.1.2 Relativistic motion in a plane wave

The motion of a charged particle in an intense field can, in fact, be solved exactly for arbitrary field amplitudes, without having to resort to the approximations used in the previous section. While this can be done by solving

the equations of motion directly given by the Lorentz force, we will do it by instead deriving the constants of motion through the Lagrangian and Hamiltonian formalisms. In doing so, we introduce the field potentials,

$$\mathbf{B} = \nabla \times \mathbf{A}, \quad \mathbf{E} = -\nabla\phi - \frac{1}{c}\frac{\partial \mathbf{A}}{\partial t}, \tag{3.7}$$

where ϕ and $\mathbf{A}$ is the scalar and vector potential, respectively, and as will become apparent, the constants of motion can be easily expressed in terms of these potentials.

The Lagrangian L of a relativistic charged particle in an electromagnetic field, expressed through its potentials, is given by [37, 46–48]

$$L = -mc^2\sqrt{1 - \frac{\mathbf{v}^2}{c^2}} - q\phi + q\mathbf{A}\cdot\frac{\mathbf{v}}{c} \tag{3.8}$$

and the particle has a canonical momentum $\tilde{\mathbf{p}}$ of

$$\tilde{\mathbf{p}} \equiv \frac{\partial L}{\partial \mathbf{v}} = \mathbf{p} + \frac{q}{c}\mathbf{A}, \tag{3.9}$$

where $\mathbf{p} = \gamma m\mathbf{v}$ is the linear momentum and $\gamma = (1 - \mathbf{v}^2/c^2)^{-1/2}$ the Lorentz factor of the particle. For a propagating monochromatic plane wave the potentials can be expressed as functions purely dependent on the phase $t - r_\parallel/c$, where $r_\parallel$ is the longitudinal coordinate and t is time. Due to gauge invariance, it is also possible to choose the potentials such that

$$\phi = 0, \quad \nabla\cdot\mathbf{A} = 0, \tag{3.10}$$

making the plane wave fully described by $\mathbf{A} = \mathbf{A}_\perp(t - r_\parallel/c)$ [46]. Since the Lagrangian is independent of the transverse coordinate $\mathbf{r}_\perp$ ($\partial L/\partial \mathbf{r}_\perp = 0$), the transverse canonical momentum $\tilde{\mathbf{p}}_\perp$ is conserved ($\mathrm{d}\tilde{\mathbf{p}}_\perp/\mathrm{d}t = 0$).

The second constant of motion can be found from the relation $\mathrm{d}H/\mathrm{d}t = -\partial L/\partial t$ between the Hamiltonian and the Lagrangian. The Hamiltonian is given by [47, 48]

$$H(\mathbf{r}, \tilde{\mathbf{p}}, t) \equiv \mathbf{v}\cdot\tilde{\mathbf{p}} - L = \gamma mc^2, \tag{3.11}$$

and describes the energy of the electron. Through the aforementioned relation we obtain

$$\frac{\mathrm{d}H}{\mathrm{d}t} = -\frac{\partial L}{\partial t} = c\frac{\partial L}{\partial r_\parallel} = c\frac{\mathrm{d}}{\mathrm{d}t}\frac{\partial L}{\partial v_\parallel} = c\frac{\mathrm{d}\tilde{p}_\parallel}{\mathrm{d}t}, \tag{3.12}$$

where the second equality comes from the fact that $\mathbf{A}$ is a function purely dependent on the phase. Our constants of motion can therefore be summarized as

$$\gamma mc - \tilde{p}_\parallel = \text{const}, \quad \tilde{\mathbf{p}}_\perp = \text{const}. \tag{3.13}$$

We may now proceed to determine these constants for a particular choice of initial conditions. Assuming that the particle in a distant past was at rest ($\mathbf{p} = 0$) and not subject to any field ($\mathbf{A} = 0$), the linear momentum, using equation (3.9), becomes

$$p_\parallel = (\gamma - 1)mc, \quad \mathbf{p}_\perp = -\frac{q}{c}\mathbf{A}. \tag{3.14}$$

Through the relativistic energy-momentum relation, these two momentum components are further related through

$$p_\parallel = \frac{\mathbf{p}_\perp^2}{2mc}. \tag{3.15}$$

Finally, we note that for a plane wave of frequency ω_0 the amplitude of the vector potential A_0 and the amplitude of the field E_0 are related as $E_0 = \omega_0 A_0/c$, (see eq. 3.7). The normalized laser amplitude (eq. 3.4) can thus be expressed as $a_0 = eA_0/m_e c^2$ and is therefore sometimes called the *normalized vector potential*. Thus normalizing the vector potential $\mathbf{a} = e\mathbf{A}/m_e c^2$ allows us to summarize the equations of motion as

$$\frac{\gamma}{c}\frac{\mathrm{d}r_\parallel}{\mathrm{d}t} = \frac{\mathbf{a}^2}{2}, \quad \frac{\gamma}{c}\frac{\mathrm{d}\mathbf{r}_\perp}{\mathrm{d}t} = -\frac{q}{e}\mathbf{a}, \quad \gamma = 1 + \frac{\mathbf{a}^2}{2}. \tag{3.16}$$

Solving the equations of motion becomes straight-forward by changing the integration variable to $\tau = t - x/c$, through which

$$\frac{\mathrm{d}\tau}{\mathrm{d}t} = 1 - \frac{v_\parallel}{c} = 1 - \frac{p_\parallel}{\gamma mc} = 1 - \frac{(\gamma - 1)mc}{\gamma mc} = \frac{1}{\gamma}. \tag{3.17}$$

We now look at the special case of an electron in a linearly y-polarized plane wave of frequency ω_0 propagating in the x-direction. The corresponding vector potential is given by $\mathbf{a} = (0, a_0, 0)\cos(\omega_0\tau)$, for which the solution becomes

$$x = \frac{a_0^2}{4}\left(c\tau + \frac{c}{2\omega_0}\sin 2\omega_0\tau\right), \quad y = a_0\frac{c}{\omega_0}\sin\omega_0\tau, \quad z = \text{const.} \tag{3.18}$$

The resulting motion is thus seen to be composed of two parts, the first of which is a constant drift in the longitudinal direction. From the cycle-averaged motion, the drift velocity v_d is readily obtained to be

$$v_d = \frac{a_0^2}{4 + a_0^2}c. \tag{3.19}$$

This drift is superimposed by a *figure-of-eight* oscillation, as the electron is oscillating with frequency ω_0 in the polarization direction and with frequency $2\omega_0$ in the longitudinal direction. This figure-of-eight motion can be seen in a frame moving in the longitudinal direction with the drift velocity v_d and,

by performing an appropriate Lorentz boost to this frame, the corresponding longitudinal motion can be shown to be described by [45]

$$x' = \frac{a_0^2}{8\gamma_0}\frac{c}{\omega_0'}\sin 2\omega_0\tau, \tag{3.20}$$

where $\gamma_0 = 1 + a_0^2/2$ and where x' is the longitudinal position and ω_0' the frequency as seen in the drift frame.

The electron dynamics described in equations (3.18) and (3.20) are presented in Figure 3.1. The motion of an electron in a circularly polarized plane wave, $\mathbf{a} = a_0(0, \cos(\omega_0\tau), \sin(\omega_0\tau))/\sqrt{2}$, is also included in Figure 3.1(c). It is interesting to note that the square of the vector potential is constant, $\mathbf{a}^2 = a_0^2/2$, in this circularly polarized field. This in turn leaves γ constant, making the equations of motion (3.16) easily solvable. The resulting electron motion is again composed of a constant longitudinal drift with a velocity v_d given by equation (3.19). However, there is no longitudinal oscillation in this field and the electron instead performs a simple circular motion in the transverse plane.

The longitudinal motion of a charged particle in a plane wave field comes from the $\mathbf{v} \times \mathbf{B}$ term of the Lorentz force. However, in spite of this longitudinal motion, if the field was to slowly decay over time the particle would eventually come to a halt, as can be deduced from the constants of motion. This implies that, under these conditions, no net acceleration can be obtained in a laser field of finite duration, a fact that is often refered to as the Lawson-Woodward theorem [49–52]. Fortunately, because realistic laser fields also carry a finite amount of energy, they unavoidably contain spatial gradients in violation of one of the underlying assumptions of the theorem, allowing for a net energy transfer from the laser field to a particle. In the interaction of a laser field with a plasma, the response of the plasma and its accompanying fields is non-negligible and provides further means for transferring energy. While of limited applicability, this simplified analysis provides important insights into charged particle dynamics in intense fields by illuminating several aspects that remain relevant to more complex scenarios.

3.1.3 Ponderomotive force

As demonstrated in the previous section, a charged particle in an oscillating electromagnetic field will be displaced in the polarization direction by the transverse electric field. If the field is inhomogeneous the displacement of the particle may move it to a region that is, on average, subject to a different field intensity. The average force experienced over the first half of the oscillation cycle is therefore not guaranteed to equal that of the second half. This causes the oscillation center of the particle to drift away from regions of higher intensity and toward regions of lower intensity. The drift motion

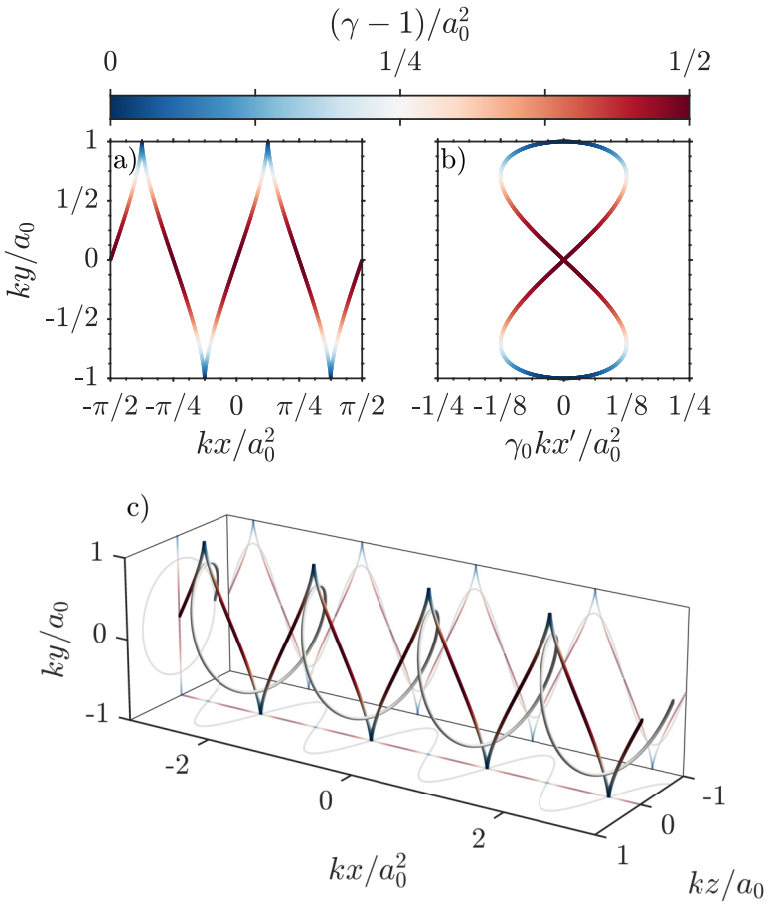

Figure 3.1: The universal trajectory of an electron in a plane wave field of arbitrary intensity. The electron motion in a linearly y-polarized field is presented both: (a, c) in the lab frame and; (b) in the drift frame moving with velocity v_d. (c) Further shows the electron trajectory in a circularly polarized plane wave field. The color scale shows the electron kinetic energy as seen in the lab frame.

of the oscillation center can be described by an effective force called the *ponderomotive force* $\mathbf{F}_\mathrm{p}$, obtained from the cycle-averaged Lorentz force.

For a monochromatic electromagnetic field of arbitrary space dependence, $\mathbf{E}(\mathbf{r},t) = \mathbf{E}_0(\mathbf{r})\cos(\omega t)$, the ponderomotive force on a non-relativistic charged particle is [45]

$$\mathbf{F}_\mathrm{p} = -\frac{q^2}{2m\omega^2}\nabla\langle\mathbf{E}^2\rangle, \tag{3.21}$$

which for electrons can be written as $\mathbf{F}_p = -m_e c^2 \nabla\langle\mathbf{a}^2\rangle/2$, where $\mathbf{a}$ is the corresponding normalized laser amplitude. The force retains this form also for propagating fields and is seen to always point away from regions of higher intensity ($I \sim \langle\mathbf{E}^2\rangle$) [44]. Interestingly, the force is proportional to the square of the charge and inversely proportional to the mass of the particle,

thereby affecting charges of opposite sign equally but heavier particles less strongly. For arbitrary field strengths the relativistic ponderomotive force, as seen in the oscillation center system, is similarly given by [44, 53]

$$\mathbf{F}_{\mathrm{p}}^{\mathrm{rel}} = -\nabla m_{\mathrm{eff}} c^2, \quad m_{\mathrm{eff}} \equiv m_e \sqrt{1 + \langle \mathbf{a}^2 \rangle}, \tag{3.22}$$

where m_{eff} is the *effective mass* of the oscillation center, which appears due to the particle's relativistic increase in inertia during its quiver motion. The corresponding expression valid in any inertial frame appears significantly more complicated and has been omitted for brevity but its derivation is found in Ref. [44, 53].

The drift motion described by the ponderomotive force allow charged particles to gain net energy through their interaction with an intense laser field, in contradiction to the Lawson-Woodward theorem, if their uphill acceleration is greater than their downhill deceleration. While this implication of the ponderomotive force is conceptually significant, it is important to remember that the force itself is merely manifestation of the average motion due to the underlying Lorentz force. As such, there are natural limitations to its applicability and since it formally only concerns the motion of the oscillation center, it will naturally be unable to fully capture the real particle dynamics.

3.2 Plasma-based acceleration

Up until this point, we have only discussed the acceleration of charged particles by intense fields in vacuum. While we have just shown such acceleration to be possible, direct vacuum acceleration is often impractical for most applications. The total charge which can be accelerated in such a way is often insufficient and without exact experimental control over parameters such as the laser pulse shape it becomes difficult to accelerate particles into a collimated, monoenergetic beam. Because laser fields in vacuum propagate at the speed of light, particles can not stay perfectly in phase with the field. Combined with the fact that intense laser fields in general are of very short in duration, this limits the total time a particle can spend in the field, in turn severely limiting the total acceleration.

To overcome the difficulties of vacuum acceleration one can instead consider the particles to be accelerated as part of a plasma, in which a laser field can induce collective acceleration through the response of the plasma to the field. Something very reminiscent of this idea was proposed as early as 1957 by Veksler [54], in which he envisaged acceleration of charged particles through *coherent motion*. While the exact details may differ, such "coherent acceleration" is achieved in the many plasma acceleration schemes existing today.

3.2.1 Electron acceleration

When an intense laser field interacts with a low-density material, such as a gas jet, an underdense plasma is formed. As the laser pulse propagates through the plasma, its propagation speed is slightly decreased, as indicated by the dispersion relation presented earlier, in equation (2.3). This makes it possible for particles to stay perfectly in phase with the field and significantly increases the interaction time between individual particles and the field, which was one of the major flaws of vacuum acceleration. As the pulse propagates through the plasma it also sets up collective plasma oscillations through which in particular electrons can be accelerated using the concept of *laser wakefield acceleration* (LWFA) [55–57].

The most successful variation of LWFA is the so called *bubble regime* [58, 59], in which the ponderomotive push (eq. 3.21) on the electrons is strong enough to create a cavity in the plasma, completely evacuated of all electrons. As the electrons are pulled back by the charge separation field a highly nonlinear wakefield is generated, trailing the evacuated region. Since the group velocity of the laser field in the plasma is lower than the speed of light, phase matching between the electrons and the laser-driven cavity becomes possible. As electrons are trapped in the trailing cavity and wakefield structure, they are able to gain significant amounts of energy in the process. There are several ways through which electrons can be injected into the cavity and when accelerated in this way have been shown to provide monoenergetic beams of electrons [60, 61]. This has allowed for the acceleration of ultra-short (femtosecond duration) electron bunches to above 1 GeV, over an acceleration distance of no more than a few centimeters [62].

3.2.2 Ion acceleration

For laser-driven acceleration of ions, where protons are the lightest and therefore the most mobile, the equations of motion are the same as for the much lighter electrons. However, because of the large difference in mass, $m_p/m_e \approx 1836$, where m_p is the proton mass, we see from the definition of the normalized laser amplitude (eqs. 3.4 and 3.6) that the intensity of the laser field would have to be more than six orders of magnitude greater in order to induce an equivalent relativistic motion of protons, implying intensities on the order of $10^{24}\,\mathrm{W/cm^2}$. For heavier ions the situation becomes even more challenging. Because ions are much less mobile than the lighter electrons, the acceleration gradients set up in an underdense plasma by an ultra-short laser field typically fade away well before the ions can gain any appreciable amount of energy. It should therefore not come as a surprise that ion acceleration, through laser wakefields, has proved more difficult to realize.

The issues just outlined do not spell the end of laser-driven ion acceleration and there is in fact a whole range of laser-plasma acceleration schemes specifically addressing ion acceleration [30, 31]. The most well-known ion acceleration schemes are target normal sheath acceleration (TNSA) [63–69], Coulomb explosion (CE) of clusters [70–72], double-layered targets [73–75], breakout afterburner (BOA) [76–78], hole boring [79], collisionless shock acceleration [80, 81], magnetic vortex acceleration [82, 83] and light sail or radiation pressure acceleration [84–87]. Common for most of these schemes is that they concern the interaction of intense laser fields with overdense (or at least near-critical) targets, allowing for the generation of more long-lived acceleration gradients, and the ions are generally accelerated *indirectly*, with the energy of the laser field being transferred to the ions via the electrons.

Among the ion acceleration schemes mentioned above, the most extensively studied and experimentally accessible is TNSA, wherein a thin foil is irradiated by an intense laser pulse. Because the target is overdense, the laser pulse can not propagate through the generated plasma. Instead, the electrons on the irradiated side are heated by the laser and travel through the target to its rear side. As the electrons cross the plasma-vacuum interface at the rear side of the target, the charge separation results in a strong electrostatic field through which ions can be accelerated. The scheme gets its name from the fact that the direction of this field is normal to the rear surface of the target, where an expanding sheath of plasma containing high-energy ions is formed and with the resulting ion beam being fairly well collimated along the target normal. Because they are the lightest, and through their presence via the pervasiveness of water contamination on target surfaces, the ions accelerated are predominantly protons.

Plasma heating and generation of hot electrons

The process by which the surface of a plasma is heated, creating the stream of *hot electrons* that later drives the ion acceleration in for example TNSA, is still not fully understood. These electrons are also said to be suprathermal, as their energies by far exceeds the temperature of the comparatively cool background plasma. Several mechanism have been proposed to explain the generation of these hot electrons, with varying degrees of success depending on the setup. The most commonly cited mechanisms are resonant absorption, Brunel heating [88] and "$\mathbf{J} \times \mathbf{B}$" heating [89].

In resonant absorption, the heating occurs through a resonant excitation of plasma oscillations at the critical density n_c, at which $\omega_0 = \omega_p$. The mechanism relies on the existence of a plasma density ramp, long enough for the definition of a local plasma density to make sense. In Brunel heating, initially proposed under the name "not-so-resonant" absorption, the plasma density gradient is instead assumed to be infinite, or close to it, such that a plasma surface can be imagined. Heating occurs as electrons are pulled

off the surface, into vacuum, and then accelerated back into the plasma. Because the plasma screens the external field, the electrons are released into the plasma with their vacuum energy. Both of these mechanisms relies on the electric field for excitation and acceleration, requiring p-polarized oblique incidence to provide an electric field normal to the plasma surface. When the field intensity is strong enough, the longitudinal (to the laser propagation direction) $\mathbf{v} \times \mathbf{B}$ force is comparable to the electric force. The third mechanism, "$\mathbf{J} \times \mathbf{B}$" heating, relies on vacuum heating similarly to the Brunel mechanism, but is instead driven by the longitudinal force due to the magnetic field. Both Brunel and "$\mathbf{J} \times \mathbf{B}$" heating are pulsed, at ω_0 and $2\omega_0$ respectively, which can be traced back to the periodicities of the transverse and longitudinal motions described by equation (3.18). If instead circularly polarized fields are considered the "$\mathbf{J} \times \mathbf{B}$" heating disappears, as they impose no oscillating longitudinal motion, reinforcing the general preference for linear polarization in all the aforementioned heating mechanisms.

Energy routes in target normal sheath acceleration

The energy of the laser pulse is under TNSA transferred to the ions in multiple stages, with electrons as intermediaries, as shown in Figure 3.2. Because we have little control over the progression of these stages, a considerable amount of the total energy is "lost" through a number of side channels. For example, instead of being absorbed by the hot electrons, parts of the laser radiation is simply reflected at the plasma-vacuum interface. Even if all the laser energy is absorbed, because of the transverse motion (to the target normal) of the hot electrons, some of the absorbed energy can not be transferred to the ions. Combined, these deficiencies has left TNSA insufficient for a number of potential applications. Considerable efforts have therefore been put into improving upon the shortcomings of the basic scheme.

In particular, there have recently been several studies investigating how microstructures on the target surface can be used to increase the maximum energy of the ions [90–98] as well as improve the collimation of the beam [99, 100]. Most of these studies focus primarily on how much of the laser energy can be transferred to the target and, by extension, to the ions. Because of the difficulty in disentangling the contribution of the various effects in this process, the performance of a particular modification is typically judged based the aggregated result, such as the maximum energy and total charge in the final ion beam. While this approach has lead to improvements in the parameters under consideration, the performance of TNSA remains insufficient. Since an absorption of practically 100% has been shown to be possible this leaves little room for further improvement along the same lines, and it instead becomes important to more fully understand the dynamics of the intermediaries, the hot electrons.

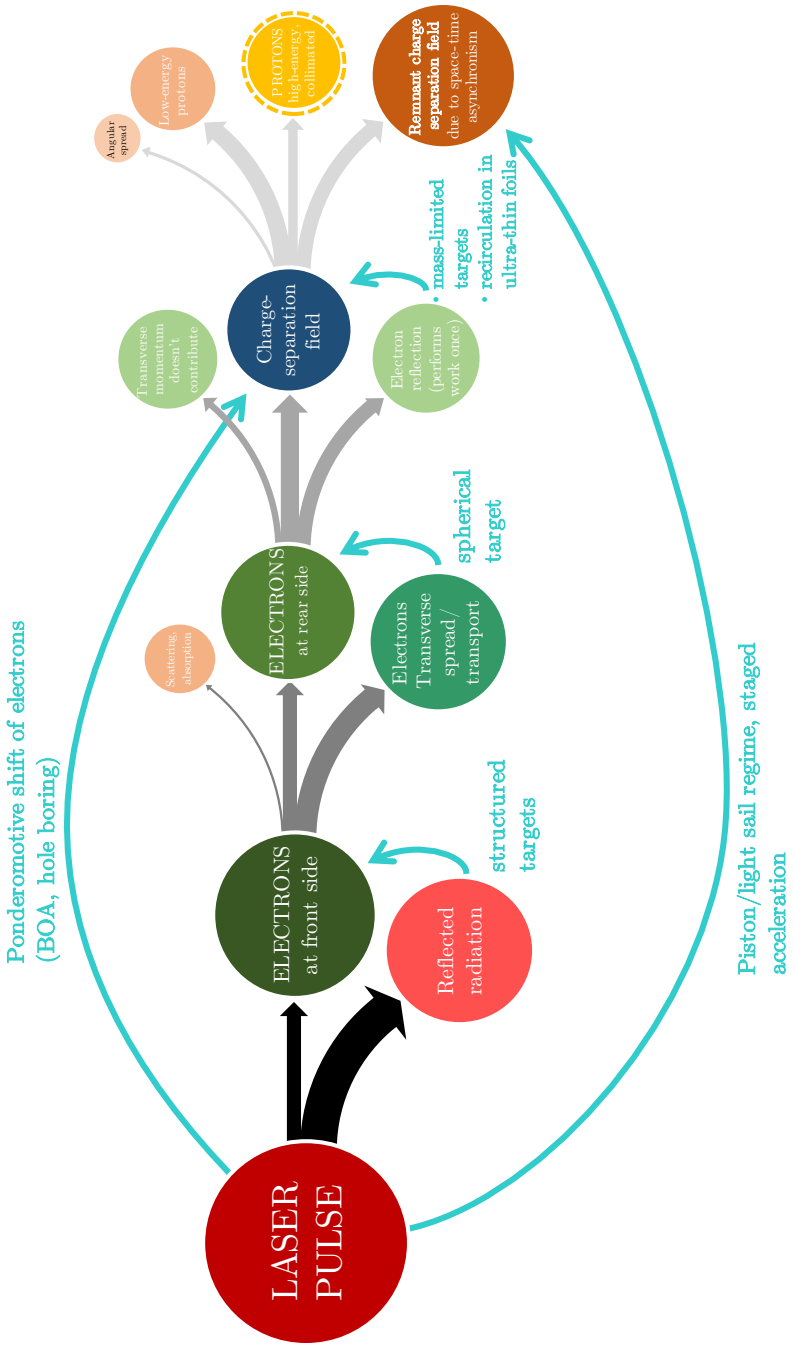

Figure 3.2: Schematic summary of the major energy routes present in target normal sheath acceleration. The process is accompanied by a number of side channels, which inhibits a perfect efficiency in the primary goal of transferring laser energy to high-energy protons. The impact of these side channels can be lessened with various target design choices, or through the use of more advanced acceleration schemes.

With this in mind, we have studied the dynamics of hot electrons in a number of systems, looking specifically at how the energy loss due to the transverse (to the target normal) transport of the electrons can be subverted. This loss occurs because at least a fraction of the hot electrons are generated with a transverse momentum. As the charge separation field on the rear side of the target is largely oriented along the target normal direction, this momentum component will remain unchanged. The hot electrons also do not impart all of their longitudinal energy to the charge separation field, but retain some of their energy as they are pulled back into the plasma. For sufficiently thin targets, allowing for a recirculation of the hot electrons, a greater portion of their energy can be imparted on the ions through the charge separation field. Despite this recirculation, the hot electrons will rapidly be transported away from the primary interaction region if their transverse momentum is too great. It can therefore be expected that ion energies will increase if, all else equal, the hot electrons are generated with a smaller transverse momentum or if their transverse propagation can be otherwise restricted, such that they contribute to the charge separation field in the primary interaction region for an extended period of time. The latter can be accomplished using so called mass-limited targets, in which the target is bounded in one or several transverse directions, forcing a transverse reflection of the hot electrons back into the primary interaction region.

In Paper A [43] we analyse how periodic structures affect the spectral properties of the generated hot electrons. The setup consists of a flat plasma slab irradiated at an angle θ by an intense laser field, as shown in Figure 3.3(a). In the absence of surface structures, the angular distribution of the hot electrons roughly follows

$$p_\perp = \frac{\sin\theta}{\cos^2\theta}\left(\sqrt{1+p_\parallel^2\cos^2\theta}-1\right), \tag{3.23}$$

where both the momentum transverse ($p_\perp$) and parallel ($p_\parallel$) to the target normal lies in the plane of incidence, Figure 3.3(b)-(c). We show that the addition of the periodic surface structures makes the angular distribution much wider and centers it closer the target normal direction, Figure 3.3(d)-(e). More importantly, the increase in absorbed laser energy due to these structures is shown to translate into an increased normal motion of the electrons. For applications such as TNSA, this potentially reduces the relative energy losses due to transverse electron motion. In studies of ion acceleration using microstructured targets, the increase in ion energies can therefore not purely be attributed to the increased absorption of laser radiation at the front surface, but is also supported by a more beneficial electron directionality.

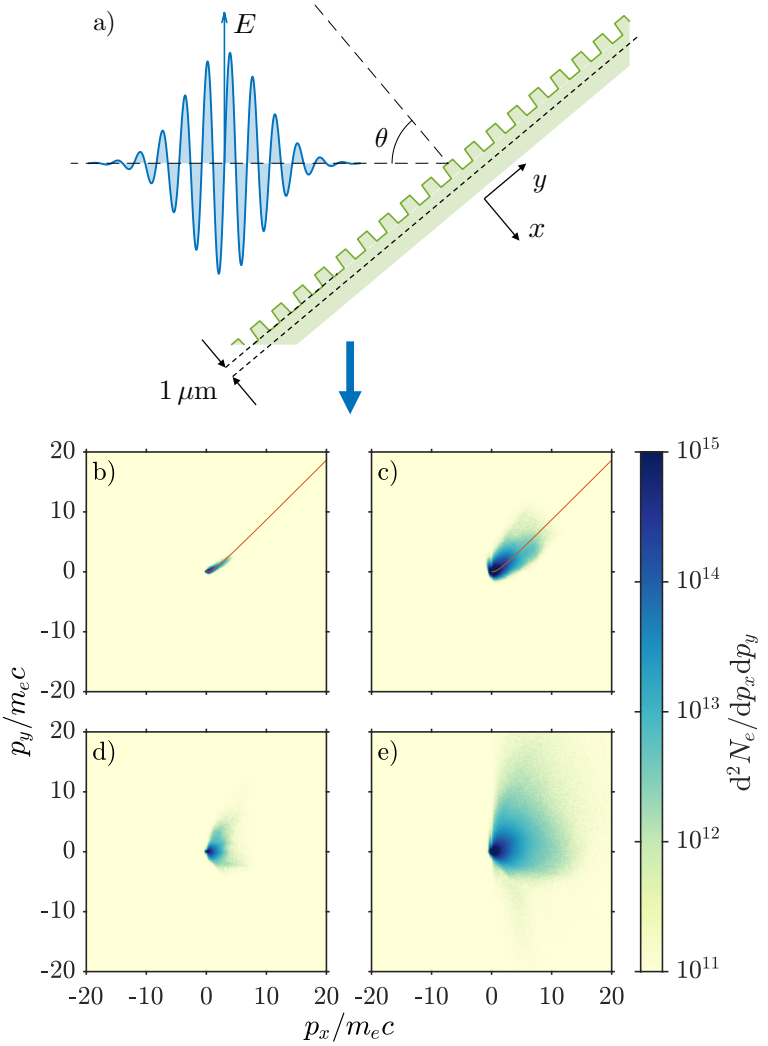

Figure 3.3: (a) The setup consists of a p-polarized Gaussian laser pulse with amplitude $a_0 = 6.3$ and duration $\tau_{\mathrm{FWHM}} = 40\,\mathrm{fs}$, incident on a microstructured, semi-infinite and overdense plasma at an angle to the target normal of θ. A virtual surface (dashed line), at which hot electron distributions are collected, is placed inside the plasma at a distance of 1 µm from the surface, not counting the height of the microstructures. The cumulative momentum space distribution of electrons transiting the virtual surface is shown for: (b, c) a flat foil and; (d, e) a foil with square microstructures with a period equal to the laser wavelength; when irradiated by a laser pulse incident at 45°. The momentum relation predicted by conservation of generalized momenta for an idealized flat foil (eq. 3.23) is indicated with a red line (b, c). The distributions are shown for two time instances, $t = 225\,\mathrm{fs}$ (b, d) and $t = 500\,\mathrm{fs}$ (c, e). The peak of the pulse reaches the surface at $t = 250\,\mathrm{fs}$.

Chapter 4

Chirped-standing-wave acceleration

The mechanisms enabling and ideas underpinning our current understanding of laser-driven ion acceleration was presented in Chapter 3. In this chapter we follow up on this topic and present the theoretical basis for a novel acceleration scheme originally proposed in Ref. [101], and further studied in Paper B [102]. This scheme was devised with the goal of providing a more controllable acceleration mechanism not relying on plasma heating, that is inherently insensitive to less controllable experimental conditions and with an uncomplicated initiation.

4.1 Motivating the need for a different scheme

Due to their inherent robustness the most experimentally accessible ion acceleration schemes are based on plasma heating as the primary stage in transferring laser energy to the kinetic energy of ions. Despite being experimentally accessible and sufficient for some applications, these schemes have intrinsic limitations that preclude meeting the requirements of more advanced applications. One of the fundamental reasons behind this is a lack of temporal control over the various acceleration stages, thereby providing us with no advanced means for a controlled conversion of laser energy into kinetic energy of ions moving in a chosen direction and with given energy.

The concept of *chirped-standing-wave acceleration* (CSWA) [101] was proposed in an attempt to overcome these difficulties and rests on the idea that in order to control the ion acceleration one must first control the motion of the electrons. This can be achieved by using one or several laser pulses to form a standing wave in which electrons can be trapped. The trapping occurs at the electric field node of the standing wave due to the ponderomotive potential and if this node were to move, the trapped electrons would move with it. Thus, by placing an ultra-thin foil in such a field, the ions in

the foil can be accelerated by the charge separation field formed between the electrons and ions as the electrons are continuously displaced by the movement of the node.

This node movement can be achieved in several ways, but the original idea of CSWA was to generate the standing wave using a single laser pulse reflected from a dense mirror, see Figure 4.1. By introducing a chirp to the pulse the position of the node can be made to move with respect to the mirror. Since the frequency is one of the most stable laser parameters, and the chirp of the pulse is relatively easy to control, this results in a tunable acceleration scheme. Furthermore, the locking of the electrons keeps instabilities from forming, which is a major hindrance for many other acceleration schemes. Finally, the laser pulse is circularly polarized in order to drive the electrons in a stable, circular motion. Compared to linear polarization, this restricts the motion of the electrons in the transverse plane, thereby further preventing the formation of instabilities.

4.2 Modelling the chirped laser pulse

Since the chirp of the laser pulse is central to the acceleration scheme, we begin by describing a simple model for a chirped laser pulse with a Gaussian temporal envelope. Assuming that we start out with an unchirped pulse of frequency ω_0, the longitudinal shape can be described by

$$\Psi(\eta) = \psi(\eta)\exp(i\omega_0\eta), \tag{4.1}$$

where the phase is given by $\omega_0\eta = \omega_0(t - x/c)$, and where $\psi(\eta)$ defines the longitudinal envelope. In frequency space, the oscillating term amounts to nothing but a shift of the spectrum

$$\hat{\Psi}(\omega) = \hat{\psi}(\omega - \omega_0), \tag{4.2}$$

where the hat symbolizes the Fourier transform of the function. Describing the envelope as a Gaussian, $\psi(\eta) = \exp(-a\eta^2)$, the frequency spectrum of our pulse is given by

$$\hat{\Psi}(\omega) = \sqrt{\frac{\pi}{a}}\exp\left[-(\omega - \omega_0)^2/4a\right], \tag{4.3}$$

where a can be related to the duration τ_0 of the laser pulse, or alternatively its bandwidth $\Delta\omega$. For laser pulses, these are most commonly expressed in terms of the *full-width at half-maximum* (FWHM) of their intensity

$$a = \frac{2\ln 2}{\tau_0^2} = \frac{\Delta\omega^2}{8\ln 2}. \tag{4.4}$$

A chirp can now be introduced by for example passing the pulse through a setup of gratings, similarly to how intense laser pulses can be stretched

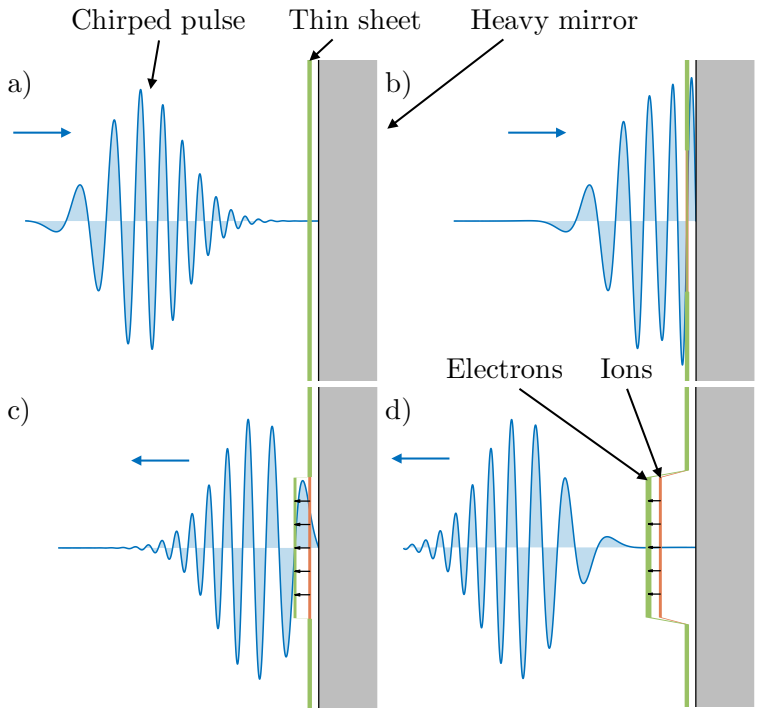

Figure 4.1: Schematic representation of the general scenario of the CSWA concept. (a) A chirped laser pulse incident on a high-density mirror with a thin overdense layer fixed in a position some distance from the mirror. (b) The pulse penetrates the thin layer as it becomes relativistically transparent, forming a standing wave which compresses and locks the electrons to the electric field node. (c) As the frequency of the standing wave decreases the field nodes move away from the mirror and the locked electrons are consequently pulled along, setting up an electrostatic field between them and protons of the thin layer. (d) The electrons are released as the pulse leaves the mirror and the standing wave disappears. The protons, having obtained a significant amount of energy, is travelling away from the mirror.

and recompressed using the chirped-pulse amplification technique. Physically, this introduces a frequency-dependent time delay that alters the relative phase between different frequencies. As an effect, the pulse becomes longer but, more importantly to us, it also obtains a time-variable frequency. To lowest order, this can be achieved by introducing a simple linear chirp, also known as group delay dispersion, in which the *instantaneous time delay* varies linearly with frequency. Since the instantaneous delay is simply the frequency derivative of the phase, $t_d(\omega) = \mathrm{d}\phi/\mathrm{d}\omega$, the linear chirp is introduced by an additional phase component ϕ, which will have to be quadratic in frequency. Assuming that we also wish to have no time delay of the central frequency we may choose

$$\phi(\omega) = \mathcal{C}(\omega - \omega_0)^2/4a, \tag{4.5}$$

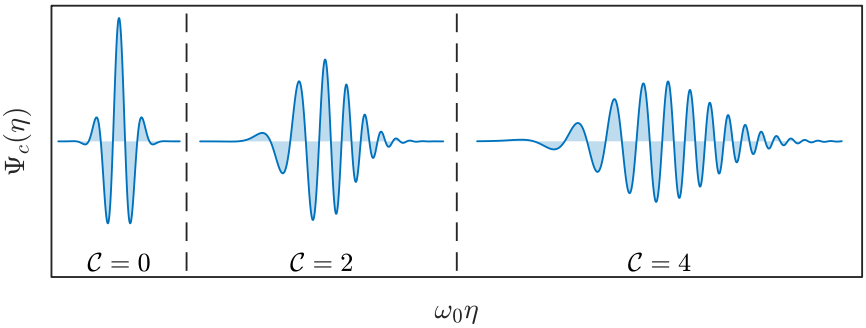

Figure 4.2: Waveform of a Gaussian pulse with bandwidth $\Delta\omega = 0.5\omega_0$, for three different values of the dimensionless chirp parameter $\mathcal{C}$, according to equation (4.7).

where $\mathcal{C}$ is a *dimensionless chirp parameter*. With this choice, the chirped pulse is simply described by

$$\hat{\Psi}_c(\omega) = \hat{\Psi}(\omega)\exp[-i\phi(\omega)] = \sqrt{\frac{\pi}{a}}\exp\left[-(1+i\mathcal{C})(\omega-\omega_0)^2/4a\right], \tag{4.6}$$

and after transforming it back to the time domain it can finally be expressed as

$$\Psi_c(\eta) = \psi_c\exp\left[-\alpha\eta^2 + i(\omega_0\eta + \kappa\eta^2 + \delta)\right], \tag{4.7}$$

where we have defined

$$\psi_c = \frac{1}{\sqrt[4]{1+\mathcal{C}^2}}, \quad \alpha = \frac{1}{1+\mathcal{C}^2}a, \quad \kappa = \frac{\mathcal{C}}{1+\mathcal{C}^2}a, \quad \delta = \frac{\omega_0^2}{4a}\mathcal{C} + \frac{\arctan\mathcal{C}}{2}. \tag{4.8}$$

After studying this expression it can be noted that the constant term in the phase, δ, could have been completely avoided through a different choice of $\phi(\omega)$ in equation (4.5). Furthermore, that the pulse is now linearly chirped can be inferred from the presence of the η^2-term in the phase of equation (4.7), as it allows us to write the instantaneous frequency as a linear function of η,

$$\omega(\eta) = \omega_0 + 2\kappa\eta. \tag{4.9}$$

Finally, the peak amplitude of the pulse is seen to decrease for increasing values of $|\mathcal{C}|$, while the pulse also becomes longer, as expected. The amount of stretching of the pulse is related to the dimensionless chirp parameter as

$$\tau_c/\tau_0 = \sqrt{1+\mathcal{C}^2}, \tag{4.10}$$

where τ_c is the FWHM duration of the chirped pulse. The waveform of an example pulse with bandwidth $\Delta\omega = 0.5\omega_0$ is visualized in Figure 4.2 for different values of chirp.

4.3 Chirped standing wave

By illuminating a dense plasma slab with a laser pulse described by equation (4.7), a chirped standing wave can be formed. For a pulse travelling in the positive x-direction, with the mirror located at $x = 0$, and assuming perfect reflection, this standing wave will (for $x \leq 0$) be described by two counter-propagating pulses of equal and opposite amplitude. We define $\eta_- = t - x/c$ and $\eta_+ = t + x/c$ for a pulse propagating in the positive and negative x-direction, respectively. By describing the pulse as the real part of equation (4.7) and assuming the intensity gradient to be small, $|\alpha(\eta_+^2 - \eta_-^2)| \ll 1$, the standing wave can be expressed as

$$\Psi_c^{\mathrm{SW}}(x,t) = \Psi_c(\eta_-) - \Psi_c(\eta_+) \approx -2\psi_c \exp(-\alpha\eta_-^2)\sin(A)\sin(B), \quad (4.11)$$

where we have defined

$$A(x,t) = \omega_0 t + \kappa(t^2 + x^2/c^2) + \delta, \quad B(x,t) = (\omega_0 + 2\kappa t)x/c. \quad (4.12)$$

Studying the case of zero chirp, for which $A(x,t) = \omega_0 t$ and $B(x,t) = \omega_0 x/c$, allows us to identify that the argument of the first sine defines the temporal oscillation and the argument of the second defines the node positions of the standing wave. The nodes of the chirped standing wave is therefore given by $B(x,t) = n\pi$, for some integer n, or

$$x = n\frac{\lambda_0}{2}\left(1 + \frac{2\kappa}{\omega_0}t\right)^{-1}, \quad (4.13)$$

where $\lambda_0 = 2\pi c/\omega_0$ is the laser central wavelength. At $t = 0$ the nodes can be seen to be located at half-wavelength steps from the mirror. For $x < 0$ and for the nodes to move *away* from the mirror we further note that a negative chirp is required, $\mathcal{C} < 0$, meaning that the frequency is decreasing (wavelength is increasing) with time. Furthermore, the speed of the node can be obtained through differentiation and shows that higher-order nodes (larger $|n|$) will move proportionally faster. It is however important to remember the approximation that $|\alpha(\eta_+^2 - \eta_-^2)| = |4\alpha t x/c| \ll 1$, which restricts the validity for the higher-order nodes. In reality such nodes will not be very stable due to beating oscillations.

4.4 Relativistic self-induced transparency

This far we have only considered the formation of the chirped standing wave. However, in order to accelerate ions using this field, we must also be able to place the ions and electrons in one of the nodes. This is achieved through an effect called *relativistic self-induced transparency* (RSIT) [103–114], by which a plasma becomes transparent to a sufficiently intense laser field. This

effect is simply a result of the limiting speed of light, as this also imposes a limit on the current that can be produced by a finite number of charges. For a plasma slab of areal density $\sigma = n_e L$, where L is the thickness of the slab, the maximum possible current is

$$j_{\max} = \sigma c e, \tag{4.14}$$

assuming that only electrons are contributing. Through Faraday's law (2.5d) we further obtain that there is a maximum field strength that this current can produce, which would be necessary in order for the plasma slab to reflect the incoming radiation. Assuming circular polarization we get that the threshold intensity that can be reflected by the plasma slab is

$$I_{\text{th}} = \pi c e^2 \sigma^2. \tag{4.15}$$

Further defining the *critical areal density* as $\sigma_{\text{cr}} = \lambda_0 n_{\text{cr}}$, the threshold intensity can be expressed as

$$\frac{I_{\text{th}}}{I_{\text{rel}}} = \pi^2 \left(\frac{\sigma}{\sigma_{\text{cr}}} \right)^2, \tag{4.16}$$

where I_{rel} corresponds to an a_0 of unity.

As we have shown, for a given areal density there is a threshold intensity above which the plasma slab becomes transparent. By placing an ultra-thin foil in front of a mirror we can therefore get the ions and electrons into the standing wave. When irradiated by the intense laser pulse, the thin foil will become relativistically transparent as the intensity surpasses the threshold. Assuming that the mirror is sufficiently dense, the standing wave will then quickly form as the pulse is reflected from the mirror. In order to optimize the acceleration distance of the ions we can therefore place the ultra-thin foil such that its position coincides with the initial position of one of the standing-wave nodes.

4.5 Ion acceleration

As the electrons are displaced by the movement of the electric field nodes of the standing wave, the resulting charge separation will give rise to a micron-sized capacitor-like longitudinal field. Since the maximum strength of this field is proportional to the areal charge density of the thin foil, we want this areal density to be as large as possible, while still allowing for relativistic transparency.

In Ref. [101], these two conditions are considered when estimating the maximum achievable energy of the ions. This is mainly done through an estimate of the total acceleration time of the ions. The study further demonstrates the tunability of the scheme through variation of the chirp, and shows

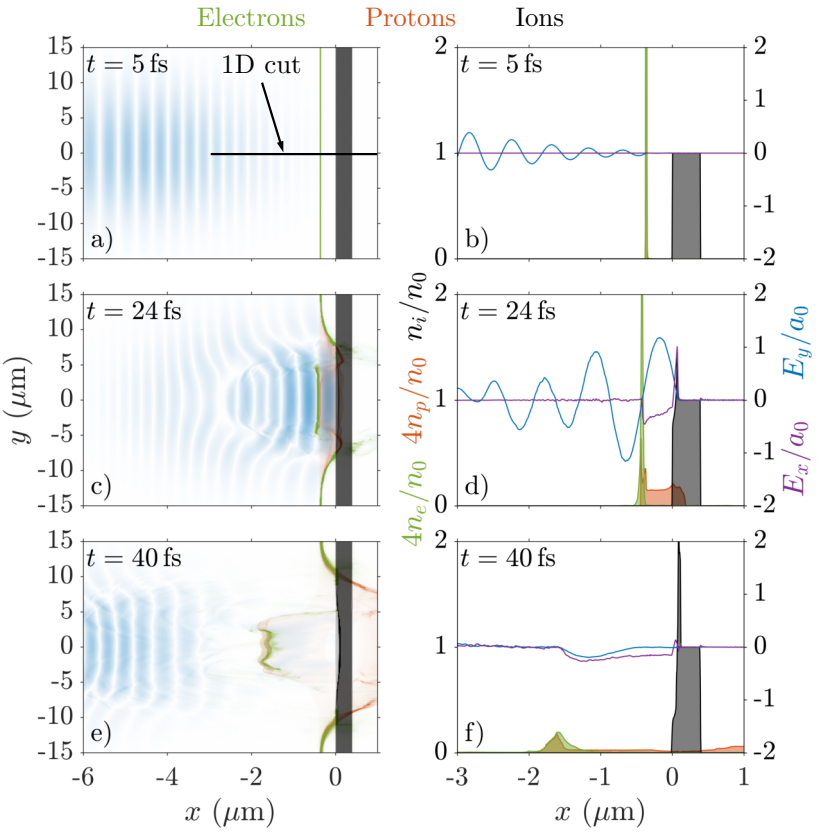

Figure 4.3: A 2D PIC simulation of CSWA for a laser energy $\varepsilon_0 = 80\,\mathrm{J}$, spot size $w = 10\,\mu\mathrm{m}$, bandwidth $\Delta\omega = 0.5\omega_0$ and chirp $\mathcal{C} = -4$ is shown for three time instants: (a, b) before the interaction between the laser pulse and the thin foil; (c, d) during the CSWA stage when the electrons are locked to the standing wave formed by the reflected radiation; (e, f) and some time after the pulse has been reflected and the electrons released. (a, c, e) Magnitude of the transverse electric field E_y (blue), electron density (green), proton density (red), and ion density (grey) as functions of 2D coordinates. (b, d, f) A 1D cut additionally showing the longitudinal electric field E_x (purple) and transverse electric field E_y (blue), with fields obtained for $y = 0$ and densities averaged over the range $|y| < w/2$.

that it is possible to accelerate protons in excess of 100 MeV. Even more importantly, the resulting ion beam is collimated, of high charge and displays a peaked energy spectrum. A typical 2D simulation of proton acceleration using CSWA can be seen in Figure 4.3.

In Paper B [102] we discuss *standing-wave acceleration* (SWA) from a more general perspective, not necessarily relying upon chirp to move the locked electrons. We also demonstrate that CSWA, as a particular implementation of SWA, performs well also under non-ideal conditions and is robust against the effects of limited contrast, misalignment and elliptical

polarization. Finally, we discuss the prospects and limitations of CSWA and show that its main limitation lies in the maximum acceleration distance of the ions, which is determined by the bandwidth of the laser pulse. In particular, we derive an estimate for the achievable proton energies based on this limitation, which scales as

$$E_D \approx 3.2 a_0 \left(\frac{n}{2} \frac{\Delta\omega}{\omega_0} \right) \text{[MeV]}, \tag{4.17}$$

showing the importance of not only the field amplitude, but the pulse bandwidth as well.

The outlined capabilities can be further improved through a number of more advanced modifications. So far, the frequency chirp has been assumed to be purely linear, ultimately yielding the node movement described by equation (4.13). By allowing for higher-order dispersive effects, the speed of the node can instead be tailored to the speed of the accelerated sheet of ions. Further improvements are also expected from the use of a flat-top pulse (after stretching), as it better utilizes the total pulse energy and improves the stability of the higher-order nodes. Using several pulses it may also be possible to implement a staging procedure, utilizing nodes of increasingly higher order.

Chapter 5

Introduction to radiation reaction

In the classical theory of electromagnetism radiation is synonymous with electromagnetic waves, and is generated by the acceleration of charged particles. At the same time, as became evident in the early 20th century, radiation can also be described in terms of particles, called photons, carrying a discrete amount of energy E, or quanta, that is related to its corresponding frequency as $E = \hbar\omega$, where ω is the (angular) frequency and $\hbar$ the reduced Planck's constant. In quantum theory, these seemingly conflicting descriptions are treated using a single framework, showing that both descriptions can be valid approximations. This concept is more formally known as the wave-particle duality. However, which of these descriptions is more accurate depends on the situation. In particular, when the wavelength of the radiation is much smaller than all other relevant length scales, the particle description is often justified. A more complete description of electromagnetic radiation, accounting also for relativistic effects, is obtained within the framework of quantum electrodynamics (QED), which is one of the most successful theories of modern physics to date.

In Chapter 2 we covered the basic equations governing the collective motion of charged particles and the evolution of the electromagnetic fields. Through the coupling between the fields ($\mathbf{E}$, $\mathbf{B}$) and the macroscopic current and charge densities ($\mathbf{J}$, ρ), this collective motion leads to the generation of *coherent* radiation. However, in order for the radiation to be coherent, the average distance between the radiating particles must be small compared to the wavelength of the emitted radiation. Thus, if the particle number density n is low or the wavelength of the emitted radiation λ is small the emitted radiation can no longer be treated as coming from collective motion, but from single particles. The radiation is then said to be *incoherent*. More formally, the radiation can be treated as coherent when $\lambda > l$ and incoherent

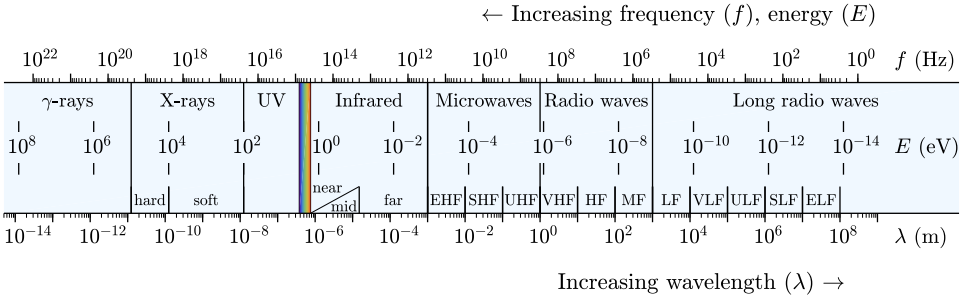

Figure 5.1: The spectrum of electromagnetic radiation and common classification of different spectral ranges. In the high-energy range of X-rays and γ-rays the radiation is primarily discussed in terms of its photon energy, while it in the low-energy range of microwaves and radio waves is mainly described by its frequency or wavelength, depending on field of study. In the intermediate range the radiation is mainly discussed in terms of wavelength and photon energy.

when $\lambda < l$, where $l = n^{-1/3}$ is the average distance between the radiating particles.

In Chapter 3 we covered the dynamics of single charged particles in strong fields, and saw that particles in such fields can experience very strong acceleration. We did not, however, discuss the incoherent radiation that this acceleration gives rise to, how the emission of radiation affects the particle emitting it or how it changes the equations of motion. This is what we aim to cover in this chapter. In Chapter 7 we will later show how the plasma dynamics and coherent radiation is modelled by the classical particle-in-cell scheme and how the incoherent radiation can be accounted for through extensions of the classical scheme.

5.1 Electromagnetic radiation

Electromagnetic radiation is all around us and is classically described as waves, made up by the oscillations of the electromagnetic fields, covering a broad range of frequencies, as presented in Figure 5.1. This radiation is often ascribed various properties which varies with its frequency, mainly depending on how it interacts with various forms of matter. The understanding of this interaction has paved the way for numerous groundbreaking scientific discoveries and is the foundation for countless technological applications. Furthermore, this has provided both tools for and helped advance many other fields of science, such as biology, medicine, astronomy and materials science.

In order to exploit electromagnetic radiation for various applications, one must also have a clear understanding of how it can be generated and the effects of this generation. As mentioned earlier, we will here cover radiation emitted from the acceleration of single particles. Of particular interest

are the total radiation emitted, the angular distribution of radiation, and its frequency spectrum. We will however focus our attention on the total radiation and its frequency spectrum, in order to keep the discussion more brief. Since we are mainly interested in radiation generation in relation to the dynamics of ultra-relativistic particles, this restriction will however be of little importance, for reasons that will be explained later. See Ref. [37, 46] for a more detailed discussion.

An expression for the total radiated power was derived over a century ago, in the case of a non-relativistic charged particle, showing that the radiated power is proportional to the square of the particle's acceleration. This is the so called Larmor result or, more commonly, *Larmor's formula* [115]

$$P = \frac{2}{3}\frac{e^2}{c^3}|\dot{\mathbf{v}}|^2, \tag{5.1}$$

where $\mathbf{v}$ and $\dot{\mathbf{v}}$ are the velocity and acceleration of the particle, respectively, and P is the total radiated power. Using the fact that the total power is Lorentz invariant, one can show that there is a unique relativistic generalization of the Larmor formula that reproduces equation (5.1) in the limit of non-relativistic motion [37]. It can be written

$$P = -\frac{2}{3}\frac{e^2}{m^2c^3}\left(\frac{\mathrm{d}p_\mu}{\mathrm{d}\tau}\frac{\mathrm{d}p^\mu}{\mathrm{d}\tau}\right), \tag{5.2}$$

where $p^\mu = \gamma m(c, \mathbf{v})$ is the particle's four-momentum, τ its proper time and the sign depends on the choice of metric.

The Larmor formula and its relativistic generalization can be derived through integration of the Poynting vector of the radiation fields over an infinite sphere enclosing the radiating particle. These fields are fully described by the motion of the particle, through the *Liénard–Wiechert potentials* [116, 117]. These potentials are a direct result of Maxwell's equations (2.5a) - (2.5d) and describe the time-varying electromagnetic fields for arbitrary motion of the particle,

$$\mathbf{E}(\mathbf{x}, t) = \frac{e}{c}\left[\frac{\mathbf{n}\times((\mathbf{n}-\boldsymbol{\beta})\times\dot{\boldsymbol{\beta}})}{(1-\boldsymbol{\beta}\cdot\mathbf{n})^3 R}\right]_{\tau_r}, \quad \mathbf{B} = [\mathbf{n}\times\mathbf{E}]_{\tau_r}, \tag{5.3}$$

where $\mathbf{n} = \mathbf{R}/R$ is a unit vector in the direction of the observation point $\mathbf{x}$ from the particle's position $\mathbf{r}(\tau)$, $\mathbf{R} = \mathbf{x} - \mathbf{r}(\tau)$, $\boldsymbol{\beta} = \mathbf{v}/c$ and the subscript τ_r means that the quantity inside the square brackets is to be evaluated at the retarded time τ_r, implicitly defined by $\tau_r = \tau - R(\tau_r)/c$.

The fields presented in equation (5.3) is formally only one part of the full expression, which consists of two terms commonly referred to as the velocity fields and acceleration fields. The foremost is equivalent to a boosted Coulomb field that depends on $\boldsymbol{\beta}$ alone, whereas the latter (shown in eq. 5.3)

is also proportional to the acceleration $\dot{\boldsymbol{\beta}}$, hence their names. However, because the velocity fields fall off as R^{-2}, compared to the R^{-1} dependence of acceleration field, they do not contribute to the radiated power (at infinity) and has therefore been dropped for brevity.

Further assuming that the observation point, $\mathbf{x}$, is far from the region of space where the acceleration occurs, and through Fourier transformation of equation (5.3), the total energy radiated per unit solid angle and unit frequency interval can be obtained as [37]

$$\frac{\mathrm{d}^2\mathcal{E}}{\mathrm{d}\omega\mathrm{d}\Omega} = \frac{e^2}{4\pi^2 c}\left|\int_{-\infty}^{\infty} \frac{\mathbf{n}\times((\mathbf{n}-\boldsymbol{\beta})\times\dot{\boldsymbol{\beta}})}{(1-\boldsymbol{\beta}\cdot\mathbf{n})^2}\mathrm{e}^{i\omega(t-\mathbf{n}\cdot\mathbf{r}(t)/c)}\,\mathrm{d}t\right|^2 . \tag{5.4}$$

While the radiated energy for arbitrary particle motion can be obtained from equation (5.4), for most practical purposes this expression becomes too expensive to work with. Fortunately, a number of important simplifications can be made when looking at ultra relativistic particles. First, it can be noted that in the relativistic limit, the radiation due to longitudinal acceleration is negligible compared to that of transverse acceleration [37]. More accurately, the radiated power due to a parallel force is a factor of γ^{-2} smaller than that due to a perpendicular force of equal magnitude. This is in fact a general result of special relativity [118], wherein a perpendicular force in general gives rise to an acceleration that is γ^2 larger than that from a parallel force. Secondly, in the relativistic limit ($\beta \to 1$) the factors of $(1-\boldsymbol{\beta}\cdot\mathbf{n})$ in the denominator of equations (5.3) - (5.4) dominates the angular distribution of the emitted radiation. As a result, the radiation is mainly emitted in a narrow cone along the direction of propagation and it can be shown that the root mean square angle of emission is γ^{-1} in this limit [37]. For most purposes it is thus sufficient to consider the radiation to be emitted exclusively in the particle's direction of propagation, as it undergoes an instantaneous circular motion.

5.1.1 Synchrotron radiation

Synchrotron radiation gets its name from the device with which it was first observed [119] and is the result of the transverse acceleration ($\dot{\mathbf{v}} \perp \mathbf{v}$) of ultra-relativistic charged particles as they undergoing circular motion in a strong magnetic field. This radiation is typically broadband, extending from microwaves all the way up to hard X-rays. In more elaborate setups, using e.g. undulators, the typical continuous spectrum can be turned into a series of harmonic peaks, through coherent superposition of contributions from different parts of the particle's trajectory. The exact form of the synchrotron spectrum (including that of e.g. undulators) can be derived from equation (5.4). We will here cover some of the main results.

Consider an electron moving around a circle of radius ρ and with velocity v, giving it an orbit angular frequency v/ρ. For non-relativistic motion

the radiation emitted is called *cyclotron radiation* and has a fundamental frequency equal to the orbit frequency. If we also consider the orbital motion as being caused by an external and perpendicular magnetic field, H, the orbital frequency becomes $\omega_{\mathrm{H}} = v/\rho = eH/\gamma mc$, called the *cyclotron frequency*. As the motion becomes relativistic however, the orbital frequency gets reduced by the factor of γ, while the typical frequency of the emitted radiation, or *characteristic synchrotron frequency*, scales as [37, 46]

$$\omega_c = \frac{3}{2}\omega_H \gamma^3 = \frac{3}{2}\frac{eH}{mc}\gamma^2, \tag{5.5}$$

where the numerical factor 3/2 is a matter of convention, chosen to simplify later expressions. Note especially that the typical frequency of the radiation gets strongly up-shifted due to relativistic effects.

As previously mentioned, the frequency spectrum of the synchrotron radiation can be obtained from equation (5.4). Assuming instantaneous circular motion as above and integrating over all angles of emission, the spectral intensity, defined as the radiated energy per unit frequency and unit time, is obtained to be

$$\frac{\mathrm{d}P}{\mathrm{d}\omega} = \frac{\sqrt{3}}{2\pi}\frac{e^3 H}{mc^2} F_1\left(\frac{\omega}{\omega_c}\right), \quad F_1(\xi) = \xi \int_\xi^\infty K_{5/3}(\xi')\mathrm{d}\xi', \tag{5.6}$$

where $F_1(\xi)$ is called the *first synchrotron function* and $K_{5/3}(\xi)$ is the modified Bessel function of the second kind, and is shown in Figure 5.2. Integrating equation (5.6) over all frequencies then gives us the total radiated power

$$P = \frac{4}{9}\frac{e^3 H}{mc^2}\omega_c = \frac{2}{3}\frac{e^4 H^2}{m^2 c^3}\gamma^2, \tag{5.7}$$

showing that it scales strongly with both magnetic field strength and electron energy (γ). By using the limiting forms of the modified Bessel function [120] the synchrotron spectrum of equation (5.6) can be obtained exactly in the limits of $\omega \ll \omega_c$ and $\omega \gg \omega_c$ as

$$\frac{\mathrm{d}P}{\mathrm{d}\omega} = \frac{e^3 H}{mc^2}\begin{cases} \frac{2^{2/3}}{\Gamma(\frac{1}{3})}\sqrt[3]{\frac{\omega}{\omega_c}} & \approx 0.59\sqrt[3]{\frac{\omega}{\omega_c}} & \text{if } \omega \ll \omega_c \\ \frac{\sqrt{3}}{2\sqrt{2\pi}}\sqrt{\frac{\omega}{\omega_c}}\mathrm{e}^{-\omega/\omega_c} & \approx 0.35\sqrt{\frac{\omega}{\omega_c}}\mathrm{e}^{-\omega/\omega_c} & \text{if } \omega \gg \omega_c \end{cases}, \tag{5.8}$$

where $\Gamma(z)$ is the gamma function. It is thus clear that the spectral intensity drops of rapidly for frequencies above ω_c, but extends far into the low frequency range due to the weak scaling below ω_c. The peak of the spectrum occur slightly below the critical frequency, at $\omega/\omega_c \approx 2/7$ (relative error of 0.034%).

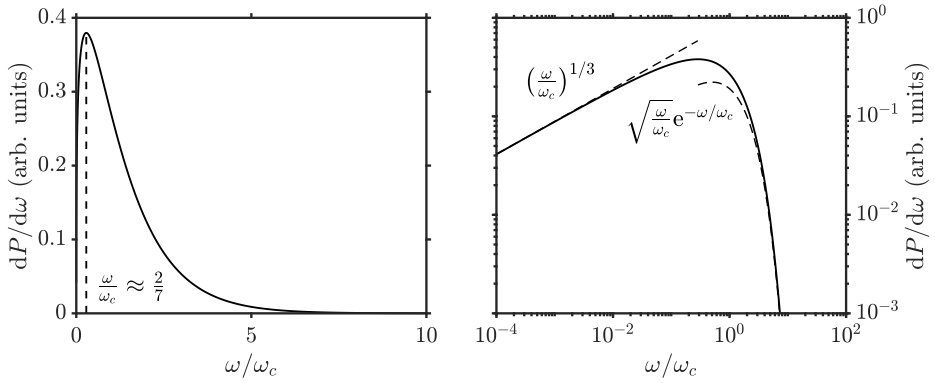

Figure 5.2: The spectral intensity of synchrotron radiation with a typical frequency ω_c. The dashed lines indicate the spectral maximum (left) and the asymptotic limits of the spectrum (right).

5.2 Classical radiation reaction

In the previous section we covered the radiation emission of accelerated charges moving along prescribed trajectories. Through simple arguments of conservation of energy and momentum this emission must invariably lead to a recoil of the particle, such that it loses energy (and momentum) equivalent to that carried away by the radiation fields. In order to account for this *radiation reaction* (RR) the equations of motion of the particle must be amended, as this recoil is not captured by the Lorentz force (eq. 2.6).

To illustrate that the recoil is not captured by the Lorentz force, we again turn to the simple example of a relativistic, charged particle moving in a constant magnetic field H, perpendicular to the velocity of the particle. In this field, according to the Lorentz equation, the particle will move indefinitely along a circle of radius $\rho = \gamma mcv/eH$, as the magnetic field bends its trajectory without performing any work on the particle (leaving v and γ constant). However, as we saw in the previous section, the particle should continuously lose energy equivalent to what is radiated away according to equation (5.7). As a result, the particle should instead spiral inwards, as both γ and v decreases over time ($\mathrm{d}\gamma/\mathrm{d}t = -P/mc^2$).

In order to account for radiation reaction, the equations of motion are typically modified to include an extra force term

$$m\dot{\mathbf{v}} = \mathbf{F}_{\mathrm{EM}} + \mathbf{F}_{\mathrm{RR}}, \tag{5.9}$$

where $\mathbf{F}_{\mathrm{EM}}$ is the Lorentz force as in equation (2.6). By requiring that the average work done on the particle should equal the energy loss through Larmor's formula (eq. 5.1) the radiation reaction force is found to be

$$\mathbf{F}_{\mathrm{RR}} = \frac{2}{3}\frac{e^2}{c^3}\ddot{\mathbf{v}} = m\tau_{\mathrm{LAD}}\ddot{\mathbf{v}}. \tag{5.10}$$

This force is also called the *Abraham-Lorentz* force and has a typical time scale associated with it, $\tau_{\mathrm{LAD}} = 2e^2/3mc^3 = 2.27 \times 10^{-24}\,\mathrm{s}$. The relativistic generalization of (5.9)-(5.10) is given by the *Lorentz-Abraham-Dirac* (LAD) equation [121–123]

$$\frac{\mathrm{d}p^\mu}{\mathrm{d}\tau} = \frac{eF^{\mu\nu}p_\nu}{mc} + f^\mu_{\mathrm{RR}}, \quad f^\mu_{\mathrm{RR}} = \frac{2}{3}\frac{e^2}{mc^3}\left[\frac{\mathrm{d}^2p^\mu}{\mathrm{d}\tau^2} + \frac{p^\mu}{m^2c^2}\left(\frac{\mathrm{d}p^\nu}{\mathrm{d}\tau}\frac{\mathrm{d}p_\nu}{\mathrm{d}\tau}\right)\right], \quad (5.11)$$

where f^μ_{RR} is the radiation reaction four-force. However, as both of these forms contain a third order time derivative, they admit pathological solutions exhibiting runaway acceleration or acausal behaviour [124].

This situation can be overcome by considering the radiation reaction force to be but a smaller perturbation to the equation of motion, such that $|\mathbf{F}_{\mathrm{RR}}| \ll |\mathbf{F}_{\mathrm{EM}}|$. In such a case, a reduction of order can be achieved by expressing the higher order derivatives in terms of the external field, $\mathrm{d}p^\mu/\mathrm{d}\tau \approx eF^{\mu\nu}p_\nu/mc$, giving us the *Landau-Lifshitz* (LL) form of radiation reaction [46]

$$f^\mu_{\mathrm{RR}} = \frac{2}{3}er_e\left(\partial_\lambda F^{\mu\nu}\right)u_\nu u^\lambda + \frac{2}{3}r_e^2\left[F^{\mu\nu}F_{\nu\lambda}u^\lambda + (F^{\nu\kappa}u_\kappa)(F_{\nu\lambda}u^\lambda)u^\mu\right], \quad (5.12)$$

where $u^\mu = p^\mu/mc$ is the particle four-velocity normalized to the speed of light and $r_e = e^2/mc^2$ is the classical electron radius.

While the LL equations of motion provides a description of radiation reaction that is free from the issues plaguing the LAD equation, its validity depends on the relative strength of the RR term and is therefore not generally applicable. However, looking more closely at the typical time scale involved in the LAD equation we find that it is close to three orders of magnitude shorter than the quantum mechanical time scale of electrons, the Compton time $\tau_C = \hbar/mc^2 = 1.29 \times 10^{-21}\,\mathrm{s}$. This strongly suggests that the problem is in fact quantum mechanical in nature and that it in light of this perhaps should not be surprising that a fully consistent classical description seemingly can not be found.

5.3 Quantum radiation reaction

In order to resolve questions on radiation reaction, we must turn to the quantum mechanical description of nature. Within the theory of quantum electrodynamics, the interaction between charged particles and electromagnetic fields is mediated by photons that effectively makes up the fields. In this interaction, photons and particles can scatter on each other and thereby exchange both energy and momentum. The theory also enables the creation and annihilation of particle-antiparticle pairs, as a consequence of special relativity and quantum mechanics. In contrast to classical electrodynamics

this interaction is inherently stochastic and the probability of a particular outcome is given by the corresponding *probability amplitude*. QED is a perturbation theory, in which the probabilities are computed through an expansion in the fine structure constant $\alpha = e^2/\hbar c \approx 1/137$. The different terms in this expansion are often computed using the pictorial representation developed by Feynman, called Feynman diagrams.

Using this approach, the probability of scattering electrons (and positrons) on a single photon (or even a few) can be calculated to incredible precision. However, in the strong laser fields considered in this thesis, the number of photons each electron interacts with is large. To illustrate this, we can consider the relativistic field amplitude $a_0 \gg 1$. It can be re-expressed as $eE\lambda_C \gg \hbar\omega$, where $\lambda_C = \hbar/mc$ is the reduced *Compton wavelength* that in turn expresses a fundamental limit on measuring the position of a particle. This inequality shows that the work performed by the laser field over the distance of one Compton length ($eE\lambda_C$) is much greater than the energy of a single photon in the laser field ($\hbar\omega$) for large a_0.

In the perturbative expansion of QED, its terms are actually not independent of the field strength a_0. For the relativistic field amplitudes achievable with high-intensity lasers ($a_0 > 1$), higher order terms can in fact be enhanced by a factor of a_0 (or larger), such that the naïve expansion is no longer guaranteed to converge. The study of QED at relativistic field strengths therefore requires different tools than usual in order to circumvent such concerns and is sometimes considered an area of its own, called *strong-field QED* (SFQED). In this area, the laser field is instead often treated as a fixed background, making up a coherent photon state with which particles can interact. This is called the *Furry picture* and is widely employed together with *Volkov states* [125], exact (non-perturbative) solutions of the Dirac equation in the presence of a plane-wave field, in order to describe many SFQED processes. These processes can be represented by its corresponding Feynman diagrams as before but where the particles are now described by "dressed" particle states, accounting for the interaction with the photons of the background field. In general however, the problem is very complicated and solutions have therefore only been obtained for a few special, often highly symmetric, cases such as for a constant or plane wave field.

Nevertheless, a number of important results have been obtained. Of particular importance for this thesis, the rates of a number of quantum processes has been computed, albeit given a number of assumptions and approximations, and has subsequently been implemented in several state-of-the-art codes in order to utilize this theory for more practical purposes. This provides a coupling between plasma physics, lasers physics and QED, giving rise to a zoo of complex dynamics and interesting phenomena, some of which will be discussed in Chapter 6.

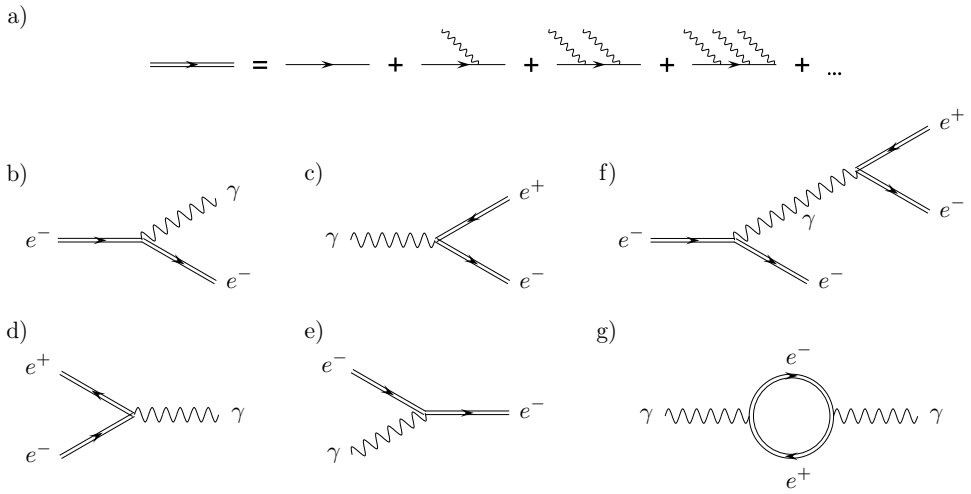

Figure 5.3: Feynman diagrams for some common strong-field QED processes. In these diagrams the particles are described by "dressed" particle states (a), represented by double lines, which accounts for the interaction with the photons of the background field. The lowest order processes are (b) single photon emission, (c) pair production, (d) annihilation and (e) photon absorption. Higher order processes, such as (f) trident and (g) vacuum birefringence, are also possible.

5.3.1 The Schwinger effect

One of the earliest results belonging to SFQED is the possibility of producing electron-positron pairs from vacuum, without any presence of massive seed particles. This is made possible by the instability of the quantum vacuum under the influence of a strong, external electric field, from which virtual electron-positron pairs can gain sufficient energy to be physically created ($2mc^2$).

This nonperturbative pair production is strongly suppressed for field strengths below a critical field $E_\mathrm{S} = mc^2/e\lambda\!\!\!^{-}_C = m^2c^3/e\hbar \simeq 10^{18}\,\mathrm{V/m}$, called the *Sauter-Schwinger field* [126–128], defined as the electric field that produces work equal to mc^2 over the distance of a Compton length. For a constant electric field E the electron-positron pair creation rate R_S (i.e., the number of pairs per unit time and unit volume) due to this effect is given by [128–130]

$$R_\mathrm{S} = \frac{1}{4\pi^3 \lambda\!\!\!^{-3}_C \tau_C} \frac{E^2}{E_\mathrm{S}^2} \exp\Big(-\frac{\pi E_\mathrm{S}}{E}\Big). \tag{5.13}$$

Expressed in terms of numbers more familiar to laser physicists, the Schwinger limit corresponds to an intensity of $\approx 10^{29}\,\mathrm{W/cm^2}$ (assuming optical wavelengths), and is therefore considered to be well beyond current capabilities.

5.3.2 Nonlinear Compton scattering

While the Schwinger limit is currently out of reach, quantum effects still play a significant role well below this limit [131]. Turning our attention back to the classical result of synchrotron radiation we see that when $\hbar\omega_c/\gamma mc^2 \sim 1$, equation (5.6) predicts the emission of photons with energies above the energy of the electron. Such emissions can of course not be physical, and the synchrotron spectrum must therefore be amended in this regime. Furthermore, if a single photon is able to carry off a significant portion of the emitting particle's energy and momentum the emission and subsequent reaction can no longer be treated classically, as if it was the result of continuous emissions. These effects are parametrised by the *quantum nonlinearity parameter*

$$\chi \equiv \frac{\sqrt{|F_{\mu\nu}p^\nu|^2}}{mcE_\mathrm{S}} = \gamma\frac{1}{E_\mathrm{S}}\sqrt{\left(\mathbf{E}+\frac{\mathbf{v}}{c}\times\mathbf{B}\right)^2-(\frac{\mathbf{v}}{c}\cdot\mathbf{E})^2}, \tag{5.14}$$

which describes the field strength felt in the rest frame of the particle, relative to the Sauter-Schwinger field. The square root expression can also be thought of as being the result of an *effective*, transverse magnetic field H_eff, allowing us to also write the quantum nonlinearity parameter as

$$\chi = \gamma\frac{H_\mathrm{eff}}{E_\mathrm{S}}. \tag{5.15}$$

Through equation (5.5) we thus have that χ can be further viewed as the ratio of the typical energy of the emitted photon, to the energy of the electron

$$\chi = \frac{2}{3}\frac{\hbar\omega_c}{\gamma mc^2}. \tag{5.16}$$

Moreover, equation (5.14) allows us to rewrite the generalized Larmor's formula (eq. 5.2) in a more accessible form

$$P = -\frac{2}{3}\frac{e^2}{m^2c^3}\left(\frac{\mathrm{d}p_\mu}{\mathrm{d}\tau}\frac{\mathrm{d}p^\mu}{\mathrm{d}\tau}\right) = \left\{\frac{\mathrm{d}p^\mu}{\mathrm{d}\tau} = \frac{eF^{\mu\nu}p_\nu}{mc}\right\} = \frac{2}{3}\frac{\alpha mc^2}{\tau_C}\chi^2, \tag{5.17}$$

making the well known χ^2 scaling explicit.

In light of equation (5.16), the results of Section 5.1.1 can only be valid in the classical limit $\chi \ll 1$. In the quantum regime, defined by $\chi \gtrsim 1$, the spectrum given by equation (5.7) must be corrected, such as to account for the finite energy of the radiating particle. This correction can to first order be obtained from the emission rates of nonlinear Compton scattering (Fig. 5.3b), which have been computed in SFQED assuming incoherent single-particle emissions from the interaction with a constant plane-wave field. This assumption is often called the *locally constant crossed field approximation* (LCFA), and formally assumes that the two field invariants $\mathbf{E}^2-\mathbf{B}^2$ and $\mathbf{E}\cdot\mathbf{B}$ are identically zero (or at least negligible).

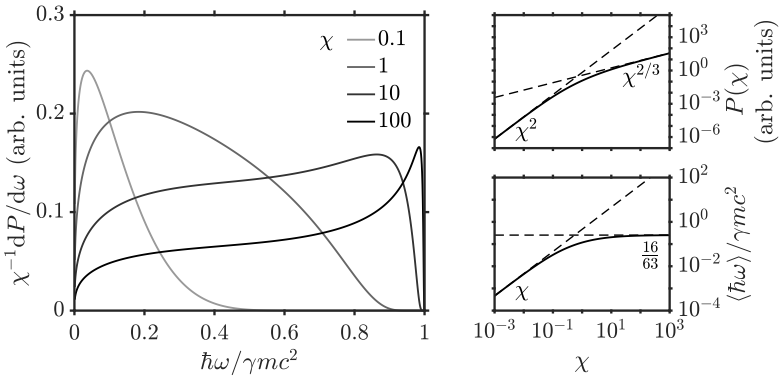

Figure 5.4: The spectral intensity of nonlinear Compton scattering (left) for different values of the nonlinear quantum parameter χ. The total power (top right) and average photon energy (bottom right) of emitted radiation is also shown, together with its asymptotic scalings (dashed lines).

The photon emission rate due to nonlinear Compton scattering is often expressed in terms of the photon number spectrum per unit time, and has been obtained to be [132, 133]

$$\frac{\mathrm{d}N}{\mathrm{d}\delta} = \frac{\sqrt{3}}{2\pi}\frac{\alpha}{\tau_C}\frac{\chi}{\gamma}\left[\frac{(1-\delta)}{\delta}F_1(z) + \delta F_2(z)\right], \quad z = \frac{2}{3\chi}\frac{\delta}{1-\delta}, \tag{5.18}$$

where $\delta = \hbar\omega/\gamma mc^2$ is the photon energy normalized to the energy of the radiating particle and $F_2(x) = xK_{2/3}(x)$ is the *second synchrotron function*. Interestingly, this result can also be obtained through a simpler analysis, taking into account kinematics and particle spin [134]. This quantum corrected spectrum can now be compared to the classical spectrum by means of the spectral intensity $\mathrm{d}P/\mathrm{d}\delta = (\hbar\omega)\mathrm{d}N/\mathrm{d}\delta$,

$$\frac{\mathrm{d}P}{\mathrm{d}\delta} = \frac{\sqrt{3}}{2\pi}\frac{\alpha mc^2}{\tau_C}\chi\left[(1-\delta)F_1(z) + \delta^2 F_2(z)\right], \quad z = \frac{2}{3\chi}\frac{\delta}{1-\delta}, \tag{5.19}$$

which can also be written as

$$\frac{\mathrm{d}P}{\mathrm{d}\omega} = \frac{\sqrt{3}}{2\pi}\frac{e^3 H_{\mathrm{eff}}}{mc^2}(1-\delta)\left[F_1(z) + \frac{3\chi}{2}\delta z F_2(z)\right], \quad z = \frac{2}{3\chi}\frac{\delta}{1-\delta}. \tag{5.20}$$

From the properties of the synchrotron functions it can now be seen that the classical result (5.6) can be recovered in the classical limit $\chi \to 0$.

The spectral intensity (5.19) is presented in Figure 5.4 and clearly shows the distortion of the spectrum for larger values of χ, wherein the spectral peak narrows as it is pushed closer to $\delta = 1$. The modification of the spectrum also affects various scaling laws, and it can therefore be of interest to integrate both the number spectrum (5.19) and the spectral intensity (5.19) over all photon energies to obtain the total number of emitted photons

per unit time and the total emitted power, respectively. These integrals can be performed analytically in the classical $\chi \ll 1$ and quantum $\chi \gg 1$ limits, giving the number of photons per unit time

$$N = \frac{\alpha}{\tau_C}\frac{1}{\gamma}\begin{cases} \frac{5}{2\sqrt{3}}\chi & \approx 1.44\chi & \text{if } \chi \ll 1 \\ \frac{14\Gamma(\frac{2}{3})}{9\sqrt[3]{3}}\chi^{2/3} & \approx 1.46\chi^{2/3} & \text{if } \chi \gg 1 \end{cases}, \tag{5.21}$$

and total power

$$P = \frac{\alpha mc^2}{\tau_C}\begin{cases} \frac{2}{3}\chi^2 & \approx 0.67\chi^2 & \text{if } \chi \ll 1 \\ \frac{32\Gamma(\frac{2}{3})}{81\sqrt[3]{3}}\chi^{2/3} & \approx 0.37\chi^{2/3} & \text{if } \chi \gg 1 \end{cases}. \tag{5.22}$$

In particular, the scaling for the total emitted power is reduced for large χ, which in turn results in an overestimation of e.g. radiation reaction as described by the Landau-Lifshitz equations of motion (5.12). The total power is therefore often written as $P = (2\alpha/3\tau_C)mc^2 g(\chi)\chi^2$, where $g(\chi)$, called the Gaunt factor, provides the correction to the classical scaling. This discrepancy is sometimes corrected for in the LL equation by similarly rescaling the radiation reaction term by $g(\chi)$. While it is an improvement, this approach would then still treat emissions classically and therefore fails to correctly capture other parts of the physics, such as stochasticity effects. A more accurate description that makes direct use of the emission rates is discussed in Chapter 7.

Finally, we may combine the computed scalings to obtain the average energy of the emitted photons in the two limits

$$\langle \hbar\omega \rangle = P/N = \gamma mc^2 \begin{cases} \frac{4}{5\sqrt{3}}\chi & \approx 0.46\chi & \text{if } \chi \ll 1 \\ \frac{16}{63} & \approx 0.254 & \text{if } \chi \gg 1 \end{cases}. \tag{5.23}$$

Here it is interesting to note that the average photon energy, to first order, approaches a constant value of $\hbar\omega \approx \gamma mc^2/4$ in the limit of large χ, which is also shown in Figure 5.4.

5.3.3 Multi-photon Breit-Wheeler

Similarly to how electrons and positrons emit photons through nonlinear Compton scattering as they interact with a strong laser-field, high-energy photons can themselves interact with the field and decay into an electron-positron pair through the process of multi-photon Breit-Wheeler (Fig. 5.3c). This is parametrized by the photon quantum nonlinearity parameter χ_γ defined as

$$\chi_\gamma \equiv \frac{\sqrt{|F_{\mu\nu}\hbar k^\nu|^2}}{mcE_S}, \tag{5.24}$$

where $k^\nu = (\omega/c, \mathbf{k})$ is the photon four-wavevector.

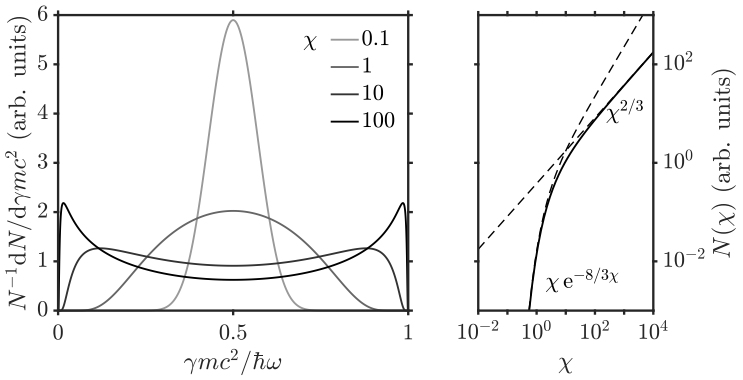

Figure 5.5: The energy spectrum of multi-photon Breit-Wheeler pair production (left) for different values of the nonlinear quantum parameter χ_γ. The total number of produced pairs (right) is also shown, together with its asymptotic scalings (dashed lines).

The pair production rate due to multi-photon Breit-Wheeler has been obtained similarly to nonlinear Compton scattering. The number spectrum of produced pairs per unit time is [132, 133, 135]

$$\frac{\mathrm{d}N}{\mathrm{d}\delta_e} = \frac{\sqrt{3}}{2\pi}\frac{\alpha}{\tau_C}\frac{mc^2\chi_\gamma}{\hbar\omega}\left[(\delta_e-1)\delta_e F_1(z) + F_2(z)\right], \quad z = \frac{2}{3\chi_\gamma}\frac{1}{(1-\delta_e)\delta_e}, \tag{5.25}$$

where $\delta_e = \gamma mc^2/\hbar\omega$ is the electron energy (and $1-\delta_e$ the positron energy) normalized to the energy of the photon. This strongly resembles equation (5.18) as a result of the crossing symmetry between their respective Feynman diagrams. The pair production spectrum is presented in Figure 5.5 for different values of χ_γ. Unlike the photon emission spectrum, however, the pair production spectrum is clearly symmetric around $\delta_e = 0.5$ and has a Gaussian shape for small χ_γ. At the other end of the scale, the spectrum is symmetrically split into two peaks, pushed towards $\delta_e = 0$ and $\delta_e = 1$.

Also often of interest is the total pair production. In the limits of $\chi_\gamma \ll 1$ and $\chi_\gamma \gg 1$, the total number of produced pairs per unit time can be obtained analytically as

$$N = \frac{\alpha}{\tau_C}\frac{mc^2}{\hbar\omega}\begin{cases} \frac{3\sqrt{3}}{16\sqrt{2}}\chi_\gamma \mathrm{e}^{-8/3\chi_\gamma} & \approx \quad 0.23\chi_\gamma \mathrm{e}^{-8/3\chi_\gamma} & \text{if } \chi_\gamma \ll 1 \\ \frac{20\pi^2}{7\sqrt[3]{3}\Gamma(\frac{1}{3})^4}\chi_\gamma^{2/3} & \approx \quad 0.38\chi_\gamma^{2/3} & \text{if } \chi_\gamma \gg 1 \end{cases}, \tag{5.26}$$

and is presented in Figure 5.5. Of particular interest is the fact that the total pair production rate is strongly suppressed in the limit of small χ_γ, similarly to the Schwinger pair production rate (5.13). In the high-χ_γ limit the rate instead scales as $\chi_\gamma^{2/3}$, which is the same as the high-χ scaling of the photon emission rate (5.21) discussed earlier.

Chapter 6

Radiation generation

Contemporary sources of extreme light are commonly based on one of two major principles, bremsstrahlung and Compton (back)scattering. In the former, photon emission is triggered as a charged particle interacts with the Coulomb field of a heavy particle, or even the combined field of several heavy particles in for example a crystal lattice. With Compton scattering, which will be the focus of this chapter, the photon emission instead comes from the interaction of an electron with one or several photons, typically in the form of a laser field. While synchrotron sources deserves to be mentioned, arguably being the most common light source, we make no distinction between synchrotron radiation and Compton scattering in this thesis, along the lines of Chapter 5.

The primary focus of this chapter is on the generation of high-energy photons, as studied in Paper C [136], but results of Paper D [137] will also be briefly discussed. Before proceeding further, we first define what we mean with *high-energy* photons. In essence, the expression will be used as a relative measure of the photon energy $\hbar\omega$ compared to the energy of the radiating particle $\varepsilon_0 = \gamma mc^2$, hereafter assumed to be an electron. Borrowing the stricter definition used in Paper C, we will consider photons with an energy above half the electron energy ($\hbar\omega > \varepsilon_0/2$) to be of high energy. While this formally permits photons of any energy, our main interest is on the generation of photons with an absolute energy of 1 GeV and above, and the discussions will be restricted accordingly. In Chapter 5 the average photon energy was shown to scale as $\langle\hbar\omega\rangle \sim \gamma mc^2\chi$, before saturating to a constant fraction of the electron energy at large values of χ. Maximizing the typical photon energy, for any given electron energy, is therefore a matter of maximizing the nonlinear quantum parameter χ, defined in (5.14), which means aiming for the quantum regime of radiation reaction. Naturally, this can be done by turning up either the field strength or the particle momentum.

One of the simplest setups, conceptually, for reaching the quantum regime of radiation reaction is to collide an energetic electron beam with

a high-intensity laser field. Assuming linear polarization and that the particle propagates at an angle of θ to the propagation direction of the laser field the nonlinear quantum parameter becomes

$$\chi = \gamma \frac{a_0}{a_S}(1 - \beta \cos\theta), \tag{6.1}$$

where $a_S = eE_S/m\omega c = \lambda/\lambda_C = 4.12 \times 10^5$ is the normalized Schwinger field at a wavelength of 1 µm and $\beta = v/c$ is the speed of the electron normalized to the speed of light. Unsurprisingly, χ is maximized at an optimal angle of $\theta = \pi$, corresponding to the case of antiparallel propagation. This is also the setup used in both previous and contemporary experiments, aimed at studying the quantum regime of radiation reaction. Most famous being the famous SLAC E-144 [138, 139], and the more recent experiments at the Central Laser Facility, Rutherford Appleton Laboratory [140, 141].

While the preceding discussion suggests that a high χ can be reached given a sufficiently large peak intensity, for pulses of long temporal duration, or with otherwise fat-tailed distributions, the energy losses during the interaction in the tail can be significant. Reaching large values of χ is therefore not simply a matter of peak intensity, but spatial and temporal extent as well. Taking this fact into account, it becomes preferable under certain conditions to perform the experiment at an angle, in spite of equation (6.1), to compensate for the premature energy losses. The performance is also affected by the quantum nature of radiation reaction. Due to the stochastic nature of photon emissions, it becomes possible for particles to for example reach the peak field without any premature loss of energy, in a process called staggering. Similarly, it is possible for particles to pass through the laser field without emitting at all, effectively quenching the photon emissions for sufficiently short pulses [142].

6.1 The dipole wave

While the typical setup has allowed us to reach high intensities, especially when employing adaptive optics in order to achieve tight focusing, it does not fully utilize the available laser power. For instance, consider having a laser pulse with a total energy $\mathcal{E}_1$, peak amplitude E_1 and peak intensity I_1, related to each other as $\mathcal{E}_1 \sim E_1^2 \sim I_1$, and split the laser pulse into N equal parts. Each subpulse will then carry an energy of $\mathcal{E}_N = \mathcal{E}_1/N$ and have a peak amplitude and intensity of $E_N = E_1/\sqrt{N}$ and $I_N = I_1/N$, respectively. The pulses can now be recombined and, through constructive interference, yield a peak amplitude of $NE_N = \sqrt{N}E_1$, corresponding to a peak intensity NI_1. Eventually, the achievable peak field saturates, as it becomes limited by diffraction. The optimal field configuration, resulting in the greatest field amplitude for any given laser power, has been proven to be that of

a dipole wave [143], provided that the field is monochromatic. The use of 4π-focusing or multiple colliding laser pulses for realizing this field using high-intensity lasers has been studied in several works [144], suggesting a belt-like configuration for focusing several pulses.

The dipole wave, essentially the field of a dipole antenna run in reverse, can be obtained analytically as an exact solution to Maxwell's equations (2.5). The solution permits two linearly independent modes, commonly referred to as the electric dipole (transverse magnetic) and magnetic dipole (transverse electric) depending on the field at the center of the structure. The field of a monochromatic electric dipole can be written as [144]

$$\mathbf{B}_e = \frac{3}{2} a_0 \sin(\omega t)(\hat{d} \times \hat{n}) \left[\frac{-kR\cos(kR) + \sin(kR)}{k^2 R^2} \right] \tag{6.2a}$$

$$\begin{aligned} \mathbf{E}_e = \frac{3}{2} a_0 \cos(\omega t) \Bigg\{ & \hat{d} \left[\frac{\left(k^2R^2 - 1\right)\sin(kR) + kR\cos(kR)}{k^3 R^3} \right] \\ & + \hat{n}(\hat{n} \cdot \hat{d}) \left[\frac{\left(3 - k^2R^2\right)\sin(kR) - 3kR\cos(kR)}{k^3 R^3} \right] \Bigg\}, \end{aligned} \tag{6.2b}$$

where the field is given in relativistic units, $\hat{n} = \mathbf{R}/R$ is the direction of observation and $\hat{d}$ is the (unit) dipole vector. The field is shown in Figure 6.1. The peak electric (magnetic) field is given by a_0 ($0.65a_0$) and the first azimuthal field maximum occurs at a distance of 0.33λ from the center. The peak amplitude can further be related to the total incident laser power, P, as $a_0 = \sqrt{16e^2P/3m^2c^5} \approx 780\sqrt{P\,[\mathrm{PW}]}$. The field of the magnetic dipole can similarly be obtained through the substitution $\mathbf{B}_m \leftarrow \mathbf{E}_e$, $\mathbf{E}_m \leftarrow -\mathbf{B}_e$.

Besides maximizing the peak field, the dipole wave is also spatially well localized, providing the benefit of allowing particles little opportunity to prematurely lose energy as it interacts with the tail. Looking more closely at the field geometry, it is obvious that it is not spherically symmetric. In fact, the incoming field creating this structure can in the far-field be written $I(\theta) \sim \sin^2\theta$, where θ is the angle to the dipole vector. This effectively leaves a hole along the dipole axis, allowing particles to effortlessly reach the central peak-field region. However, taking into account that the on-axis field is directed entirely along $\hat{d}$, an ultra-relativistic particle travelling along this axis will unfortunately only experience a negligible χ. Instead, for particles propagating in the $\hat{d}$-direction, χ is maximized at the first azimuthal peak.

To make use of the peak field, the particle momenta must lie in the normal plane of $\hat{d}$ as it passes through the center. While this may seem preferable to the previously discussed case, it must also be weighed against the adverse effects due to differing spatial distributions. Assuming a fixed particle momentum, the spatial distribution of χ falls off as ρ^{-1} for the case of in-plane motion, where ρ is the distance to the center. If the momentum is instead directed along $\hat{d}$, χ falls off more rapidly, as z^{-2}. In reality the

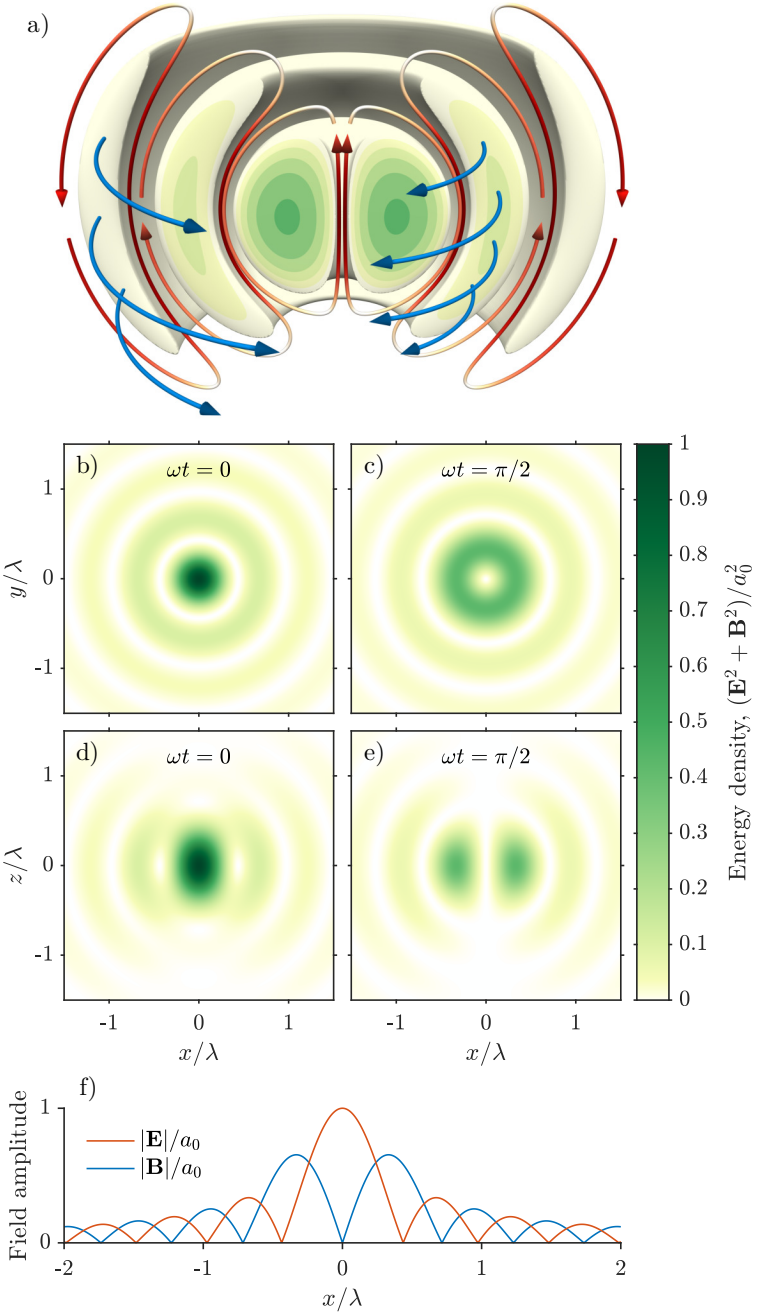

Figure 6.1: An electric dipole oriented with its symmetry axis in the z-direction ($\hat{d} = \hat{z}$), showing the electric field (red), magnetic field (blue) and energy density (green). The instantaneous energy density is shown in the xy-plane for $z = 0$ (b), (c) and in the xz-plane for $y = 0$ (d), (e) for two separate points in time. (f) The electric and magnetic field amplitudes are shown for a one dimensional cut along the x-axis, for $y = z = 0$.

actual distribution of χ experienced will depend on the past acceleration of the particle and its radiation losses, as well as the exact phase of the dipole wave.

6.2 The role of pair production

So far, we have discussed the intricacies of generating high-energy photons entirely based on what we know about the photon emission rates. However, as the nonlinear quantum parameter is increased, the effect of pair production also comes into play, with the pair production rate eventually becoming comparable to the photon emission rate. When this happens, the emitted high-energy photons decay into electron-positron pairs before having a chance to leave the strong-field region, hampering the yield of high-energy photons. To estimate when this effect becomes important it is instructive to talk about *radiation length* rather than actual emission rates. The radiation length is defined as the average distance (or time) between events, effectively constituting a mean free path. For an efficient generation of high-energy photons we therefore wish to minimize the radiation length l_{rad}, while equivalent the pair production scale length l_{pair} is kept large. The importance of these effects are then easily determined through comparison with the typical size of the field, l_{field}.

To estimate when this effect comes into play we note that the radiation length can be obtained in the limit of large χ from equation (5.21) as $l_{\text{rad}} \approx 15\lambda_{\text{C}}\gamma^{1/3}\left(a_0/a_{\text{S}}\right)^{-2/3}$. The pair production scale length can similarly be obtained from equation (5.26) as $l_{\text{pair}} \approx 3.8(\hbar\omega/\varepsilon_0)^{1/3} l_{\text{rad}}$. Assuming a photon energy within our high-energy definition, $\hbar\omega > \varepsilon_0/2$, the pair production scale length becomes $l_{\text{pair}} > 3l_{\text{rad}}$. In fact, this inequality holds for all values of χ and so producing large amounts of high-energy photons means minimizing $l_{\text{rad}}/l_{\text{field}}$ while keeping $l_{\text{rad}}/l_{\text{field}} = 3l_{\text{rad}}/l_{\text{field}}$ sufficiently large. The sweet-spot can therefore be expected to lie somewhere around $l_{\text{rad}}/l_{\text{field}} \sim 1$, with the position of the optima scaling as $a_0^2 \sim \gamma$, further assuming that $\chi \approx \gamma a_0/a_{\text{S}}$ (and similarly for χ_γ). In the limit of small χ the radiation length l_{rad} becomes independent of γ, while the pair production scale length has an exponential dependence on $(\chi_\gamma)^{-1}$. Neglecting logarithmic factors the position of the optima is therefore expected to scale as $a_0 \sim \gamma^{-1}$, implying a constant χ_γ. The intersection of the obtained scaling laws can naturally be expected to occur around $\chi \sim 1$. The high-χ scaling of l_{rad} thus suggests that the middle-ground can be found in the vicinity of $\varepsilon_0 \approx 14\,\text{GeV}$ ($\gamma \sim 28000$) for fields of optical size, $l_{\text{field}} = 1\,\mu\text{m}$. This point should also be where the optima of the photon generation efficiency is at the smallest possible a_0.

A more complete understanding of the balance between the two processes can be obtained by studying the exact scaling laws, presented in Figure 6.2

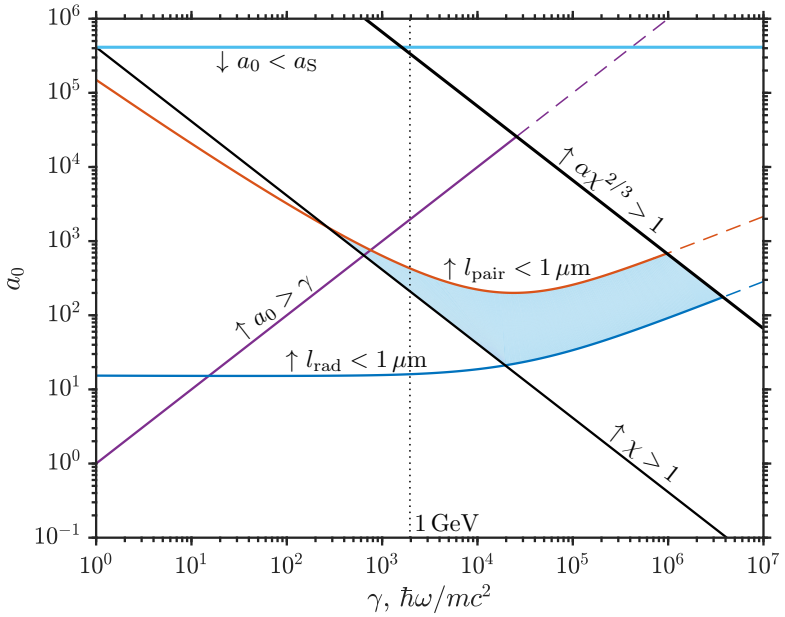

Figure 6.2: Lines of constant scale length (1 µm) for nonlinear Compton scattering (blue) and multi-photon Breit-Wheeler pair production (red), as functions of γ (or $\hbar\omega/mc^2$ in the case of l_{pair}) and a_0. Also shown is the Schwinger limit (cyan), $a_0 = \gamma$ (purple) and two values of constant χ (black). The thicker black line ($\alpha\chi^{2/3} = 1$) indicates a limit where QED is expected to become non-perturbative, and our current framework breaks down. Arrows indicate the side on which the displayed inequalities hold. The marked region indicates where high-energy photon production can be expected to be optimal.

as functions of γ and a_0, and where we have assumed that the typical size of the field is on the order of 1 µm. From our earlier discussions, we know that the optimal range for photon production occur for small l_{rad}, but large l_{pair}. For the produced photons to be of high energy, according to our earlier definition, also means restricting ourselves to large χ. The region of interest, resulting from these considerations, is marked in the figure. This region is also bounded at $\chi \sim 1600$, indicating a limit where strong-field QED is expected to become non-perturbative [145–149], preventing us from reaching any conclusions beyond this point.

6.2.1 The importance of the field shape

The arguments for why and how photon emission is influenced by the exact shape of the field distribution are equally valid in the case of pair production. For a given particle energy γ, this will affect both where the maximum occurs (at what a_0) as well as the high-energy photon production at the maximum. In this context, we use *production* in reference only to the photons able to

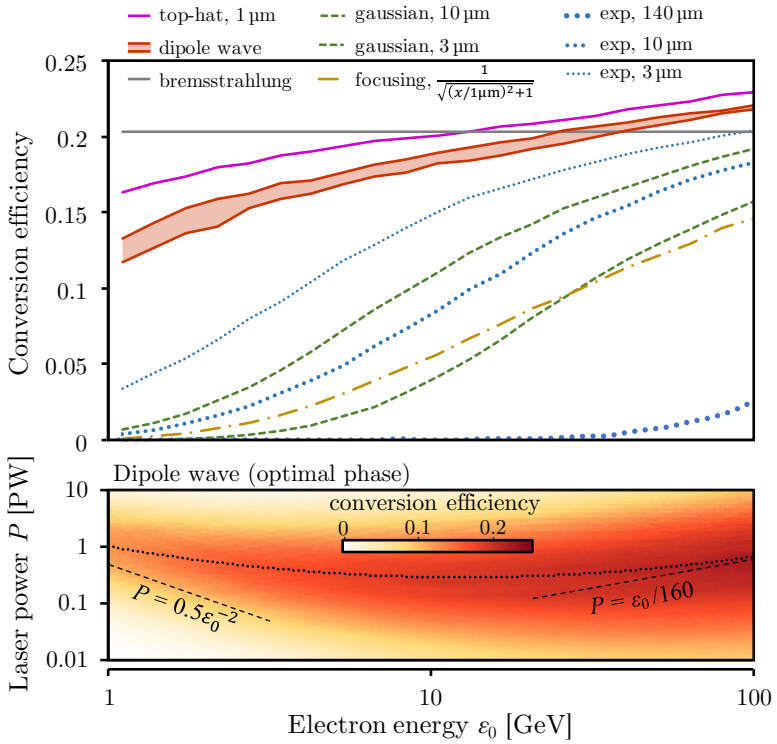

Figure 6.3: The computed conversion efficiency for optimal amplitude as a function of initial electron energy for various field shapes $S(x)$ and scale lengths. The electrons and all generated particles are assumed to be ultra-relativistic and experience fields given by $a_0/a_S = S(ct)$. The case of $S(x) \propto \exp(x/140\,\mu\text{m})$, for $x < 0$, corresponds to Ref. [150]. We also show the maximal conversion efficiency for bremsstrahlung, achieved at optimal thickness for arbitrary target material, see Ref. [151]. The result for the dipole wave is shown with bounds corresponding to different phases. The conversion efficiency for the optimal phase is shown on the lower panel as a function of laser power P and initial electron energy ε_0. The optimal laser power is shown for each initial electron energy (dotted) together with the analytical estimates (dashed).

escape the field without decaying into pairs. In order to investigate this effect, we performed a set of one-dimensional simulations in Paper C [136], wherein a beam of ultra-relativistic electrons are assumed to propagate rectilinearly through a given field. Any effect apart from photon emission and pair production are assumed to be negligible. The resulting *conversion efficiency*, the photon production normalized to the initial number of electrons, is shown in Figure 6.3.

In particular, the dipole wave is found to out-perform all other suggested field shapes and can be seen to surpass the optimal conversion efficiency expected from bremsstrahlung, given a sufficiently large electron beam energy. The only exception to this is the shape of a top-hat, which is unphysical

anyway. The conversion efficiency is further presented for the dipole wave as a function of the initial electron energy ($\varepsilon_0 \sim \gamma$) and the total laser power ($P \sim a_0^2$). The optimum can be seen to closely follow the estimated scaling laws, obtained earlier, and the lowest laser power needed to reach the turning point can be found around 10 GeV as predicted. Of particular significance is also the result that the optimal laser power can be as low as 0.4 PW, and is therefore within reach of current laser systems.

6.2.2 Pair production cascades

In situations where the pair production scale length is small compared to the typical size of the field, it becomes possible to trigger a pair cascade. These cascades can broadly be classified into two types, avalanches and showers [152], where the key difference between the two lies in their source of energy. In an avalanche, the energy fueling the cascade is primarily drawn from the laser field through continuous reacceleration of the particles, while a shower cascade primarily relies on the energy provided by the initial particles.

For a stationary target, or when the quiver energy obtained from the field is greater than a particle's initial energy (meaning $a_0 > \gamma$ initially), the typical particle energy will scale as $\gamma \sim a_0$. Again turning our attention to Figure 6.2, we see that the use of a stationary target for reaching large values of χ unavoidably means moving in the direction of strong pair production. This is reinforced by the fact that as the radiation reaction effects get stronger, the typical particle energy obtained in the field will be suppressed by radiation losses. As a result, the typical energy will not lie along the line of $\gamma = a_0$ for increasingly larger values of χ, but will bend upwards (where $\gamma < a_0$).

In relation to high-energy photon production, the prospect of triggering a self-sustained avalanche cascade using a dipole wave and a stationary target has recently been investigated, showing that photon energies up to a few GeV can be efficiently produced with this setup [153]. Beyond this point, however, and due to the suppression of the typical particle energy discussed earlier, the achievable photon energies scales only mildly with a_0. This motivates the use of an energetic electron beam for high-energy photon production beyond ~ 1 GeV, as originally suggested in Paper C [136].

In the dipole wave-electron beam setup studied in Papers C and D [136, 137] both cascade types can potentially be triggered, primarily depending on the field strength and the initial particle energy, requiring three-dimensional simulations to accurately capture the dynamics. As suggested by Figure 6.2, a shower cascade is obtained at sufficiently large field strengths. As some particles generated in this shower are produced with a low energy, the cascade also contain elements of the avalanche type. While the shower cascade must generally be avoided, if the goal is to produce an efficient high-energy photon source, the same is not necessarily true of the avalanche cascade,

as the accompanying reacceleration can instead provide a boost to the photon production. In Paper C [136], this boost was shown to occur despite the avalanche not being self-sustained. This was further studied in Paper D [137], looking primarily at the energy partitioning between the different particle species, and the results were used to highlight a number of regimes within reach of current and upcoming laser facilities.

Chapter 7

Particle-in-cell scheme

Since the equations describing the interaction of plasmas and electromagnetic fields are inherently complex and nonlinear the possibilities for studying these systems with analytical tools are very limited. For relativistic plasmas, such as those induced by ultra-intense laser fields, this possibility is reduced even further. This is especially true when considering problems of more dimensions than one, where geometrical considerations can be of great importance. The need for numerical tools for studying these systems should therefore be apparent.

The numerical solution of the Vlasov-Maxwell system of equations provides one of the most detailed description of a collisionless plasma. However, such a simulation would in the general case have to be solved in the fully six-dimensional phase space. Most codes of this type are as a result only employed for studying problems of greatly reduced dimensionality and are therefore restricted in scope. To improve the computational efficiency sophisticated numerical methods such as adaptive mesh refinement can be used, but the implementation of such techniques become increasingly complex for higher dimensions.

Alternatively, plasmas may be studied in the fluid description by solving the fluid equations. This is preferable to solving the kinetic equations when studying large systems as the fluid equations are only three-dimensional. However, the fluid description is a simplification of the kinetic description and can of course only be applied in regimes where its simplifying assumptions are valid. For example, because the dependence of the velocity distribution is lost in the fluid description it becomes inherently unsuitable for the study of systems with strong kinetic effects. This is often the case for plasmas interacting with ultra-intense laser fields.

Instead, the standard tool for large scale relativistic plasma simulations is the particle-in-cell (PIC) scheme [154]. It is a general approach to the numerical solution of partial differential equations such as the Vlasov-Maxwell equations and achieves a much more favourable scaling, than direct solu-

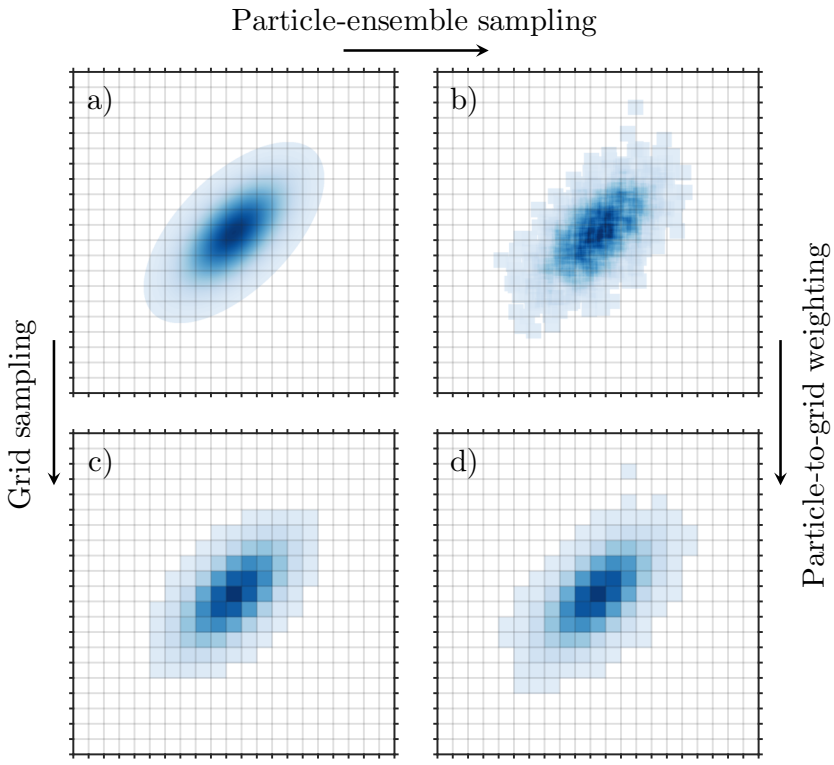

Figure 7.1: Illustration of the difference between directly solving the kinetic equations and the particle-in-cell method, for numerically evolving the distribution function $f_s(\mathbf{r}, \mathbf{v}, t)$. In the former case the distribution function (a) is discretized and its evolution is solved on a finite grid (b) while in the latter the distribution function is sampled using an ensemble of macro-particles (c) which will be evolved according to their equations of motion. The macro quantities of the ensemble are obtained on the grid by a weighting scheme (d), and can be used for the evolution of the fields.

tion of the kinetic equation, by effectively sampling the particle distribution functions. This is done by tracing an ensemble of macro-particles, representing the plasma, in continuous phase space and simultaneously calculating moments of the distribution function on a mesh, representing the simulated coordinate space. The system is advanced in time by self-consistently solving Maxwell's equations for the electromagnetic fields on the mesh as well as the equations of motion for the particles. The difference between directly solving the kinetic equations and the PIC scheme is illustrated in Figure 7.1.

7.1 Classical particle-in-cell scheme

At its core the classical PIC method [155] consists of advancing the fields on a computational mesh in the *field solver* and advancing the particles in phase space in the *particle pusher*. In the two intermediate stages the fields

are interpolated from the field mesh to the position of the particles and the currents produced by the particles are deposited on the mesh, respectively. The main blocks of the classical PIC method is diagrammatically shown in Figure 7.2. For each iteration, the position and velocity of each particle are used to compute the current density $\mathbf{J}(\mathbf{r})$ using a weighting scheme. This source term is then used in Maxwell's equations in order to advance the electric and magnetic fields $\mathbf{E}$ and $\mathbf{B}$. The charge density $\rho(\mathbf{r})$ can also be calculated, but Coulomb's law (eq. 2.5a) is typically only required as an initial condition. The field values are then interpolated to the position of each particle and the equations of motion are then solved in the particle pusher, where the position and velocity of each particle are updated.

There are several numerical methods which can be employed in the field solver such as FDTD, FEM, and spectral methods, with FDTD being the most commonly used. The mesh is allowed to be very complicated and the individual field components are not required to be co-located, as is the case for the FDTD method in which the mesh is that of a spatially staggered grid known as the *Yee grid* [156]. What is however universal for all of these methods is that the fields are calculated on a discrete mesh.

In the particle pusher the dynamics of the particles are computed according to the Lorentz force (2.6) and similarly to the field solver this can be done in several different ways. The *de facto* standard in plasma physics is the *Boris pusher* [157] in which the particle position and velocity is computed in a leapfrog-like manner and where the latter is most commonly updated in several steps. First, half of the electric impulse is added, then a rotation due to the magnetic field is performed before finally adding the remainder of the electric impulse.

As the physical systems can be very large in terms of the number of particles, with typical number densities of $10^{18}\,\mathrm{cm}^{-3}$ and above, it is often not feasible to simulate the system in its entirety. The workaround used in PIC schemes is to have every simulated particle represent a collection of real particles of the same type, called a *super-particle*. This is possible because a super-particle in a given field follows a path identical to that of its corresponding real particles, as their charge to mass ratios are the same. Furthermore, the super-particles are treated as being of finite size and are weighted to the mesh according to their shape, or *form factor*. These shapes can most easily be described by B-splines of varying degree, giving an increase in smoothness, but with a trade-off in computational speed. The most commonly used shapes are *nearest grid point* (NGP), *cloud-in-cell* (CIC) and *triangle shaped cloud* (TSC) corresponding to zeroth, first and second order interpolation, respectively. By employing the same weighting scheme for both the current deposition and field interpolation the PIC scheme can be made to conserve momentum. More advanced weighting schemes also exist in order to further guarantee for example charge conservation [158], but they are in general more computationally intensive.

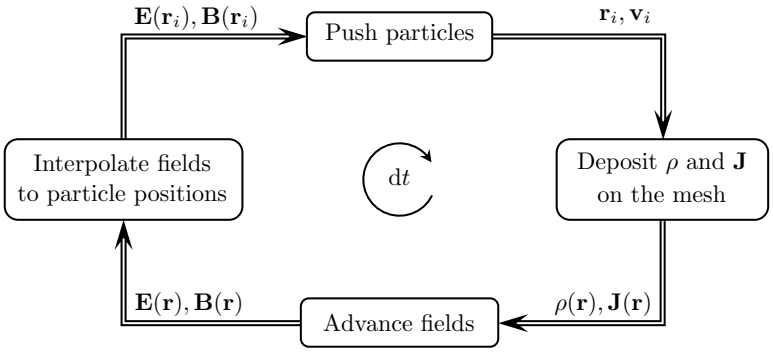

Figure 7.2: Diagrammatic representation of the classical PIC scheme. The vector $\mathbf{r}$ represents grid positions whereas the subscripted vectors, $\mathbf{r}_i$ and $\mathbf{v}_i$, represent positions and velocities of particles.

The PIC approach has proven to be an indispensable tool for advanced studies of plasma dynamics and has turned out to be applicable in a large number of regimes. As it is based on particle dynamics, it is straightforward to relate it to not only classical mechanics, but to quantum mechanical scattering processes as well. This allows the classical PIC scheme to be extended such that it can, to within certain limitations, account for particle collisions [159], ionization [160], radiation reaction [161, 162] and various quantum effects [163–167].

7.2 Extended particle-in-cell scheme (QED-PIC)

As mentioned the classical PIC scheme can easily be extended in order to include more physics, turning it into a highly versatile tool. Classical radiation reaction for example, covered briefly in Chapter 5, can easily be implemented by changing the particle pusher to one that accounts for the added terms of the LL equation (5.12). This changes the particle dynamics, which in turn affects both the collective motion of and radiation generated by the plasma.

If we are interested in also studying the emission of incoherent high-frequency radiation, such as synchrotron radiation, we will however have to make further extensions. The reason for this is that only the collective radiation, generated via the macroscopic current density, $\mathbf{J}$, is captured by the classical PIC scheme. Even if we theoretically could include the incoherent radiation on the grid, this would be very impractical given the large differences in scale between these types of radiation. The wavelength of the incoherent radiation emitted by ultra-relativistic particles can easily be on the order of 1 nm and below, and so to resolve such wavelengths on a computational mesh would for many simulations require a considerable increase in resolution. Fortunately, these wavelengths will also be much smaller than

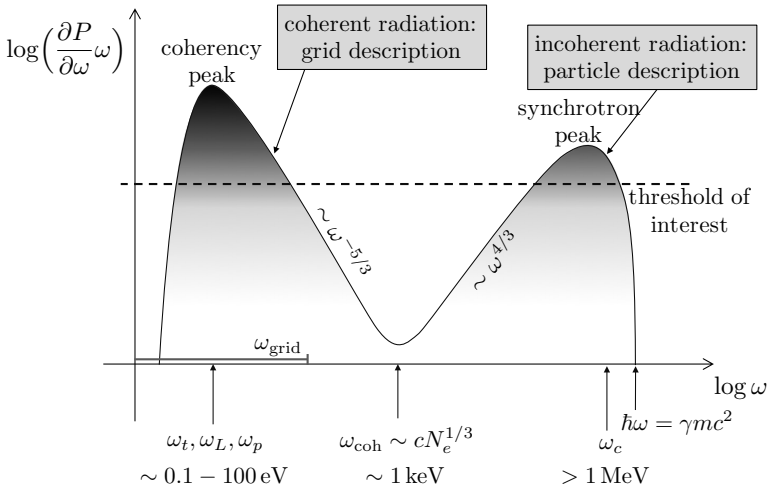

Figure 7.3: Illustration showing the separation of scale between coherent and incoherent (synchrotron) radiation. The figure has been adapted from Ref. [167].

all other relevant length scales, and the radiation can thus be well approximated as point-particles. This separation of scales between the coherent and incoherent radiation is illustrated in Figure 7.3. For most practical scenarios of interest we may therefore include the incoherent radiation as a separate particle species, photons, that propagate rectilinearly and at the speed of light.

As described in Chapter 5, the classical description of radiation reaction has several shortcomings. Most importantly, it is possible to reach the quantum regime $\chi \sim 1$ with state-of-the-art lasers, in which case the classical description will be naturally insufficient. Luckily, the PIC scheme is sufficiently versatile to admit more complicated descriptions. However, in order to include quantum radiation reaction we can no longer simply rely on an adapted particle pusher. Instead, we can make use of the rates for various QED processes and include these processes using a Monte Carlo-based approach. The resulting QED-PIC scheme, shown in Figure 7.4, is thus best described as semi-classical, where we assume that the motion of the (super) particles is described by the classical equations of motion between stochastic QED events. Most commonly, only two of the first order processes shown in Figure 5.3 are included, nonlinear Compton and multi-photon Breit-Wheeler. The reason for this is that the remaining two processes, photon absorption and pair annihilation, have comparatively small cross-sections as they require close collision between particles to occur [132, 133, 168]. Sometimes, the process of Schwinger pair production is also included, which is separate from Breit-Wheeler pair production in that the creation of a pair is entirely due to the background field.

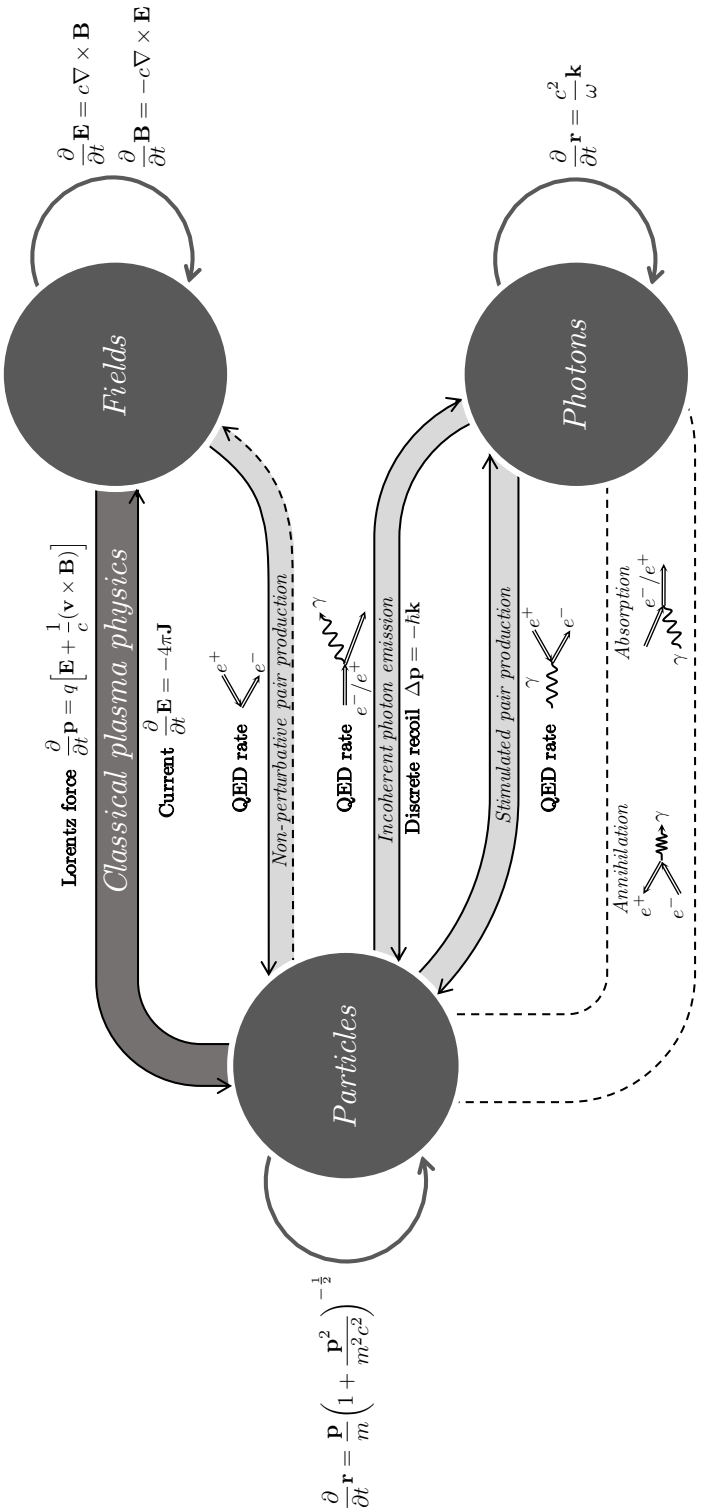

Figure 7.4: Diagrammatic representation of the QED-PIC scheme where the coherent radiation is represented by the *fields* and the incoherent radiation by *photons*. The figure has been adapted from Ref. [167].

There are several ways of implementing the QED event generator, but common for all of them is that they generate the events stochastically according to the number spectra of (5.18) and (5.25). In the case of photon emission, the recoil on the emitting particle is also included, thereby accounting for radiation reaction. The two most common ways of implementing it is to: *i*) randomly pick an energy and then use rejection sampling with the number spectrum to determine if the event should occur [164, 167]; or *ii*) randomly decide if an event should occur using the total probability of an event, and then determine the energy through inverse transform sampling [166, 169].

There are both advantages and disadvantages to each of the two approaches, with for example the latter requiring tabulation of the inverse cumulative distribution function, but common to both is that the probability of a QED event to occur within one time step should be less than unity. In fact, in order for the number of events over an extended duration of time to be accurate, the probability of a single event within one time step must be much smaller than unity. The reason for this is that we neglect the occurrence of multiple events within a single time step. Discounting any interference effects between events, the total number of events over a large number of time steps should therefore, on average, be underestimated. This discrepancy is minimized by making the events rare. Furthermore, a too high event probability could also lead to an apparent, yet unphysical, temporal correlation between such events.

This is typically only of an issue in regimes of very high χ and as the simplest way of ensuring a sufficient accuracy is to decrease the global time step, it can for the most part be ignored. At the same time this issue can not be fully overlooked, as decreasing the global time step can be highly inefficient. Ultimately, only particles experiencing a high χ are in need of the increased temporal resolution and only for a limited period of time, as the strong fields giving rise to the high χ are often well localized in both time and space. The general solution is therefore to implement what is called *subcycling*, for which the time step is reduced only for the particles in need of it, as determined by their instantaneous value of χ. This can be performed entirely in the particle pusher, without any changes to the remainder of the PIC loop, and is commonly done by splitting the time step into an integer number of substeps for the selected particles [167].

An improvement can be obtained by computing *when* the next emission will occur, instead of *if* it will occur within the current time step. This way a complete separation of time scales can be obtained between the QED-event generator and the classical PIC loop, allowing the global time step Δt to be set through consideration of only the usual PIC constraints due to the resolution of the plasma and stability of the field solver. An event generator that admits this separation is shown in Algorithm 1, in which the time until the next event $\Delta\tau$ is separately computed for each particle from the event

Algorithm 1: Time-separated event generator

$\chi \leftarrow \sqrt{|F_{\mu\nu}p^{\nu}|^2}/E_{\mathrm{S}}mc$
$\tau \leftarrow 0$
$\Delta\tau \leftarrow -\log(\mathrm{rand})t_{\mathrm{rad}}(\chi)$
while $\tau + \Delta\tau < \Delta t$ **do**
  $\tau \leftarrow \tau + \Delta\tau$
  Boris pusher($\Delta t' = \Delta\tau$)
  Trigger event
  $\chi \leftarrow \sqrt{|F_{\mu\nu}p^{\nu}|^2}/E_{\mathrm{S}}mc$
  $\Delta\tau \leftarrow -\log(\mathrm{rand})t_{\mathrm{rad}}(\chi)$
end while
Boris pusher($\Delta t' = \Delta t - \tau$)

probability rate $t_{\mathrm{rad}}(\chi) = N(\chi)^{-1}$, using the instantaneous χ of the particle. If the event time $\Delta\tau$ is small enough for the event to occur before the next global time step $\tau + \Delta\tau < \Delta$, where τ is the current subtime of the particle, the particle will first be pushed the corresponding amount of time and its subtime incremented, after which the event will be triggered. Subsequent events are computed identically, until the suggested subtime surpasses the global time step, at which point the event will be discarded and the particle pushed for the remainder of the subtime in order to synchronize with the global time step. At this point in time the particle has reached the time scale of the fields, which must therefore be advanced before any further events can be computed. Furthermore, this synchronization has no effects on the event probability other than that caused by the physical propagation of the fields, given that the events are uncorrelated.

The inclusion of these QED processes further leads to the possibility of launching particle cascades through a continuous production of high-energy photons and electron-positron pairs. This means that the number of simulated particles can grow exponentially within just a few time steps, quickly exhausting the computational resources. In order to overcome also this issue, several techniques have been developed for dynamically reducing the number of simulated particles while minimizing the noise introduced by the procedure. The two primary methods for accomplishing this are called particle merging [170–175] and and particle thinning [176, 177]. These have in common that the number of super-particles can be reduced by compensating with an increase in the particle factor of the remaining ensemble (super-particles are allowed to have different particle factors).

7.2.1 Assumptions, validity and omitted physics

As is always the case with numerical simulations, they rest on a set of assumptions that are important to be aware of in order to stay within its

range of applicability, or run the risk of reaching incorrect conclusions. The primary assumption of the semi-classical approach of QED-PIC is the validity of the locally constant crossed field approximation. More accurately the field must be slowly varying in time and space, compared to the formation length (the length over which the emission happens). In the high-intensity limit ($a_0 \gg 1$) the formation length is of the order $\lambda/a_0 \ll \lambda$ [168], where λ is the wavelength of the background laser field. In this regime the laser field varies on a scale much larger than the formation length, motivating the use of LCFA through which the rates of Section 5.3 can be obtained [132, 133].

To more accurately determine the range of validity of QED-PIC requires detailed benchmarks. However, in SFQED only the simplest diagrams have been calculated exactly, partly explaining why this numerical approach was conceived in the first place; to expand our knowledge of these processes in regimes of more than just a handful of particles. Herein lies the difficulty with benchmarking. Nevertheless, efforts have been and are being made towards benchmarking QED-PIC against some of the few exact results available [178, 179] and the current understanding is that the approximations are well motivated for most cases where $a_0 \gg 1$. For relatively moderate intensities ($a_0 \sim 1$) the LCFA rates mainly overestimate the number of low-frequency photons produced [180]. But as the contribution to e.g. radiation reaction from these photons is generally but a fraction of the effect, benchmarks indicate a reasonable agreement even at moderate a_0 [179]. It should also be pointed out that the overall effect of radiation reaction is typically small at moderate intensities, and so these errors will for the most part be negligible.

As mentioned earlier, many quantum effects and several QED processes are not accounted for in current QED-PIC codes. Some omissions are easier to motivate than others, such as photon absorption and pair annihilation mentioned earlier; their cross sections are simply too low in the typical regimes of interest to be of importance anyway. Higher-order processes such as trident, shown in Figure 5.3(f), could potentially be included. However, such higher order processes is partially already captured by the current implementation, through multi-step combinations of photon emission and pair production. Formally these scenarios are not identical. For example, the photon in the trident process is virtual, meaning that it does not need to conserve energy and momentum, and is never explicitly created. The probabilities for the single-step and combined two-step processes therefore do not exactly match. Furthermore, the probability of the trident process can not formally be separated into two independent channels corresponding to having a real or a virtual photon as intermediary. It is however possible to separate the amplitudes corresponding to the two "channels". For large values of χ the contribution of the one-step amplitude to the probability is suppressed, making it possible to approximately split the trident process under such circumstances [181, 182]. Further analytical work has also been

carried out for even higher-order processes [183], and may in the future lend itself to comparisons with QED-PIC simulations.

Avenues of improvement

In the QED-PIC scheme the super-particles propagate according to the classical equations of motion, in the same way as in standard PIC. While this obviously neglects the intricacies of quantum mechanics, it can be motivated by the fact that the centroid of a particle (Volkov) wave function closely follows the classical trajectory [184]. A more accurate description would however involve the evolution of the particle wave function, accounting for effects such as dispersion and interference. Because the typical time between particle-particle interactions is small and the density is small, these effects are assumed to be small. Of potentially greater importance is the role of particle spin. While effects of particle spin has not yet become a regular part of QED-PIC codes, its potential consequences has recently been studied [185–189]. It has for example been shown that significant spin-polarization can occur over femtosecond time scales and that spin-polarization can modify both the photon emission intensity and pair production rates by up to 30%.

In the typical approximation used in current codes photons are emitted parallel to the particle momentum. In reality, photons are emitted into a cone with finite opening angle, aligned with the particle momentum. Since this angle shrinks with particle energy, in the case of emissions from ultra-relativistic particles, finite beaming will only amount to a secondary effect. Nevertheless, its effects can be felt in for example the divergence of an electron beam after interacting with an intense laser pulse, and are of relevance to both current and upcoming experiments. In a recent study, this finite beaming was accounted for by utilizing the photon emission rates differential in both energy and scattering angle, demonstrating an improved agreement with QED predictions of nonlinear Compton scattering [190]. Implementing this into QED-PIC codes should be relatively straightforward, but will come with an added expense to the computational speed.

Bibliography

[1] T. H. Maiman, Nature **187**, 493 (1960).

[2] F. J. McClung and R. W. Hellwarth, J. Appl. Phys. **33**, 828 (1962).

[3] L. E. Hargrove, R. L. Fork, and M. A. Pollack, Appl. Phys. Lett. **5**, 4 (1964).

[4] D. Strickland and G. Mourou, Opt. Comm. **56**, 219 (1985).

[5] A. Piskarskas, A. Stabinis, and A. Yankauskas, Sov. Phys.-Usp. **29**, 869 (1986).

[6] P. Moulton, Opt. News **8**, 9 (1982).

[7] P. F. Moulton, J. Opt. Soc. Am. B **3**, 125 (1986).

[8] V. Yanovsky, V. Chvykov, G. Kalinchenko, P. Rousseau, T. Planchon, T. Matsuoka, A. Maksimchuk, J. Nees, G. Cheriaux, G. Mourou, and K. Krushelnick, Opt. Express **16**, 2109 (2008).

[9] M. D. Perry, D. Pennington, B. C. Stuart, G. Tietbohl, J. A. Britten, C. Brown, S. Herman, B. Golick, M. Kartz, J. Miller, H. T. Powell, M. Vergino, and V. Yanovsky, Opt. Lett. **24**, 160 (1999).

[10] C. Danson, D. Hillier, N. Hopps, and D. Neely, High Power Laser Sci. Eng. **3**, e3 (2015).

[11] Z. Gan, L. Yu, S. Li, C. Wang, X. Liang, Y. Liu, W. Li, Z. Guo, Z. Fan, X. Yuan, L. Xu, Z. Liu, Y. Xu, J. Lu, H. Lu, D. Yin, Y. Leng, R. Li, and Z. Xu, Opt. Express **25**, 5169 (2017).

[12] S. Gales, K. A. Tanaka, D. L. Balabanski, F. Negoita, D. Stutman, O. Tesileanu, C. A. Ur, D. Ursescu, I. Andrei, S. Ataman, M. O. Cernaianu, L. D'Alessi, I. Dancus, B. Diaconescu, N. Djourelov, D. Filipescu, P. Ghenuche, D. G. Ghita, C. Matei, K. Seto, M. Zeng, and N. V. Zamfir, Rep. Prog. Phys. **81**, 094301 (2018).

[13] ELI-Beamlines Website, www.eli-beams.eu (2019).

[14] B. Le Garrec, D. N. Papadopoulos, C. Le Blanc, J. P. Zou, G. Chériaux, P. Georges, F. Druon, L. Martin, L. Fréneaux, A. Beluze, N. Lebas, F. Mathieu, and P. Audebert, Proc. SPIE **10238** (2017).

[15] C. Hernandez-Gomez, S. P. Blake, O. Chekhlov, R. J. Clarke, A. M. Dunne, M. Galimberti, S. Hancock, R. Heathcote, P. Holligan, A. Lyachev, P. Matousek, I. O. Musgrave, D. Neely, P. A. Norreys, I. Ross, Y. Tang, T. B. Winstone, B. E. Wyborn, and J. Collier, J. Phys. Conf. Ser. **244**, 032006 (2010).

[16] W. Li, Z. Gan, L. Yu, C. Wang, Y. Liu, Z. Guo, L. Xu, M. Xu, Y. Hang, Y. Xu, J. Wang, P. Huang, H. Cao, B. Yao, X. Zhang, L. Chen, Y. Tang, S. Li, X. Liu, S. Li, M. He, D. Yin, X. Liang, Y. Leng, R. Li, and Z. Xu, Opt. Lett. **43**, 5681 (2018).

[17] XCELS Website, www.xcels.iapras.ru (2019).

[18] E. Cartlidge, Science **359**, 382 (2018).

[19] O. Coddington, J. L. Lean, P. Pilewskie, M. Snow, and D. Lindholm, Bull. Am. Meteorol. Soc. **97**, 1265 (2016).

[20] xkcd webcomic, xkcd.com.

[21] A. J. Gonsalves, K. Nakamura, J. Daniels, C. Benedetti, C. Pieronek, T. C. H. de Raadt, S. Steinke, J. H. Bin, S. S. Bulanov, J. van Tilborg, C. G. R. Geddes, C. B. Schroeder, C. Tóth, E. Esarey, K. Swanson, L. Fan-Chiang, G. Bagdasarov, N. Bobrova, V. Gasilov, G. Korn, P. Sasorov, and W. P. Leemans, Phys. Rev. Lett. **122**, 084801 (2019).

[22] A. Higginson, R. J. Gray, M. King, R. J. Dance, S. D. R. Williamson, N. M. H. Butler, R. Wilson, R. Capdessus, C. Armstrong, J. S. Green, S. J. Hawkes, P. Martin, W. Q. Wei, S. R. Mirfayzi, X. H. Yuan, S. Kar, M. Borghesi, R. J. Clarke, D. Neely, and P. McKenna, Nat. Commun. **9**, 724 (2018).

[23] U.S. Department of Energy roadmap, "Advanced accelerator development strategy report: DOE advanced accelerator concepts research roadmap workshop," (2016).

[24] V. S. Khoroshkov and E. I. Minakova, Eur. J. Phys. **19**, 523 (1998).

[25] E. Fourkal, B. Shahine, M. Ding, J. S. Li, T. Tajima, and C.-M. Ma, Med. Phys. **29**, 2788 (2002).

[26] S. Bulanov, T. Esirkepov, V. Khoroshkov, A. Kuznetsov, and F. Pegoraro, Phys. Lett. A **299**, 240 (2002).

[27] S. V. Bulanov and V. S. Khoroshkov, Plasma Phys. Rep. **28**, 453 (2002).

[28] V. Malka, S. Fritzler, E. Lefebvre, E. d'Humières, R. Ferrand, G. Grillon, C. Albaret, S. Meyroneinc, J.-P. Chambaret, A. Antonetti, and D. Hulin, Med. Phys. **31**, 1587 (2004).

[29] S. S. Bulanov, A. Brantov, V. Y. Bychenkov, V. Chvykov, G. Kalinchenko, T. Matsuoka, P. Rousseau, S. Reed, V. Yanovsky, K. Krushelnick, D. W. Litzenberg, and A. Maksimchuk, Med. Phys. **35**, 1770 (2008).

[30] H. Daido, M. Nishiuchi, and A. S. Pirozhkov, Rep. Prog. Phys. **75**, 056401 (2012).

[31] A. Macchi, M. Borghesi, and M. Passoni, Rev. Mod. Phys. **85**, 751 (2013).

[32] M. Borghesi, D. H. Campbell, A. Schiavi, M. G. Haines, O. Willi, A. J. MacKinnon, P. Patel, L. A. Gizzi, M. Galimberti, R. J. Clarke, F. Pegoraro, H. Ruhl, and S. Bulanov, Phys. Plasmas **9**, 2214 (2002).

[33] A. J. Mackinnon, P. K. Patel, M. Borghesi, R. C. Clarke, R. R. Freeman, H. Habara, S. P. Hatchett, D. Hey, D. G. Hicks, S. Kar, M. H. Key, J. A. King, K. Lancaster, D. Neely, A. Nikkro, P. A. Norreys, M. M. Notley, T. W. Phillips, L. Romagnani, R. A. Snavely, R. B. Stephens, and R. P. J. Town, Phys. Rev. Lett. **97**, 045001 (2006).

[34] B. Dromey, M. Coughlan, L. Senje, M. Taylor, S. Kuschel, B. Villagomez-Bernabe, R. Stefanuik, G. Nersisyan, L. Stella, J. Kohanoff, *et al.*, Nat. Commun. **7**, 10642 (2016).

[35] P. K. Patel, A. J. Mackinnon, M. H. Key, T. E. Cowan, M. E. Foord, M. Allen, D. F. Price, H. Ruhl, P. T. Springer, and R. Stephens, Phys. Rev. Lett. **91**, 125004 (2003).

[36] P. Debye and E. Hyckel, Phys. Zeitz. **24**, 185 (1923).

[37] J. D. Jackson, *Classical electrodynamics*, 3rd ed. (Wiley, 1998).

[38] J. H. Poynting, Philos. T. R. Soc. Lond. **175**, 343 (1884).

[39] A. A. Vlasov, J. Exp. Theor. Phys. **8**, 291 (1938).

[40] A. A. Vlasov, J. Phys. (USSR) **9**, 25 (1945).

[41] H. Alfvén, Nature **150**, 405 (1942).

[42] L. Landau, J. Phys. (USSR) **10** (1946).

[43] J. Magnusson, A. Gonoskov, and M. Marklund, Eur. Phys. J. D **71**, 231 (2017).

[44] P. Mulser and D. Bauer, *High Power Laser-Matter Interaction*, 1st ed., Springer Tracts in Modern Physics 238 (Springer-Verlag Berlin Heidelberg, 2010).

[45] A. Macchi, *A Superintense Laser-Plasma Interaction Theory Primer*, SpringerBriefs in Physics (Springer, 2013).

[46] L. Landau and E. Lifshitz, *The Classical Theory of Fields*, 4th ed. (1975).

[47] A. Fetter and J. Walecka, *Theoretical Mechanics of Particles and Continua*, Dover Books on Physics (Dover Publications, 2003).

[48] H. Goldstein, C. Poole, and J. Safko, *Classical Mechanics*, 3rd ed. (Addison Wesley, 2002).

[49] P. M. Woodward, J. IEE **93**, Part IIIA, 1554 (1947).

[50] J. D. Lawson, *Laser Accelerators?*, Rutherford Laboratory report RL-75-043 (1975).

[51] J. D. Lawson, IEEE Trans. Nucl. Sci. **NS-26**, 4217 (1979).

[52] R. B. Palmer, Part. Accel. **11**, 81 (1980).

[53] D. Bauer, P. Mulser, and W. H. Steeb, Phys. Rev. Lett. **75**, 4622 (1995).

[54] V. I. Veksler, Sov. J. At. Energy **2**, 525 (1957).

[55] T. Tajima and J. M. Dawson, Phys. Rev. Lett. **43**, 267 (1979).

[56] C. Joshi, W. B. Mori, T. Katsouleas, J. M. Dawson, J. M. Kindel, and D. W. Forslund, Nature **311**, 525 (1984).

[57] E. Esarey, C. B. Schroeder, and W. P. Leemans, Rev. Mod. Phys. **81**, 1229 (2009).

[58] P. Mora and T. M. Antonsen, Phys. Rev. E **53**, R2068 (1996).

[59] A. Pukhov and J. M. ter Vehn, Appl. Phys. B **74**, 355 (2002).

[60] S. P. Mangles, C. Murphy, Z. Najmudin, A. G. R. Thomas, J. Collier, A. E. Dangor, E. Divall, P. Foster, J. Gallacher, C. Hooker, D. A. Jaroszynski, A. J. Langley, W. B. Mori, P. A. Norreys, F. S. Tsung, R. Viskup, B. R. Walton, and K. Krushelnick, Nature **431**, 535 (2004).

[61] J. Faure, Y. Glinec, A. Pukhov, S. Kiselev, S. Gordienko, E. Lefebvre, J.-P. Rousseau, F. Burgy, and V. Malka, Nature **431**, 541 (2004).

[62] W. P. Leemans, B. Nagler, A. J. Gonsalves, C. Tóth, K. Nakamura, C. G. Geddes, E. Esarey, C. Schroeder, and S. Hooker, Nat. Phys. **2**, 696 (2006).

[63] S. P. Hatchett, C. G. Brown, T. E. Cowan, E. A. Henry, J. S. Johnson, M. H. Key, J. A. Koch, A. B. Langdon, B. F. Lasinski, R. W. Lee, A. J. Mackinnon, D. M. Pennington, M. D. Perry, T. W. Phillips, M. Roth, T. C. Sangster, M. S. Singh, R. A. Snavely, M. A. Stoyer, S. C. Wilks, and K. Yasuike, Phys. Plasmas **7**, 2076 (2000).

[64] S. C. Wilks, A. B. Langdon, T. E. Cowan, M. Roth, M. Singh, S. Hatchett, M. H. Key, D. Pennington, A. MacKinnon, and R. A. Snavely, Phys. Plasmas **8**, 542 (2001).

[65] A. J. Mackinnon, Y. Sentoku, P. K. Patel, D. W. Price, S. Hatchett, M. H. Key, C. Andersen, R. Snavely, and R. R. Freeman, Phys. Rev. Lett. **88**, 215006 (2002).

[66] M. Roth, A. Blazevic, M. Geissel, T. Schlegel, T. E. Cowan, M. Allen, J.-C. Gauthier, P. Audebert, J. Fuchs, J. Meyer-ter Vehn, M. Hegelich, S. Karsch, and A. Pukhov, Phys. Rev. ST Accel. Beams **5**, 061301 (2002).

[67] P. Mora, Phys. Rev. Lett. **90**, 185002 (2003).

[68] T. E. Cowan, J. Fuchs, H. Ruhl, A. Kemp, P. Audebert, M. Roth, R. Stephens, I. Barton, A. Blazevic, E. Brambrink, J. Cobble, J. Fernández, J.-C. Gauthier, M. Geissel, M. Hegelich, J. Kaae, S. Karsch, G. P. Le Sage, S. Letzring, M. Manclossi, S. Meyroneinc, A. Newkirk, H. Pépin, and N. Renard-LeGalloudec, Phys. Rev. Lett. **92**, 204801 (2004).

[69] M. Passoni, L. Bertagna, and A. Zani, New J. Phys. **12**, 045012 (2010).

[70] T. Ditmire, J. Tisch, E. Springate, M. Mason, N. Hay, R. Smith, J. Marangos, and M. Hutchinson, Nature **386**, 54 (1997).

[71] V. F. Kovalev, V. Y. Bychenkov, and K. Mima, Phys. Plasmas **14**, 103110 (2007).

[72] V. F. Kovalev, K. I. Popov, V. Y. Bychenkov, and W. Rozmus, Phys. Plasmas **14**, 053103 (2007).

[73] T. Esirkepov, S. Bulanov, K. Nishihara, T. Tajima, F. Pegoraro, V. Khoroshkov, K. Mima, H. Daido, Y. Kato, Y. Kitagawa, K. Nagai, and S. Sakabe, Phys. Rev. Lett. **89**, 175003 (2002).

[74] T. Esirkepov, M. Yamagiwa, and T. Tajima, Phys. Rev. Lett. **96**, 105001 (2006).

[75] S. S. Bulanov, A. Brantov, V. Y. Bychenkov, V. Chvykov, G. Kalinchenko, T. Matsuoka, P. Rousseau, S. Reed, V. Yanovsky, D. W. Litzenberg, K. Krushelnick, and A. Maksimchuk, Phys. Rev. E **78**, 026412 (2008).

[76] L. Yin, B. J. Albright, B. M. Hegelich, and J. C. Fernández, Laser Part. Beams **24**, 291 (2006).

[77] L. Yin, B. J. Albright, B. M. Hegelich, K. J. Bowers, K. A. Flippo, T. J. T. Kwan, and J. C. Fernández, Phys. Plasmas **14**, 056706 (2007).

[78] B. J. Albright, L. Yin, K. J. Bowers, B. M. Hegelich, K. A. Flippo, T. J. T. Kwan, and J. C. Fernández, Phys. Plasmas **14**, 094502 (2007).

[79] T. Schlegel, N. Naumova, V. T. Tikhonchuk, C. Labaune, I. V. Sokolov, and G. Mourou, Phys. Plasmas **16**, 083103 (2009).

[80] L. O. Silva, M. Marti, J. R. Davies, R. A. Fonseca, C. Ren, F. S. Tsung, and W. B. Mori, Phys. Rev. Lett. **92**, 015002 (2004).

[81] D. Haberberger, S. Tochitsky, F. Fiuza, C. Gong, R. A. Fonseca, L. O. Silva, W. B. Mori, and C. Joshi, Nat. Phys. **8**, 95 (2012).

[82] S. V. Bulanov, D. V. Dylov, T. Z. Esirkepov, F. F. Kamenets, and D. V. Sokolov, Plasma Phys. Rep. **31**, 369 (2005).

[83] T. Nakamura, S. V. Bulanov, T. Z. Esirkepov, and M. Kando, Phys. Rev. Lett. **105**, 135002 (2010).

[84] T. Esirkepov, M. Borghesi, S. Bulanov, G. Mourou, and T. Tajima, Phys. Rev. Lett. **92**, 175003 (2004).

[85] A. Henig, S. Steinke, M. Schnürer, T. Sokollik, R. Hörlein, D. Kiefer, D. Jung, J. Schreiber, B. M. Hegelich, X. Q. Yan, J. Meyer-ter Vehn, T. Tajima, P. V. Nickles, W. Sandner, and D. Habs, Phys. Rev. Lett. **103**, 245003 (2009).

[86] S. V. Bulanov, E. Y. Echkina, T. Z. Esirkepov, I. N. Inovenkov, M. Kando, F. Pegoraro, and G. Korn, Phys. Rev. Lett. **104**, 135003 (2010).

[87] S. Kar, K. F. Kakolee, B. Qiao, A. Macchi, M. Cerchez, D. Doria, M. Geissler, P. McKenna, D. Neely, J. Osterholz, R. Prasad, K. Quinn, B. Ramakrishna, G. Sarri, O. Willi, X. Y. Yuan, M. Zepf, and M. Borghesi, Phys. Rev. Lett. **109**, 185006 (2012).

[88] F. Brunel, Phys. Rev. Lett. **59**, 52 (1987).

[89] W. L. Kruer and K. Estabrook, Phys. Fluids **28**, 430 (1985).

[90] Y. Nodera, S. Kawata, N. Onuma, J. Limpouch, O. Klimo, and T. Kikuchi, Phys. Rev. E **78**, 046401 (2008).

[91] L. Cao, Y. Gu, Z. Zhao, L. Cao, W. Huang, W. Zhou, X. T. He, W. Yu, and M. Y. Yu, Phys. Plasmas **17**, 043103 (2010).

[92] Z. Zhao, L. Cao, L. Cao, J. Wang, W. Huang, W. Jiang, Y. He, Y. Wu, B. Zhu, K. Dong, Y. Ding, B. Zhang, Y. Gu, M. Y. Yu, and X. T. He, Phys. Plasmas **17**, 123108 (2010).

[93] A. Andreev, N. Kumar, K. Platonov, and A. Pukhov, Phys. Plasmas **18**, 103103 (2011).

[94] O. Klimo, J. Psikal, J. Limpouch, J. Proska, F. Novotny, T. Ceccotti, V. Floquet, and S. Kawata, New J. Phys. **13**, 053028 (2011).

[95] D. Margarone, O. Klimo, I. J. Kim, J. Prokůpek, J. Limpouch, T. M. Jeong, T. Mocek, J. Pšikal, H. T. Kim, J. Proška, K. H. Nam, L. Štolcová, I. W. Choi, S. K. Lee, J. H. Sung, T. J. Yu, and G. Korn, Phys. Rev. Lett. **109**, 234801 (2012).

[96] A. Andreev, K. Platonov, J. Braenzel, A. Lübcke, S. Das, H. Messaoudi, R. Grunwald, C. Gray, E. McGlynn, and M. Schnürer, Plasma Phys. Control. Fusion **58**, 014038 (2016).

[97] A. Lübcke, A. A. Andreev, S. Höhm, R. Grunwald, L. Ehrentraut, and M. Schnürer, Sci. Rep. **7**, 44030 (2017).

[98] M. Blanco, M. T. Flores-Arias, C. Ruiz, and M. Vranic, New J. Phys. **19**, 033004 (2017).

[99] L. Giuffrida, K. Svensson, J. Psikal, D. Margarone, P. Lutoslawski, V. Scuderi, G. Milluzzo, J. Kaufman, T. Wiste, M. Dalui, H. Ekerfelt, I. G. Gonzalez, O. Lundh, A. Persson, A. Picciotto, M. Crivellari, A. Bagolini, P. Bellutti, J. Magnusson, A. Gonoskov, L. Klimsa, J. Kopecek, T. Lastovicka, G. A. P. Cirrone, C.-G. Wahlström, and G. Korn, J. Instrum. **12**, C03040 (2017).

[100] L. Giuffrida, K. Svensson, J. Psikal, M. Dalui, H. Ekerfelt, I. Gallardo Gonzalez, O. Lundh, A. Persson, P. Lutoslawski, V. Scuderi, J. Kaufman, T. Wiste, T. Lastovicka, A. Picciotto, A. Bagolini, M. Crivellari, P. Bellutti, G. Milluzzo, G. A. P. Cirrone, J. Magnusson, A. Gonoskov, G. Korn, C.-G. Wahlström, and D. Margarone, Phys. Rev. Accel. Beams **20**, 081301 (2017).

[101] F. Mackenroth, A. Gonoskov, and M. Marklund, Phys. Rev. Lett. **117**, 104801 (2016).

[102] J. Magnusson, F. Mackenroth, M. Marklund, and A. Gonoskov, Phys. Plasmas **25**, 053109 (2018).

[103] P. Kaw and J. Dawson, Phys. Fluids **13**, 472 (1970).

[104] C. Max and F. Perkins, Phys. Rev. Lett. **27**, 1342 (1971).

[105] J. H. Marburger and R. F. Tooper, Phys. Rev. Lett. **35**, 1001 (1975).

[106] C. S. Lai, Phys. Rev. Lett. **36**, 966 (1976).

[107] F. S. Felber and J. H. Marburger, Phys. Rev. Lett. **36**, 1176 (1976).

[108] E. Lefebvre and G. Bonnaud, Phys. Rev. Lett. **74**, 2002 (1995).

[109] S. Guérin, P. Mora, J. C. Adam, A. Héron, and G. Laval, Phys. Plasmas **3**, 2693 (1996).

[110] H. Sakagami and K. Mima, Phys. Rev. E **54**, 1870 (1996).

[111] J. Fuchs, J. C. Adam, F. Amiranoff, S. D. Baton, P. Gallant, L. Gremillet, A. Héron, J. C. Kieffer, G. Laval, G. Malka, J. L. Miquel, P. Mora, H. Pépin, and C. Rousseaux, Phys. Rev. Lett. **80**, 2326 (1998).

[112] B. Shen and Z. Xu, Phys. Rev. E **64**, 056406 (2001).

[113] M. Tushentsov, A. Kim, F. Cattani, D. Anderson, and M. Lisak, Phys. Rev. Lett. **87**, 275002 (2001).

[114] L. Willingale, S. R. Nagel, A. G. R. Thomas, C. Bellei, R. J. Clarke, A. E. Dangor, R. Heathcote, M. C. Kaluza, C. Kamperidis, S. Kneip, K. Krushelnick, N. Lopes, S. P. D. Mangles, W. Nazarov, P. M. Nilson, and Z. Najmudin, Phys. Rev. Lett. **102**, 125002 (2009).

[115] J. Larmor, Philos. Mag. **44**, 503 (1897).

[116] A. Liénard, L'Éclairage Électrique **16**, 5, 53, 106 (1898).

[117] E. Wiechert, Ann. Phys. (Berl.) **309**, 667 (1901).

[118] W. Rindler, *Relativity*, 2nd ed. (Oxford University Press, 2006).

[119] F. R. Elder, A. M. Gurewitsch, R. V. Langmuir, and H. C. Pollock, Phys. Rev. **71**, 829 (1947).

[120] I. S. Gradshteyn, I. M. Ryzhik, Y. V. Geronimus, and M. Y. Tseytlin, *Table of Integrals, Series, and Products*, 4th corrected and enlarged ed. (Academic Press, 1980).

[121] M. Abraham, *Theorie der Elektrizität, Vol. II: Elektromagnetische Theorie der Strahlung* (Teubner, 1905).

[122] H. A. Lorentz, *The Theory of Electrons* (Teubner, 1909).

[123] P. A. M. Dirac, Proc. Royal Soc. A **167**, 148 (1938).

[124] D. A. Burton and A. Noble, Contemp. Phys. **55**, 110 (2014).

[125] D. M. Wolkow, Z. Phys. **94**, 250 (1935).

[126] F. Sauter, Z. Phys. **69**, 742 (1931).

[127] W. Heisenberg and H. Euler, Z. Phys. **98**, 714 (1936).

[128] J. Schwinger, Phys. Rev. **82**, 664 (1951).

[129] A. Nikishov, Nucl. Phys. B **21**, 346 (1970).

[130] T. D. Cohen and D. A. McGady, Phys. Rev. D **78**, 036008 (2008).

[131] S. S. Bulanov, T. Z. Esirkepov, A. G. R. Thomas, J. K. Koga, and S. V. Bulanov, Phys. Rev. Lett. **105**, 220407 (2010).

[132] A. Nikishov and V. Ritus, Sov. Phys.-JETP **19**, 529 (1964).

[133] A. Nikishov and V. Ritus, Sov. Phys.-JETP **19**, 1191 (1964).

[134] A. H. Sørensen, Nucl. Instrum. Methods Phys. Res. B **119**, 2 (1996).

[135] A. I. Nikishov and V. I. Ritus, Sov. Phys.-JETP **25**, 1135 (1967).

[136] J. Magnusson, A. Gonoskov, M. Marklund, T. Z. Esirkepov, J. K. Koga, K. Kondo, M. Kando, S. V. Bulanov, G. Korn, and S. S. Bulanov, Phys. Rev. Lett. **122**, 254801 (2019).

[137] J. Magnusson, A. Gonoskov, M. Marklund, T. Z. Esirkepov, J. K. Koga, K. Kondo, M. Kando, S. V. Bulanov, G. Korn, C. G. R. Geddes, C. B. Schroeder, E. Esarey, and S. S. Bulanov, arXiv:1906.05235 (2019).

[138] C. Bula, K. T. McDonald, E. J. Prebys, C. Bamber, S. Boege, T. Kotseroglou, A. C. Melissinos, D. D. Meyerhofer, W. Ragg, D. L. Burke, R. C. Field, G. Horton-Smith, A. C. Odian, J. E. Spencer, D. Walz, S. C. Berridge, W. M. Bugg, K. Shmakov, and A. W. Weidemann, Phys. Rev. Lett. **76**, 3116 (1996).

[139] D. L. Burke, R. C. Field, G. Horton-Smith, J. E. Spencer, D. Walz, S. C. Berridge, W. M. Bugg, K. Shmakov, A. W. Weidemann, C. Bula, K. T. McDonald, E. J. Prebys, C. Bamber, S. J. Boege, T. Koffas, T. Kotseroglou, A. C. Melissinos, D. D. Meyerhofer, D. A. Reis, and W. Ragg, Phys. Rev. Lett. **79**, 1626 (1997).

[140] J. M. Cole, K. T. Behm, E. Gerstmayr, T. G. Blackburn, J. C. Wood, C. D. Baird, M. J. Duff, C. Harvey, A. Ilderton, A. S. Joglekar, K. Krushelnick, S. Kuschel, M. Marklund, P. McKenna, C. D. Murphy, K. Poder, C. P. Ridgers, G. M. Samarin, G. Sarri, D. R. Symes, A. G. R. Thomas, J. Warwick, M. Zepf, Z. Najmudin, and S. P. D. Mangles, Phys. Rev. X **8**, 011020 (2018).

[141] K. Poder, M. Tamburini, G. Sarri, A. Di Piazza, S. Kuschel, C. D. Baird, K. Behm, S. Bohlen, J. M. Cole, D. J. Corvan, M. Duff, E. Gerstmayr, C. H. Keitel, K. Krushelnick, S. P. D. Mangles, P. McKenna, C. D. Murphy, Z. Najmudin, C. P. Ridgers, G. M. Samarin, D. R. Symes, A. G. R. Thomas, J. Warwick, and M. Zepf, Phys. Rev. X **8**, 031004 (2018).

[142] C. N. Harvey, A. Gonoskov, A. Ilderton, and M. Marklund, Phys. Rev. Lett. **118**, 105004 (2017).

[143] I. Bassett, Opt. Acta **33**, 279 (1986).

[144] I. Gonoskov, A. Aiello, S. Heugel, and G. Leuchs, Phys. Rev. A **86**, 053836 (2012).

[145] V. Ritus, Ann. Phys. **69**, 555 (1972).

[146] N. B. Narozhny, Phys. Rev. D **21**, 1176 (1980).

[147] A. Fedotov, J. Phys. Conf. Ser. **826**, 012027 (2017).

[148] T. Podszus and A. Di Piazza, Phys. Rev. D **99**, 076004 (2019).

[149] A. Ilderton, Phys. Rev. D **99**, 085002 (2019).

[150] A. Benedetti, M. Tamburini, and C. H. Keitel, Nat. Photonics **12**, 319 (2018).

[151] T. G. Blackburn and M. Marklund, Plasma Phys. Control. Fusion **60**, 054009 (2018).

[152] A. Mironov, N. Narozhny, and A. Fedotov, Phys. Lett. A **378**, 3254 (2014).

[153] A. Gonoskov, A. Bashinov, S. Bastrakov, E. Efimenko, A. Ilderton, A. Kim, M. Marklund, I. Meyerov, A. Muraviev, and A. Sergeev, Phys. Rev. X **7**, 041003 (2017).

[154] F. Harlow, Los Alamos Scientific Laboratory report LAMS-1956 (1955).

[155] J. M. Dawson, Rev. Mod. Phys. **55**, 403 (1983).

[156] K. Yee, IEEE Trans. Antennas Propag. **14**, 302 (1966).

[157] J. Boris, in *Proc. Fourth Conf. Num. Sim. Plasmas, Naval Res. Lab, Wash. DC* (1970) pp. 3–67.

[158] T. Z. Esirkepov, Comput. Phys. Commun. **135**, 144 (2001).

[159] F. Peano, M. Marti, L. O. Silva, and G. Coppa, Phys. Rev. E **79**, 025701 (2009).

[160] M. Chen, E. Cormier-Michel, C. Geddes, D. Bruhwiler, L. Yu, E. Esarey, C. Schroeder, and W. Leemans, J. Comput. Phys. **236**, 220 (2013).

[161] M. Tamburini, F. Pegoraro, A. D. Piazza, C. H. Keitel, and A. Macchi, New J. Phys. **12**, 123005 (2010).

[162] M. Chen, A. Pukhov, T.-P. Yu, and Z.-M. Sheng, Plasma Phys. Control. Fusion **53**, 014004 (2011).

[163] E. N. Nerush, I. Y. Kostyukov, A. M. Fedotov, N. B. Narozhny, N. V. Elkina, and H. Ruhl, Phys. Rev. Lett. **106**, 035001 (2011).

[164] N. V. Elkina, A. M. Fedotov, I. Y. Kostyukov, M. V. Legkov, N. B. Narozhny, E. N. Nerush, and H. Ruhl, Phys. Rev. ST Accel. Beams **14**, 054401 (2011).

[165] I. V. Sokolov, N. M. Naumova, and J. A. Nees, Phys. Plasmas **18**, 093109 (2011).

[166] C. Ridgers, J. Kirk, R. Duclous, T. Blackburn, C. Brady, K. Bennett, T. Arber, and A. Bell, J. Comput. Phys. **260**, 273 (2014).

[167] A. Gonoskov, S. Bastrakov, E. Efimenko, A. Ilderton, M. Marklund, I. Meyerov, A. Muraviev, A. Sergeev, I. Surmin, and E. Wallin, Phys. Rev. E **92**, 023305 (2015).

[168] V. I. Ritus, J. Sov. Laser Res. **6**, 497 (1985).

[169] J. G. Kirk, A. R. Bell, and I. Arka, Plasma Phys. Control. Fusion **51**, 085008 (2009).

[170] G. Lapenta, J. Comput. Phys. **181**, 317 (2002).

[171] F. Assous, T. P. Dulimbert, and J. Segré, J. Comput. Phys. **187**, 550 (2003).

[172] D. Welch, T. Genoni, R. Clark, and D. Rose, J. Comput. Phys. **227**, 143 (2007).

[173] J. Teunissen and U. Ebert, J. Comput. Phys. **259**, 318 (2014).

[174] M. Vranic, T. Grismayer, J. Martins, R. Fonseca, and L. Silva, Comput. Phys. Commun. **191**, 65 (2015).

[175] P. T. Luu, T. Tückmantel, and A. Pukhov, Comput. Phys. Commun. **202**, 165 (2016).

[176] G. Lapenta and J. U. Brackbill, J. Comput. Phys. **115**, 213 (1994).

[177] A. Gonoskov, arXiv:1607.03755 (2016).

[178] C. N. Harvey, A. Ilderton, and B. King, Phys. Rev. A **91**, 013822 (2015).

[179] T. G. Blackburn, D. Seipt, S. S. Bulanov, and M. Marklund, Phys. Plasmas **25**, 083108 (2018).

[180] A. Di Piazza, M. Tamburini, S. Meuren, and C. H. Keitel, Phys. Rev. A **98**, 012134 (2018).

[181] A. Ilderton, Phys. Rev. Lett. **106**, 020404 (2011).

[182] B. King and H. Ruhl, Phys. Rev. D **88**, 013005 (2013).

[183] V. Dinu and G. Torgrimsson, Phys. Rev. D **99**, 096018 (2019).

[184] D. Seipt, arXiv:1701.03692 (2017).

[185] B. King, N. Elkina, and H. Ruhl, Phys. Rev. A **87**, 042117 (2013).

[186] R. Ekman, F. A. Asenjo, and J. Zamanian, Phys. Rev. E **96**, 023207 (2017).

[187] D. Del Sorbo, D. Seipt, T. G. Blackburn, A. G. R. Thomas, C. D. Murphy, J. G. Kirk, and C. P. Ridgers, Phys. Rev. A **96**, 043407 (2017).

[188] D. D. Sorbo, D. Seipt, A. G. R. Thomas, and C. P. Ridgers, Plasma Phys. Control. Fusion **60**, 064003 (2018).

[189] D. Seipt, D. Del Sorbo, C. P. Ridgers, and A. G. R. Thomas, Phys. Rev. A **98**, 023417 (2018).

[190] T. G. Blackburn, D. Seipt, S. S. Bulanov, and M. Marklund, arXiv:1904.07745 (2019).

Summary of papers

Paper A

Energy partitioning and electron momentum distributions in intense laser-solid interactions
In this paper we demonstrate and assess the effect on the generated hot electrons of adding micro- and nanoscale structures to a plasma slab, irradiated by an intense laser field. We show that the addition of the structures not only increases the absorption of the laser radiation, but also drastically changes the angular distribution of the generated hot electrons. This change is quantified and its importance for ion acceleration is discussed.

Paper B

Prospects for laser-driven ion acceleration through controlled displacement of electrons by standing waves
In this paper we discuss and elaborate on how controllable laser-driven ion acceleration can be achieved by controlling the electron dynamics using standing waves. We further analyse the robustness of this approach against field structure imperfections, such as those caused by misalignment, elliptical polarization and limited contrast. This is done by focusing on a particular implementation of this approach, chirped-standing-wave acceleration, and also identify the prospects and limitations of this implementation.

Paper C

Laser-particle collider for multi-GeV photon production
In this paper we develop a concept for a laser-particle collider that would be capable of delivering dense beams of multi-GeV photons. We show that the efficiency of the photon generation is determined from the balance between photon generation and pair production and that the maximum efficiency is strongly influenced by the localization of the electromagnetic field. We demonstrate the existence of an optimal laser power and that the optimally focused field of a dipole wave, which can be realized using multiple colliding

laser pulses, provides a field structure that is favourable for the purpose of high-energy photon generation. Notably, the optimal laser power, in the case of a dipole field, is obtained to be as low as 0.4 PW.

Paper D

Multiple-colliding laser pulses as a basis for studying high-field high-energy physics

In this paper we further investigate the interaction of an energetic electron beam and multiple colliding laser pulses. We review the results of previous studies, analyse the expected radiation losses analytically and present new simulation results. In particular, the triggering and dynamics of pair production cascades in this setup are investigated. A number of regimes within reach of current and upcoming laser facilities are finally identified and summarized.